Electroweak Properties of Halo Nuclei in Effective Field Theory

Zur Erlangung des Grades eines Doktors der Naturwissenschaften (Dr. rer. nat.)
genehmigte Dissertation von Wael Elkamhawy aus Böblingen
Tag der Einreichung: 25. Januar 2021, Tag der Prüfung: 17. Februar 2021

1. Gutachten: Prof. Dr. Hans-Werner Hammer
2. Gutachten: Prof. Ph.D. Achim Schwenk
Darmstadt – D17

TECHNISCHE
UNIVERSITÄT
DARMSTADT

Fachbereich Physik
Institut für Kernphysik
AG Hammer

Electroweak Properties of Halo Nuclei in Effective Field Theory

Doctoral thesis by Wael Elkamhawy

1. Review: Prof. Dr. Hans-Werner Hammer
2. Review: Prof. Ph.D. Achim Schwenk

Date of submission: January 25, 2021
Date of thesis defense: February 17, 2021

Darmstadt – D17

Erklärungen laut Promotionsordnung

§8 Abs. 1 lit. c PromO

Ich versichere hiermit, dass die elektronische Version meiner Dissertation mit der schriftlichen Version übereinstimmt.

§8 Abs. 1 lit. d PromO

Ich versichere hiermit, dass zu einem vorherigen Zeitpunkt noch keine Promotion versucht wurde. In diesem Fall sind nähere Angaben über Zeitpunkt, Hochschule, Dissertationsthema und Ergebnis dieses Versuchs mitzuteilen.

§9 Abs. 1 PromO

Ich versichere hiermit, dass die vorliegende Dissertation selbstständig und nur unter Verwendung der angegebenen Quellen verfasst wurde.

§9 Abs. 2 PromO

Die Arbeit hat bisher noch nicht zu Prüfungszwecken gedient.

Darmstadt, 25. Januar 2021

Wael Elkamhawy

Abstract

The exploration of atomic nuclei across the nuclear landscape poses a great challenge in nuclear theory. In this thesis, we investigate nuclei on the nuclear chart for which the effective number of degrees of freedom is significantly smaller than the number of nucleons. This phenomenon is called clustering and becomes extreme for so-called halo nuclei. These exotic nuclei occur along the neutron and proton driplines far from the valley of stability. They exhibit a scale separation apparent through the small separation energy of the loosely bound valence nucleons in contrast to the high binding and excitation energies of the core. By exploiting this scale separation, we construct an effective field theory (EFT) called Halo EFT which allows to describe these systems in a controlled and systematically improvable manner.

In the first part, we investigate the one-neutron halo structures within ^{15}C. They appear in the ground $1/2^+$ and in the first excited $5/2^+$ state. The ground state is predominantly bound in an S-wave while the $5/2^+$ excited state is predominantly bound in a D-wave. Within Halo EFT, using standard Cartesian coordinates, we discuss static electromagnetic properties as well as electromagnetic transitions in halo nuclei and apply our results to ^{15}C. Since our results are universal, we are able to compare them to *ab initio* results. This possibility enables us to determine unknown low-energy constants, in turn increasing the predictive power of our Halo EFT.

The second system is the one-neutron halo nucleus ^{31}Ne which is bound in a P-wave. In this case, we construct a Halo EFT using a spherical basis, an approach ideally suited for the inclusion of halo states beyond the S-wave. Thereby, we investigate the electromagnetic E1 breakup reaction into the continuum consisting of the neutron and ^{30}Ne core. Additionally, we provide results for static properties and discuss the deformation of ^{31}Ne due to the non-vanishing quadrupole moment.

The third part is a pilot study of the weak decay of the valence neutron of the halo nucleus ^{11}Be into the continuum within Halo EFT. This process, denoted $^{11}\text{Be} \to {}^{10}\text{Be}+p+e^-+\bar{\nu}_e$, is called beta-delayed proton emission. The experimental determination of the branching

ratio for this decay remains an unsolved problem due to inconsistent measurements in different experiments. We calculate the rate of this rare decay with a robust uncertainty estimate. We also discuss the impact of a recently discovered resonance in ^{11}B on the branching ratio and compare it to different experimental results.

In the fourth and final part of this thesis, we investigate the universal behavior of weakly bound charged systems in three- and one-dimensional space. The focus lies on the study of one-proton halo nuclei bound in an S-wave. In particular, the impact of the repulsive long-ranged Coulomb force is analyzed. It introduces an additional length scale D (or momentum scale k_C). We classify universal regimes characterized by the different hierarchies of the Coulomb-modified scattering length a_C and D.

Zusammenfassung

Die Erforschung von Atomkernen über die gesamte Nuklidkarte hinweg stellt eine große Herausforderung in der theoretischen Kernphysik dar. In dieser Arbeit werden Kerne studiert, deren Anzahl effektiver Freiheitsgrade signifikant kleiner ist als die Anzahl der Nukleonen. Dieses Phänomen nennt sich „Clustering“ und ist für sogenannte Halokerne stark ausgeprägt. Diese exotischen Kerne finden sich entlang der Neutronen- und Protonendripline weit entfernt vom Tal der Stabilität. Des Weiteren weisen sie eine Skalenseparation auf, die durch die kleine Separationsenergie des schwach gebundenen Valenznukleons im Gegensatz zu den hohen Bindungs- und Anregungsenergien des verbleibenden Kerns gegeben ist. Durch Ausnutzen dieser Skalenseparation wird eine effektive Feldtheorie (EFT) namens Halo-EFT konstruiert. Damit wird eine Beschreibung dieser Systeme auf eine kontrollierte und systematisch verbesserbare Art und Weise ermöglicht.

Zunächst werden die Ein-Neutron-Halostrukturen im Kern ^{15}C untersucht. Diese kommen im $1/2^+$ Grundzustand sowie im ersten angeregten $5/2^+$ Zustand vor. Der Grundzustand ist überwiegend in einer S-Welle gebunden, während der $5/2^+$ angeregte Zustand überwiegend in einer D-Welle gebunden ist. Mittels Halo-EFT und den üblichen kartesischen Koordinaten werden statische elektromagnetische Eigenschaften sowie elektromagnetische Übergänge in Halokerne untersucht und die Ergebnisse auf den Kern ^{15}C angewandt. Da die Ergebnisse universell sind, können diese mit *ab initio* Resultaten verglichen werden. Dies ermöglicht die Bestimmung weiterer unbekannter Niederenergiekonstanten, wodurch die Vorhersagekraft der Halo-EFT steigt.

Das zweite System ist der Ein-Neutron-Halokern ^{31}Ne, welcher in einer P-Welle gebunden ist. In diesem Fall wird eine Halo-EFT mit sphärischen Koordinaten konstruiert. Es zeigt sich, dass diese ideal für die Einbeziehung von Halozuständen, die über die S-Welle hinausgehen, geeignet ist. Dabei wird die elektromagnetische E1-Aufbruchsreaktion ins Kontinuum bestehend aus Neutron und ^{30}Ne-Kern untersucht. Zusätzlich werden

die Ergebnisse für statische Eigenschaften von ^{31}Ne angegeben sowie die Deformation aufgrund des nicht-verschwindenden Quadrupolmoments diskutiert.

Der dritte Teil der Arbeit ist eine Pilotstudie des schwachen Zerfalls des Valenzneutrons des Halokerns ^{11}Be ins Kontinuum. Dieser Prozess, geschrieben als $^{11}\text{Be} \rightarrow {}^{10}\text{Be} + p + e^- + \bar{\nu}_e$, wird auch „beta-delayed proton emission“ genannt. Die experimentelle Bestimmung des Verzweigungsverhältnisses dieses Zerfalls von ^{11}Be bleibt aufgrund von inkonsistenten Messungen in verschiedenen Experimenten ein ungelöstes Problem. In dieser Arbeit wird die Rate des seltenen Zerfalls inklusive einer zuverlässigen Unsicherheitsabschätzung berechnet. Außerdem wird der Einfluss einer neu gefundenen Resonanz in ^{11}B auf das Verzweigungsverhältnis diskutiert und schließlich mit experimentellen Ergebnissen verglichen.

Im letzten Teil wird das universelle Verhalten von schwach gebundenen, geladenen Systemen in drei sowie einer Raumdimension studiert. Der Fokus liegt auf die Untersuchung von Ein-Proton-Halokernen, welche in einer S-Welle gebunden sind. Dabei wird der Einfluss der abstoßenden langreichweitigen Coulombkraft analysiert. Diese führt eine zusätzliche Längenskala D (beziehungsweise eine Impulsskala k_C) ein. Es werden verschiedene universelle Bereiche aufgrund der unterschiedlichen Hierarchien der Coulomb-modifizierten Streulänge a_C und D klassifiziert.

Contents

1. Introduction

In nuclear theory, the description of the nuclear chart in terms of the fundamental strong interaction described by quantum chromodynamics (QCD) constitutes a major challenge. The reason for this is the large value of the QCD coupling constant at low energies rendering perturbative approaches impossible. QCD is the relevant interaction for the adequate description of the substructure of a single nucleon consisting of quarks and gluons. Within this fundamental picture, the nucleons are bound states of three constituent quarks interacting through the mediation of gluons, the gauge bosons of the strong force.

Over the last years, a nonperturbative approach called lattice QCD [1], [2] has been very successful in calculating the light hadronic spectrum such as the nucleon "from first principles". Unfortunately, due to computational limitations, the precise description of light nuclei remains challenging.

However, the fact that low-energy phenomena in nuclear physics do not probe physics at short distances allows to use effective degrees of freedom that are relevant at larger length or smaller energy scales. In fact, strongly interacting matter undergoes a phase transition that leads to the confinement of quarks into composite particles. Such composites can be used as degrees of freedom for a hierarchy of effective field theories (EFTs) that describe the strong interaction at different resolution scales as depicted in Fig. 1.1. Chiral effective field theory (χEFT), for example, establishes a direct connection to QCD. It uses pions and nucleons as effective degrees of freedom instead of quarks and gluons. It allows for a systematic description of the nuclear force in chiral perturbation theory (ChPT) [4], [5]. These derived interactions based on QCD can then be used in *ab initio* methods, e.g., the no-core shell model [6], in coupled cluster theory [7] or by the in-medium similarity renormalization group [8], to solve the many-body problem using controlled and improvable truncations with quantified theoretical uncertainties. Fig. 1.2 shows the progress made in *ab initio* nuclear structure calculations over the past decade.

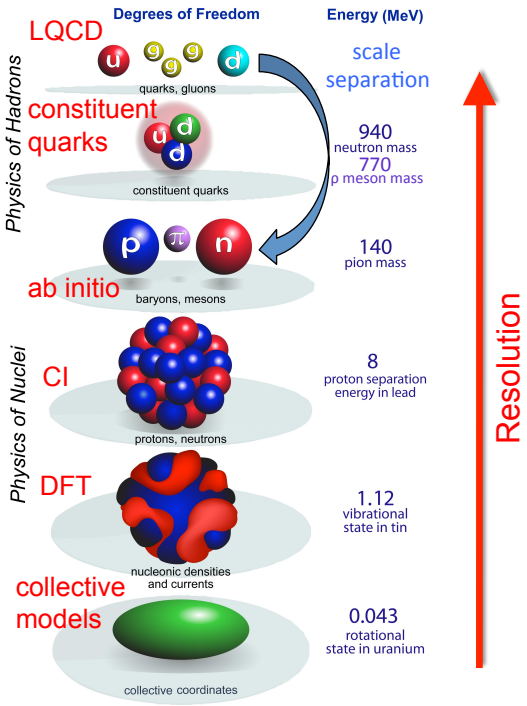

Figure 1.1.: Relevant degrees of freedom depending on the resolution scale. Figure taken from Ref. [3]

It is important to note that there are various systems in the nuclear chart for which the effective number of degrees of freedom is significantly smaller than the number of nucleons. This phenomenon is called clustering and a very prominent example is alpha clustering, e.g., in the Hoyle state of ^{12}C [10] and other light nuclei. It becomes more extreme for so-called halo nuclei. These exotic nuclei lie along the neutron and proton driplines far from stability [11], [12]. For such systems, the number of degrees of freedom is strongly reduced to a tightly bound core and a few loosely bound valence nucleons. This reduction is a consequence of a separation of scales in the system. This separation ensures that the EFT technique is a reliable method allowing a systematic and precise description of such physical systems. In case of a one-nucleon halo nucleus, the separation of scales is apparent through the small separation energy of the loosely bound valence nucleon in contrast to the comparatively high binding and excitation energies of the core. It allows for a systematic low-energy expansion in the ratio of these two scales. The expansion allows for calculations of nuclear observables in a

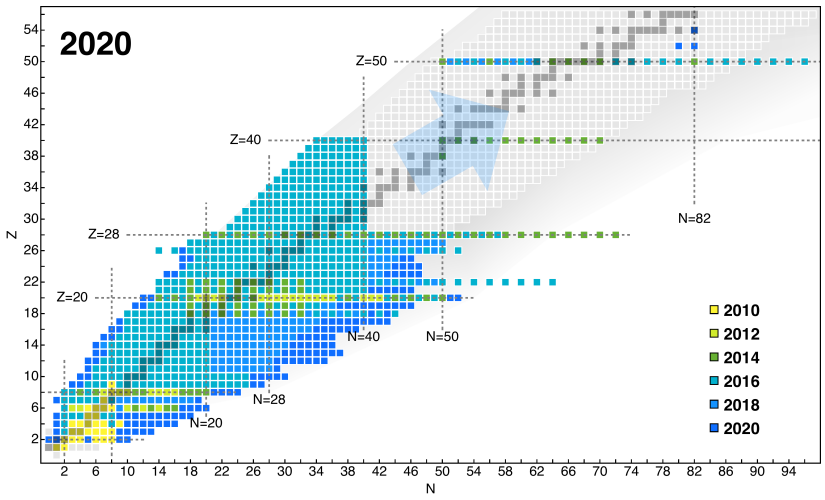

Figure 1.2.: Excerpt of the nuclear chart which shows the progress made in ab initio nuclear structure calculations over the past decade. The blue arrow indicates nuclei that will become accessible in the near future. Figure taken from Ref. [9]

model-independent and systematically improvable manner. This approach is called halo effective field theory (Halo EFT) [13]–[15]. It is a complementary approach to *ab initio* methods which have difficulties in describing weakly bound states.

In this thesis, the electroweak properties of halo nuclei are investigated. We start in Chapter 2 with a short introduction of halo nuclei and discuss their phenomenology. Basic concepts of nonrelativistic scattering, universality, and EFTs are covered in Chapter 3. In Chapter 4, electromagnetic (EM) transitions and static properties of halo nuclei are discussed and applied to the one-neutron halo nucleus ^{15}C. Thereby, we explain the Halo EFT formalism of the $1/2^+$ ground state as well as of the first excited $5/2^+$ state. Since the latter state is predominantly bound in a D-wave, we discuss in detail how to extend the formalism to higher partial waves in Cartesian coordinates. Chapter 5 provides an alternative approach to describe halo nuclei bound in higher partial waves, the spherical formalism. It is suited for the inclusion of higher partial waves since it uses the correct number of degrees of freedom by construction. In Chapter 6, electromagnetic breakup reactions as well as the structure of the one-neutron halo nucleus ^{31}Ne are investigated. In Chapter 7, we consider the weak decay of halo nuclei. More specifically, we discuss the beta-delayed proton emission from ^{11}Be and predict the branching ratio of the decay

into the continuum via a recently discovered resonance in ^{11}B. Chapter 8 discusses universality in charged halos in three- and one-dimensional space. In particular, we focus on S-wave one-proton halo nuclei and study the power counting of the Halo EFT and the implications on the universal properties. We conclude with a summary and an outlook.

2. Phenomenology of Halo Nuclei

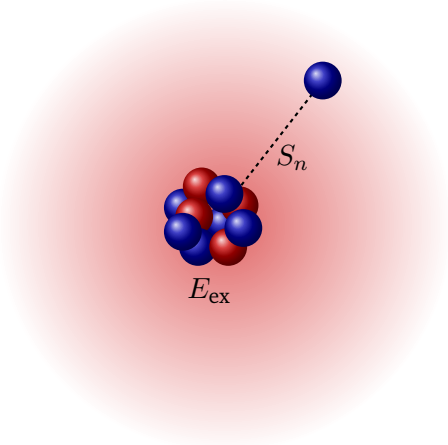

Figure 2.1.: Schematic of the one-neutron halo nucleus ^{11}Be. Compared to the excitation energy of the core $E_{\text{ex}} \approx 3.4$ MeV [16], the neutron separation energy $S_n \approx 500$ keV [17] is unnaturally small leading to the emergence of the halo structure.

Halo nuclei display a large separation of scales apparent through the small separation energy of the loosely bound valence nucleon in contrast to the comparatively high binding and excitation energies of the core. This separation leads to the emergence of the halo structure which can be considered a consequence of the quantum tunneling of halo nucleons out of the core potential to the classically forbidden region. In Fig. 2.1, ^{11}Be is sketched as an example for a one-neutron halo nucleus. In this case, the unnaturally small separation energy is given by $S_n \approx 500$ keV [17] while the excitation energy of the core is $E_{\text{ex}} \approx 3.4$ MeV [16].

2.1. Halos in Higher Partial Waves

The interaction between the constituents of a halo nucleus can in general be any higher partial wave interaction. However, due to the centrifugal barrier, lower partial waves

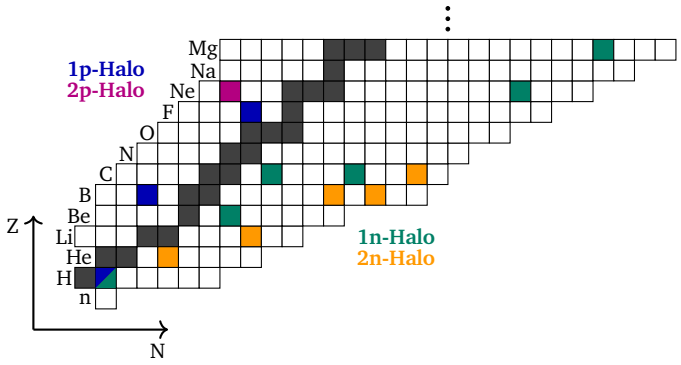

Figure 2.2.: Beginning of the nuclear chart according to Ref. [18]. The valley of stability is depicted in black and the different halo nuclei in different colors, respectively. The halo states of some nuclei are discussed in the community [19], [20].

are energetically favored. In nature, we find halo nuclei that are mostly bound in an S-, P- or a D-wave while the possibility of finding halo nuclei decreases going to higher partial waves. For example, the ground state of ^{11}Be is bound in an S-wave, ^{31}Ne is a halo nucleus predominantly bound in a P-wave while the first excited $5/2^+$ state of ^{15}C represents a D-wave halo nucleus.

2.2. Halos with Coulomb Interaction

Compared to neutron halo nuclei, proton halos interact via the repulsive Coulomb force in addition to the strong interaction which binds the system. It means that not only the strong interaction is responsible for the emergence of the halo structure but the delicate interplay between those two forces. The Coulomb barrier confines the protons to a small region around the core. This is the reason why proton halos are less common in nature as can be seen in the nuclear chart depicted in Fig. 2.2. The Coulomb interaction introduces an additional length scale D (or momentum scale k_C) and leads to possible modifications of the power counting depending on the magnitude of D and the Coulomb-modified scattering length a_C. This modification leads to a new classification of the universal regimes for proton halos characterized by the different hierarchies of the scattering length a_C and D. In Chapter 8, we investigate this modification in three- as well as one-dimensional space.

3. Theoretical Background

In this Chapter, we briefly summarize the basic concepts of nonrelativistic scattering theory relevant for this thesis. In particular, we discuss scattering at low energies near the scattering threshold. Thereby, we will show how the number of degrees of freedom in this energy regime can be reduced leading to an effective picture that is simpler but still sufficient for an adequate description of the scattering process. We introduce some formal scattering theory with a focus on two-body short-range potentials. These are the appropriate potentials for the parametrization of the underlying fundamental interaction because they capture the short-distance physics of that interaction. Since in this thesis we also discuss systems of charged particles, we show the implications due to corrections because of the long-ranged Coulomb interaction as well. Finally, we give a short introduction into effective field theories that enables to use the appropriate degrees of freedom at a certain energy scale in a systematic and improvable manner.

3.1. Low-Energy Physics

The theoretical description of nuclei on a fundamental level constitutes a major challenge. It represents a very complicated quantum-mechanical many-body process between all the particles of the standard model (quarks, leptons, etc.). The corresponding calculations are computationally exhausting and reach their limitations very fast.

However, low-energy phenomena do not probe physics at high energies or short distances. The physics beyond the low-energy regime cannot be resolved because the *de Broglie* wave length $\lambda = 2\pi/p$ corresponding to a typical small momentum p is larger than the short-distance structure. This implies that it is only necessary to include the relevant degrees of freedoms given by cluster states, i.e., by nucleons, nuclei, or even atoms. Fortunately, this reduces the complexity to the one of a few-body problem.

Whenever the typical small momentum p of a single particle is smaller than its rest mass m, we expand the relativistic dispersion relation

$$E = \sqrt{\boldsymbol{p}^2 + m^2} = m + \frac{\boldsymbol{p}^2}{2m} + \mathcal{O}\left(\boldsymbol{p}^4/m^3\right) \tag{3.1}$$

and neglect relativistic corrections.

3.2. Short-Range Interactions

The time-independent Schrödinger equation for a two-body system with reduced mass μ interacting via an isotropical potential $V(r)$ with $r = |\boldsymbol{r} - \boldsymbol{r}'|$ denoting the distance between the particles is given by

$$\left[-\frac{\Delta_r}{2\mu} + V(r) - E\right]\psi(\boldsymbol{r}) = 0\,. \tag{3.2}$$

Here, $\psi(\boldsymbol{r})$ denotes the wave function that is a solution to a state with energy E. Since the potential is spherically-symmetric, the wave function can be separated as

$$\psi(\boldsymbol{r}) = \psi_{lm}(\boldsymbol{r}) = R_l(r)Y_{lm}(\theta,\phi) = \frac{u_l(r)}{r}Y_{lm}(\theta,\phi), \tag{3.3}$$

where (l, m) are the angular momentum quantum numbers, $Y_{lm}(\theta,\phi)$ the spherical harmonics and $u_l(r)$ is the radial wave function. The corresponding radial Schrödinger is given by

$$-\frac{\mathrm{d}^2}{\mathrm{d}r^2} + \frac{l(l+1)}{r^2} + 2\mu\left[V(r) - E\right]u_l(r) = 0\,. \tag{3.4}$$

We consider short-range potentials as the appropriate parametrizations of the underlying fundamental interactions. The reason for this is that these fundamental interactions only take place at very small distances. In a first approximation, we use a contact interaction given by a delta function. Corrections to that are then given by higher order derivatives of that contact interaction. This results in a derivative expansion of the potential

$$V(r) = C_0\delta^{(3)}(r) + C_2\boldsymbol{\nabla}_r^2\delta^{(3)}(r) + \cdots\,. \tag{3.5}$$

For low-energy scattering, higher order terms in that expansion are negligible as they introduce higher powers of momenta. Therefore, only the first few coefficients C_{2i} are relevant and are called low-energy coefficients (LECs) that reproduce certain low-energy observables such as the binding energy or scattering phase shifts.

3.3. Scattering Amplitude and Cross Section

In this Section, we introduce some formal scattering theory following the books by Sakurai and Taylor [21], [22]. For simplicity, we restrict ourselves to the scattering of two nonrelativistic, spinless particles that interact via an S-wave interaction. Later in this thesis, we will also consider particles with spin that not only interact in an S-wave but also in a P- and D-wave and will explain in more detail how to extend the formalism accordingly.

For elastic scattering of an incoming plane-wave state $|\boldsymbol{p}\rangle$, the total wave function at asymptotically large distances is given by a superposition of this plane wave and an outgoing spherical wave describing the effect of the scattering process:

$$\langle \boldsymbol{r}|\psi^+_{\boldsymbol{p}}\rangle = \psi^{(+)}_{\boldsymbol{p}}(\boldsymbol{r}) \overset{r\to\infty}{\sim} e^{i\boldsymbol{p}\cdot\boldsymbol{r}} + \frac{e^{ipr}}{r} f\left(\boldsymbol{p}', \boldsymbol{p}\right) , \tag{3.6}$$

where due to energy conservation $\boldsymbol{p}' = p\hat{r}$ with $\hat{r} = \boldsymbol{r}/r$. The function $f\left(\boldsymbol{p}', \boldsymbol{p}\right)$ is called the scattering amplitude. It is related to the *on-shell* T-matrix via

$$f\left(\boldsymbol{p}', \boldsymbol{p}\right) = -\frac{\mu}{2\pi} \langle \boldsymbol{p}'| \hat{T}(E = E_{\boldsymbol{p}}) |\boldsymbol{p}\rangle , \tag{3.7}$$

with $E_{\boldsymbol{p}} = p^2/(2\mu)$. For the *full off-shell* T-matrix, the three variables E, $\boldsymbol{p}$ and $\boldsymbol{p}'$ have no connection to each other and it reads

$$T(E; \boldsymbol{p}', \boldsymbol{p}) = \langle \boldsymbol{p}'| \hat{T}(E) |\boldsymbol{p}\rangle . \tag{3.8}$$

In case $|\boldsymbol{p}'| \neq |\boldsymbol{p}|$ and $\boldsymbol{p}'^2/(2\mu) = E$ or $\boldsymbol{p}'^2/(2\mu) = E$, the T-matrix is *half off-shell*. For the two-body observables only the on-shell T-matrix is relevant. However, the T-matrix is determined by the potential via the Lippmann-Schwinger equation, an integral equation involving the half off-shell T-matrix in the homogeneous part. Since for $\boldsymbol{p}' = p\hat{r}$ the scattering amplitude only depends on p and the angle θ between $\boldsymbol{p}$ and $\boldsymbol{r}$, it has an expansion in partial waves

$$f\left(\boldsymbol{p}', \boldsymbol{p}\right) = \sum_{l=0}^{\infty} (2l+1) f_l(p) P_l(\cos\theta) , \tag{3.9}$$

where $P_l(\cos\theta)$ are the Legendre polynomials and the $f_l(p)$ are the partial-wave scattering amplitudes

$$\begin{aligned} f_l(p) &= \frac{e^{2i\delta_l} - 1}{2ip} \\ &= \frac{1}{p\cot\delta_l - ip} , \end{aligned} \tag{3.10}$$

with $\delta_l = \delta_l(p)$ being the phase shift as it will be discussed in Eq. (3.13).

The quantity that is experimentally accessible is the differential cross section which is directly related to the scattering amplitude

$$\frac{\mathrm{d}\sigma}{\mathrm{d}\Omega}\left(\boldsymbol{p}', \boldsymbol{p}\right) = \left|f\left(\boldsymbol{p}', \boldsymbol{p}\right)\right|^2 . \tag{3.11}$$

Note that $|\boldsymbol{p}'| = |\boldsymbol{p}|$. From the above expression and by using Eq. (3.9) we see that in general all partial waves contribute to the cross section requiring an infinite number of low-energy parameters. Fortunately, at low energies, only the low l contributions dominate because of the centrifugal barrier $\sim l(l+1)/r^2$. This can also be understood from the low-energy behavior of the phase shifts δ_l. As it will be described in Eq. (3.13), the expression $p^{2l+1}\cot\delta_l$ has to be constant in the limit $p \to 0$. This implies

$$\delta_l \propto p^{2l+1} , \tag{3.12}$$

meaning that indeed the low l contributions dominate the scattering processes at low energies.

3.4. Phase Shift and Effective Range Expansion

The relevant parameters describing a scattering process are the scattering phase shift and the effective range expansion parameters. In the presence of short-range interactions, they are related to each other through the effective range expansion (ERE)

$$p^{2l+1}\cot\delta_l = -\frac{1}{a_l} + \frac{1}{2}r_l p^2 + \cdots , \tag{3.13}$$

where a_l and r_l are the scattering and effective range parameters, respectively. The ellipses stand for higher-order terms ($\propto p^4, p^6, \cdots$) that are suppressed for low-energy scattering. In subsequent Chapters, we will consider S-, P- and D-wave interactions, meaning that we apply Eq. (3.13) for the cases of $l = 0, 1, 2$. Note that the right hand side of Eq. (3.13) is an analytic function in p^2 and thus of the energy. In Chapter 8, we will go into detail how this ERE is modified once we include Coulomb interactions which are relevant for the description of charged systems.

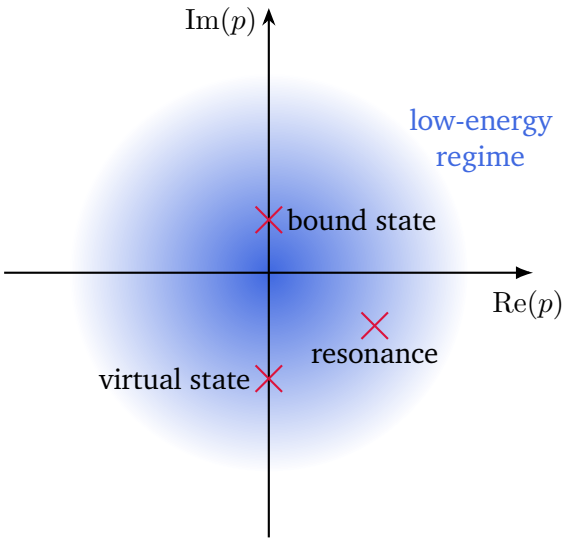

Figure 3.1.: The complex p-plane. Bound states occur on the positive imaginary axis with $p = i\gamma$, virtual states are on the negative imaginary axis, while resonances lie in the fourth quadrant. States in the low-energy regime (blue) are called shallow.

3.5. Bound States

In the complex momentum plane, two-body bound states with angular momentum l can be identified as poles of the partial wave scattering amplitude on the positive imaginary axis at $p = i\gamma$ with $\gamma > 0$. This corresponds to a negative relative energy

$$E = \frac{p^2}{2\mu} < 0\,. \tag{3.14}$$

The bound state condition for the scattering phase shift δ_l is given by

$$\cot \delta_l(p = i\gamma) = i\,. \tag{3.15}$$

Two-body states with a pole on the negative imaginary axis are called virtual states while resonant states live in the fourth quadrant. The pole structure is depicted in Fig. 3.1

3.6. Universality

For low-energy scattering (and thus small scattering momenta p) the details of any underlying interaction with a short range R are not resolved at sufficiently low eneriges. The reason for this is that the corresponding *de Broglie* wavelength $\lambda = 2\pi/p$ is too large to probe the spatial extent of the scattering center. This means that already a few low-energy parameters suffice in order to capture the low-energy phenomena in the presence of any short range potential, independently of its details. The scattering process can be described universally using only a few low-energy paramters, namely the effective range parameters appearing in the effective range expansion in Eq. (3.13).

In the case of a two-body system that interacts in an S-wave, only one parameter suffices for an adequate description at sufficiently low energies. This parameter is given by the scattering length a_0. Such a system exhibits universal properties described by this quantity. For a shallowly bound two-body state for example, the binding energy B as well as the mean square separation $\langle r^2 \rangle$ are given by

$$B = \frac{1}{2\mu a_0^2}\,, \tag{3.16}$$

$$\langle r^2 \rangle = \frac{1}{2a_0^2}\,. \tag{3.17}$$

However, going to higher and higher partial waves requires more and more low-energy parameters as will be discussed in Chapter 4. The necessity of an increasing number of effective range expansion parameters for the adequate description of the scattering process gives rise that the impact of the short range potential on low-energy phenomena increases. Since in that case, the universal properties are in general parametrized by more than one parameter, we call these systems less universal.

Similar to interactions in higher partial waves, also interactions via the Coulomb force among charged particles lead to modifications of the universal behavior. This will be discussed in more detail in Chapter 8.

3.7. Effective Field Theory

In this Section, we describe the general procedure of constructing an effective field theory in order to describe a physical system that comes along with a separation of

scales at a certain energy scale of interest. It means that the system either exhibits physics that is resolved at the energy scale under consideration or physics that can only be probed at higher energies. This scale separation determines the appropriate degrees of freedom. These fields are the ingredients to construct the most general possible Lagrangian. According to the fundamental theorem by Weinberg [23], this Lagrangian has to obey general principles as unitarity, analyticity, cluster decomposition and any other symmetries that appear in the system of interest. In general, the Lagrangian consists of infinitely many interaction terms in addition to the kinetic terms. However, due to the scale separation, it is possible to order those terms by their relative importance. This ordering is usually referred to as the *power counting* of the EFT. Once the most relevant terms are identified, only a few *low-energy constants* parametrizing these terms remain. They can be determined by *matching* calculated observables to experimental results for example. After that, other unknown observables that are accessible in the EFT can pe predicted with a theoretical uncertainty determined by the estimation of neglected higher order terms according to the power counting.

3.7.1. Halo EFT

The scale separation in Halo EFT for a one-nucleon halo nucleus is apparent through the the small separation energy between the loosely bound valence nulceon in contrast to the high binding and excitation energies of the core. For low-energy scattering, the internal structure of the core is not resolved and therefore the relevant degrees of freedom are given by the core and the valence nucleon. For a one-neutron halo nucleus that is bound in an S-Wave, one isotropic interaction is introduced that is resummed to all orders. This interaction generates the shallow bound state of the halo nucleus. In this thesis, we work in the dimer formalism, meaning that we introduce this interaction using an auxiliary two-body field, the so-called dimer field. Up to higher order, this approach is equivalent to the one without dimer fields. Calculating for example the binding energy of that nucleus allows to determine the low-energy constant that parametrizes the interaction. Then we can use this low-energy constant to make predictions and calculate further observables such as the mean square radius including a theoretical uncertainty according to the neglection of higher order terms.

4. EM Transitions and Structure of ^{15}C

In this Chapter, we present the Halo EFT formalism for ^{15}C and apply it to investigate electromagnetic transitions within ^{15}C as well as its structure. Parts of this Chapter have been published in this or similar form in our publication "Electric structure of shallow D-wave states in Halo EFT" in *J. Phys. G*, vol. 46, no. 11, p. 115 101 [24]. In Section 4.1, we show the non-relativistic Lagrangian for the S- and D-wave case. Using a momentum cutoff as regularization scheme to identify all divergences, we then calculate the dressed S- and D-wave propagators. For practical calculations, the power divergence subtraction scheme [25], [26] is applied for convenience. Based on our analysis of the divergence structure, we propose a power counting scenario and discuss its implications for higher partial wave bound states in terms of universality. In Ref. [27], the same power counting as in this Chapter is applied in order to describe shallow D-wave bound states in ^{17}C. After the inclusion of electric interactions in our theory, the B(E2) transition strength between the S- and D-wave state as well as electric form factors of the D-wave state are calculated in Section 4.2. First, we present general results and correlations for such weakly-bound systems and then apply them to the case of ^{15}C. Eventually, our Halo EFT results for ^{15}C are combined with data for the B(E2) transition strength [28] and *ab initio* results from the Importance-Truncated No-Core Shell Model (IT-NCSM) [29]. In this way, we are able to predict the quadrupole and hexadecapole moments and radii. Our findings are then compared to correlations [30] which are motivated by the rotational model of Bohr and Mottelson [31]. In Section 4.3, we present our conclusions.

Halo nuclei display a large separation of scales leading to the emergence of a halo structure. They consist of a tightly bound core nucleus surrounded by one or more weakly bound nucleons [32], [33]. This separation of scales can be expressed in terms of the core length scale, R_{core}, and the halo scale, R_{halo}, with $R_{halo} \gg R_{core}$. Halo EFT exploits this separation of scales to describe halo nuclei [13], [14] and uses the relevant degrees of freedom, the core and the halo nucleons. It is complementary to *ab initio* methods that have difficulties describing weakly-bound states and provides a useful

tool to identify universal correlations between observables. For recent reviews of Halo EFT see Refs. [15], [34], [35].

The Halo EFT formalism has been successfully used to study various reactions and properties of halo-like systems. Some early examples in the strong sector include the $n\alpha$ resonance in ^{5}He [13], [14] the $\alpha\alpha$ resonance in ^{8}Be [36] and universal properties, matter form factors and radii of two-neutron halo nuclei with predominantly S-wave [37], [38] and P-wave interactions [39], [40]. Due to the importance of higher partial waves in halo nuclei, different power counting schemes are conceivable that have a varying number of fine-tuned parameters [13], [14]. From naturalness assumptions, one expects a lower number of fine tunings to be more likely to occur in nature. However, the level of fine tuning depends strongly on the details of the considered system and has to be verified and adjusted to data.

In Halo EFT, electromagnetic interactions can be straightforwardly included via minimal substitution in the Lagrangian, and relevant electromagnetic currents can be added. Some applications to one-neutron halos, which we consider here, are the calculation of electric properties of ^{11}Be [41], ^{15}C [42], radiative neutron capture on ^{7}Li [43], [44] and ^{14}C [45], the ground state structure of ^{19}C [46], and the electromagnetic properties of ^{17}C [27]. The parameters needed as input in Halo EFT can be either taken from experiment or from *ab initio* calculations [44], [47], [48], which shows the versatility and complementary character of Halo EFT.

Electric properties provide a unique window on the structure and dynamics of one-neutron halo nuclei. We consider ^{15}C as an example and follow the approach presented in Ref. [41], where electric properties of ^{11}Be are calculated using Halo EFT. ^{15}C also has two bound states. The $\frac{1}{2}^+$ ground state of ^{15}C is predominantly an S-wave bound state, and the $\frac{5}{2}^+$ first excited state predominantly a D-wave bound state. Therefore, we focus on the extension to partial waves beyond the P-wave, in general, and especially on the extension to D-wave states. We include the strong D-wave interaction by introducing a new dimer field and compute the E2 transition strength and electric form factors. In the context of the strong $d + t \leftrightarrow n + \alpha$ reaction, D-wave states were also investigated in Ref. [49]. We use a similar approach for dressing the D-wave propagator, but a different regularization scheme. This entails a different power counting scheme as will be discussed in more detail in the next Section.

4.1. Halo EFT Formalism

We apply the Halo EFT formalism for the electric properties of P-wave systems developed in Ref. [41] to shallow D-wave systems. Since we use our theory to describe ^{15}C which has a shallow S-wave state ($J^P = \frac{1}{2}^+$) and a shallow D-wave state ($J^P = \frac{5}{2}^+$), we also include an S-wave state in our theory.

4.1.1. Lagrangian

The relevant degrees of freedom are the core, a bosonic field c, and the halo neutron, a spinor field n. The strong S- and D-wave interactions are included through auxiliary spinor fields σ for the S-wave state and d for the D-wave states, respectively. Note, that we include only one d field in the Lagrangian below. In principle, there are two d fields for the $\frac{5}{2}^+$ and $\frac{3}{2}^+$ states, respectively. Summing over repeated spin indices, the effective Lagrangian can be written as

$$\begin{aligned}\mathcal{L} = {} & c^\dagger \left(i\partial_t + \frac{\nabla^2}{2M} \right) c + n^\dagger \left(i\partial_t + \frac{\nabla^2}{2m_n} \right) n + \sigma_s^\dagger \left[\eta_0 \left(i\partial_t + \frac{\nabla^2}{2M_{nc}} \right) + \Delta_0 \right] \sigma_s \\ & + d_m^\dagger \left[c_2 \left(i\partial_t + \frac{\nabla^2}{2M_{nc}} \right)^2 + \eta_2 \left(i\partial_t + \frac{\nabla^2}{2M_{nc}} \right) + \Delta_2 \right] d_m \\ & - g_0 \left[c^\dagger n_s^\dagger \sigma_s + \sigma_s^\dagger n_s c \right] - g_2^J \left[d_m^\dagger \left[n \overset{\leftrightarrow}{\nabla}^2 c \right]_{J,m} + \left[c^\dagger \overset{\leftrightarrow}{\nabla}^2 n^\dagger \right]_{J,m} d_m \right] + \dots \,, \end{aligned} \tag{4.1}$$

where $3/2 \leq J \leq 5/2$ denotes the total spin of the D-wave state, m_n is the neutron mass, M the core mass and $M_{nc} = m_n + M$ is the total mass of the nc system. The repeated spin indices s and m are summed over according to the Einstein convention. The power counting for this Lagrangian depends on the underlying scales and will be discussed below. The S-wave part of Eq. (4.1) contains three coupling constants g_0, Δ_0 and η_0, while only two of them are linearly independent. In principle, we are free to choose which constant is set to a fixed value. Here, we choose $\eta_0 = \pm 1$ to be a sign which will be fixed by the effective range. (For an alternative choice, see Ref. [50].) This part is well known and has been discussed extensively in the literature on Halo EFT [15], [41], [42]. In order to make the presentation self-contained, the key equations for the interacting propagator of the S-wave state are collected in Appendix A.1. In the

following, we focus on the properties of the D-wave state. For the D-wave, we include four constants in our Lagrangian, namely c_2, η_2, Δ_2 and g_2. However, in this case only three of them are linearly independent. Again, we are free to choose which constant is set to a fixed value. Here, we choose $\eta_2 = \pm 1$ to be a sign, but other choices are possible. The additional 2nd-order kinetic term with constant c_2 is needed to renormalize the interacting D-wave propagator which contains up to quintic divergences. Since the core and neutron have different masses, it is convenient to define the interaction terms with Galilei invariant derivatives

$$n \overleftrightarrow{\nabla} c = n \, \frac{\left(M \overleftarrow{\nabla} - m_n \overrightarrow{\nabla} \right)}{M_{nc}} \, c \, , \tag{4.2}$$

where the arrows indicate the direction of their action. We project on the $J = 5/2$ or $3/2$ component of the interaction by defining

$$\left[n \overleftrightarrow{\nabla}^2 c \right]_{J,m} = \sum_{m_s m_l} \left(\frac{1}{2} m_s \; 2 m_l \middle| \, J m \right) \, n_{m_s} \sum_{\alpha\beta} \left(1\alpha \; 1\beta | \, 2 m_l \right) \frac{1}{2} \left(\overleftrightarrow{\nabla}_\alpha \overleftrightarrow{\nabla}_\beta + \overleftrightarrow{\nabla}_\beta \overleftrightarrow{\nabla}_\alpha \right) \, c \, , \tag{4.3}$$

where α and β are spherical indices and $\left(j_1 m_1 \; j_2 m_2 | \, J m \right)$ are Clebsch-Gordan coefficients [51] coupling j_1 and j_2 with projections m_1 and m_2, respectively, to J with projection m.

In practice, we calculate D-wave observables in Cartesian coordinates and then couple the spin and relative momentum in the appropriate way. For better distinction, we use Greek indices for the spherical representation and Latin indices for the Cartesian representation throughout this Chapter. The Cartesian form of the strong D-wave interaction is taken from Refs. [14], [49]

$$\frac{1}{2} \left(\overleftrightarrow{\nabla}_i \overleftrightarrow{\nabla}_j + \overleftrightarrow{\nabla}_j \overleftrightarrow{\nabla}_i \right) - \frac{1}{\mathrm{d} - 1} \overleftrightarrow{\nabla}^2 \delta_{ij} \, , \tag{4.4}$$

where d denotes the space-time dimension. This interaction yields 9 components, but a straightforward check shows that only 5 of them are linearly independent. Thus, the D-wave part of the Lagrangian (4.4) is Galilei invariant and contains the correct number of degrees of freedom.

The relation between spherical and Cartesian coordinates is given by

$$r_{\pm 1} = \mp (x_1 \pm i x_2)/\sqrt{2} \, , \quad r_0 = x_3 \, , \tag{4.5}$$

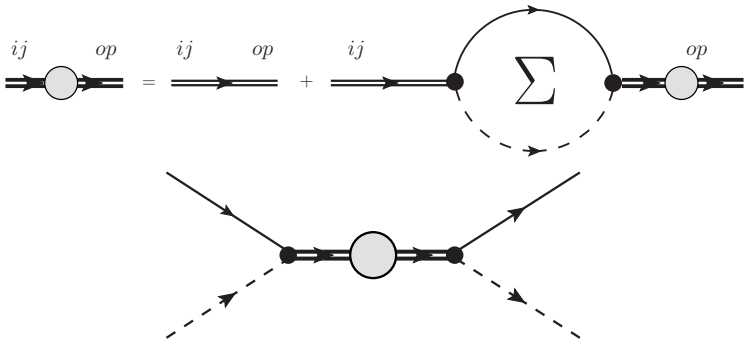

Figure 4.1.: The dashed line denotes the core field c and the thin solid line the neutron. The thin double line represents the bare dimer propagator and the thick double line with the gray circle is the dressed dimer propagator. The top panel shows the diagrammatic representation of the Dyson equation for the dressed dimer propagator and the bottom panel the neutron-core scattering amplitude with the dressed dimer propagator.

and similar relations apply to other quantities. For convenience, we will always use the Cartesian representation, but we will switch to a spherical basis if a coupling to definite angular momentum is required.

4.1.2. *D*-Wave Propagator

The dressed d propagator and the D-wave scattering amplitude are computed from summing the bubble diagrams in Fig. 4.1. This corresponds to the exact solution of the field theory defined by the terms explicitly shown in Eq. (4.1) for the D-wave state. In the next subsection, we will develop a power counting scheme that classifies the different contributions to the propagator according to their importance at low energies. After this scheme has been established, only the terms contributing to the considered order will be included. To make the divergence structure transparent, we will use a simple momentum cutoff to regularize the loop integrals. As before, we calculate the dressed D-wave propagator in the Cartesian representation and couple the neutron spin and the relative momentum to project out the appropriate angular momentum J in the end. The Dyson equation for the D-wave is illustrated in the top panel of Fig. 4.1 and

yields

$$D_d(p)_{ijop} = D_d(p)\ \frac{\left(\delta_{io}\delta_{jp} + \delta_{ip}\delta_{jo} - \frac{2}{3}\delta_{ij}\delta_{op}\right)}{2}\ , \tag{4.6}$$

$$D_d(p) = \frac{1}{\Delta_2 + \eta_2\left[p_0 - \mathbf{p}^2/(2M_{nc})\right] + c_2\left[p_0 - \mathbf{p}^2/(2M_{nc})\right]^2 - \Sigma_d(p)}\ , \tag{4.7}$$

with the one-loop self-energy

$$\Sigma_d(p)_{ijop} = \Sigma_d(p)\ \frac{\left(\delta_{io}\delta_{jp} + \delta_{ip}\delta_{jo} - \frac{2}{3}\delta_{ij}\delta_{op}\right)}{2}\ , \tag{4.8}$$

$$\begin{aligned}\Sigma_d(p) = &-\frac{m_R g_2^2}{15\pi}\left[\frac{2}{5\pi}\Lambda^5 + \frac{2}{3\pi}(2m_R)\left(p_0 - \frac{p^2}{2M_{nc}}\right)\Lambda^3\right.\\ &\left. + \frac{2}{\pi}(2m_R)^2\left(p_0 - \frac{p^2}{2M_{nc}}\right)^2\Lambda + i(2m_R)^{5/2}\left(p_0 - \frac{p^2}{2M_{nc}}\right)^{5/2}\right]\ ,\end{aligned} \tag{4.9}$$

where $m_R = (m_n M)/(m_n + M)$ denotes the reduced mass of the neutron-core system and Λ is a momentum cutoff. In spherical coordinates the Cartesian tensor [49]

$$\frac{\left(\delta_{io}\delta_{jp} + \delta_{ip}\delta_{jo} - \frac{2}{3}\delta_{ij}\delta_{op}\right)}{2}\ , \tag{4.10}$$

transforms to

$$\sum_{\alpha\beta\gamma\delta}\left(1\alpha\ 1\beta\right|2m_l\left)\left(1\gamma\ 1\delta\right|2m_l'\right)\frac{\left(\delta_{\alpha\gamma}\delta_{\beta\delta} + \delta_{\alpha\delta}\delta_{\beta\gamma} + \delta_{\alpha-\beta}(-1)^{\beta}\delta_{\gamma-\delta}(-1)^{\delta}\right)}{2} = \delta_{m_l,m_l'}\ , \tag{4.11}$$

and eventually, the full angular momentum coupling (4.3) applied in the incoming and outgoing channel yields

$$\begin{aligned}\Sigma_d(p)_{mm'} &= \sum_{m_s m_l m_s' m_l'}\left(\frac{1}{2}m_s\ 2m_l\middle|\,Jm\right)\left(\frac{1}{2}m_s'\ 2m_l'\middle|\,Jm'\right)\delta_{m_l m_l'}\delta_{m_s m_s'}\Sigma_d(p)\\ &= \delta_{mm'}\Sigma_d(p)\ ,\end{aligned} \tag{4.12}$$

where m_s (m_s') and m_l (m_l') are the spin projections of the created (annihilated) neutron and the projections of the D-wave interaction at both vertices of the bubble diagram in Fig. 4.1, respectively. Moreover, J denotes the total spin with its incoming and outgoing

projections m and m', respectively. The D-wave scattering amplitude in the two-body center-of-mass frame with $E = k^2/(2m_R)$ and $k = |\mathbf{p}'| = |\mathbf{p}|$ for on-shell scattering

$$t_2(\mathbf{p}', \mathbf{p}; E) = g_2^2 \left[\left(\mathbf{p} \cdot \mathbf{p}' \right)^2 - \frac{1}{3} \mathbf{p}^2 \mathbf{p}'^2 \right] D_d(E, \mathbf{0}) \ , \tag{4.13}$$

is matched to the effective range expansion

$$t_2(\mathbf{p}', \mathbf{p}; E) = \frac{15\pi}{m_R} \frac{\left(\mathbf{p} \cdot \mathbf{p}' \right)^2 - \frac{1}{3} \mathbf{p}^2 \mathbf{p}'^2}{1/a_2 - \frac{1}{2} r_2 k^2 + \frac{1}{4} \mathcal{P}_2 k^4 + ik^5} \ , \tag{4.14}$$

and we find the matching relations

$$\frac{1}{a_2} = \frac{15\pi}{m_R g_2^2} \Delta_2 + \frac{2}{5\pi} \Lambda^5 \ , \quad r_2 = -\frac{15\pi}{m_R^2 g_2^2} \eta_2 - \frac{2}{3\pi} \Lambda^3 \ , \quad \mathcal{P}_2 = \frac{15\pi}{m_R^3 g_2^2} c_2 + \frac{2}{\pi} \Lambda \ , \tag{4.15}$$

which determine the running of the coupling constants g_2, Δ_2, and c_2 with the cutoff Λ. Since we get Λ dependencies with powers of 5, 3, and 1, the effective range parameters a_2, r_2, and $\mathcal{P}_2$ are required for renormalization at LO. This pattern motivates our power counting scheme discussed below. In particular, we include the 2nd-order kinetic term proportional to c_2 (cf. Ref [52]) in (4.1) in order to absorb the quintic divergence. If the values for these ERE parameters are known, they can be used to fix the EFT couplings Δ_2, c_2 and g_2 in our theory.[1] In the vicinity of the bound state pole, the dressed d propagator can be written as

$$\begin{aligned} D_d(p) &= Z_d \ \frac{1}{p_0 - \frac{\mathbf{p}^2}{2M_{nc}} + B_2} + R_d(p) \ , \\ Z_d &= -\frac{15\pi}{m_R^2 g_2^2} \ \frac{1}{r_2 + \mathcal{P}_2 \gamma_2^2 - 5\gamma_2^3} \ , \end{aligned} \tag{4.16}$$

where Z_d denotes the wave-function renormalization, $B_2 = \gamma_2^2/(2m_R)$ denotes the binding energy with the binding momentum $\gamma_2 \sim 1/R_{halo}$, and $R_d(p)$ is the remainder which is regular at the pole. The pole condition gives the relation between the effective range parameters a_2, r_2, $\mathcal{P}_2$ and the binding momentum γ_2

$$\frac{1}{a_2} + \frac{1}{2} r_2 \gamma_2^2 + \frac{1}{4} \mathcal{P}_2 \gamma_2^4 = 0 \ . \tag{4.17}$$

[1] Note that we chose η_2 to be a sign.

4.1.3. Power Counting

For the shallow S-wave state, we adopt the standard power counting from pionless EFT [25], [26], [53], [54]. This implies the scaling $1/\gamma_0 \sim a_0 \sim R_{halo}$ and $r_0 \sim R_{core}$, where $\gamma_0 = (1 - \sqrt{1 - 2r_0/a_0})/r_0$ is the bound/virtual state pole position, a_0 the scattering length, and r_0 the effective range. As a result, r_0 contributes at next-to-leading order (NLO) in the expansion in R_{core}/R_{halo}.

Because more effective range parameters are involved, the power counting for shallow states in higher partial waves is not unique and different scenarios are conceivable [13], [14]. We apply the constraint that our scheme should exhibit the minimal number of fine tunings in the coupling constants required to absorb all power law divergences. This is motivated by the expectation that every additional fine tuning makes a scenario less likely to be found in nature, as discussed by Bedaque et al. in Ref. [14]. They explicitly consider P-waves where both a_1 and r_1 enter at leading order (LO) and assume the scaling relations $a_1 \sim R_{halo}^2 R_{core}$ and $r_1 \sim 1/R_{core}$, while higher effective range parameters scale with the appropriate power of R_{core}. This scenario requires only one fine-tuned combination of coupling constants in contrast to the alternative scenario proposed in Ref. [13] which requires two. In this work, we follow the general arguments of Ref. [14] and apply them to the D-wave case.

To renormalize all divergences in the $D_d(p)$ propagator, Eq. (4.6), the effective range parameters a_2, r_2, and $\mathcal{P}_2$ are all required. In the minimal scenario thus two out of three combinations of coupling constants need to be fine-tuned, i.e. $a_2 \sim R_{halo}^4\, R_{core}$ and $r_2 \sim 1/(R_{halo}^2\, R_{core})$, while $\mathcal{P}_2 \sim 1/R_{core}$. With this scaling, all three terms contribute at the same order for typical momenta $k \sim 1/R_{halo}$. Higher effective range parameters scale with R_{core} only and thus are suppressed by powers of R_{core}/R_{halo}.

This means that the dominant contribution to the D-wave bound state, after resumming all bubble diagrams and appropriate renormalization, comes from the bare propagator. In particular, the general structure of the propagator near the bound state pole at $E = -B_d$,

$$D_d(E) = \frac{Z_d}{E + B_d} \quad + \quad \text{regular terms in } E\,, \tag{4.18}$$

with Z_d the wave function renormalization constant, is fully reproduced by the bare D-wave propagator. Furthermore, all imaginary parts, if present, appear in the regular part of the amplitude. With our assumptions about the scaling of a_2, r_2, and $\mathcal{P}_2$, the loop contributions are suppressed by R_{core}/R_{halo}. They can be treated in perturbation theory and contribute at NLO in the power counting. Thus, the low-energy D-wave scattering

amplitude will satisfy unitarity perturbatively in the expansion in R_{core}/R_{halo}. This is similar to the treatment of the excited P-wave bound state in Ref. [41].

We note that the power counting depends sensitively on the details of the considered system and thus has to be verified *a posteriori* by comparison to experimental information. Including S-waves and switching to the pole momentum γ_0 instead of the scattering length a_0, the relevant parameters in our EFT are γ_0, γ_2, r_2, and $\mathcal{P}_2$ at LO, and the following wave function renormalization constants for the D-wave state are obtained

$$Z_d^{\text{LO}} = -\frac{15\pi}{m_R^2 g_2^2}\,\frac{1}{r_2+\mathcal{P}_2\gamma_2^2} \quad \text{and} \qquad Z_d^{\text{NLO}} = -\frac{15\pi}{m_R^2 g_2^2}\,\frac{1}{r_2+\mathcal{P}_2\gamma_2^2}\left[1+\frac{5\gamma_2^3}{r_2+\mathcal{P}_2\gamma_2^2}\right] . \tag{4.19}$$

The corresponding constants for the S-wave state are given in Appendix A.1.

After we have identified the proper power counting, we switch to dimensional regularization with power divergence subtraction (PDS) with renormalization scale μ as our regularization scheme [25], [26]. This simplifies the calculations but still keeps the linear divergence associated with $\mathcal{P}_2$. In PDS, the one-loop self-energy for the D-wave state is given by

$$\Sigma_d(p) = -\frac{2}{15}\frac{m_R g_2^2}{2\pi}\,(2m_R)^2\left(p_0-\frac{p^2}{2M_{nc}}\right)^2\left[i\sqrt{2m_R\left(p_0-\frac{p^2}{2M_{nc}}+i\epsilon\right)}-\frac{15}{8}\mu\right] . \tag{4.20}$$

After matching to the effective range expansion, we find

$$\frac{1}{a_2} = \frac{15\pi}{m_R g_2^2}\Delta_2 , \quad r_2 = -\frac{15\pi}{m_R^2 g_2^2}\eta_2 , \quad \mathcal{P}_2 = \frac{15\pi}{m_R^3 g_2^2}c_2 + \frac{15}{2}\mu . \tag{4.21}$$

However, we note that the μ dependence in the matching condition for $\mathcal{P}_2 \sim 1/R_{core}$ is subleading for $\mu \sim 1/R_{halo}$. It appears only at NLO where it is required to absorb the divergence at this order. Our findings in the form factor calculation confirm this observation.

As pointed out in the beginning, an EFT for D-wave states was previously considered in the context of the reaction $d+t \leftrightarrow n+\alpha$ in Ref. [49], where the coupling of the auxiliary field for the ^{5}He resonance to the αn pair with spin $3/2$ involves a D-wave. We note that in Ref. [49] the minimal subtraction (MS) scheme was used, in which all power law divergences are automatically set to zero and no explicit renormalization is

required for the D-wave propagator. As argued in Refs. [25], [26], [53], [54], the MS scheme is not well suited for systems with shallow bound states since the tracking of power law divergences is important. If MS is used in the D-wave case, the contributions of r_2 and $\mathcal{P}_2$ appear shifted to higher orders. Using a momentum cutoff scheme for the D-wave propagator, it becomes clear that contact interactions corresponding to r_2 and $\mathcal{P}_2$ are also required to absorb all divergences at leading order. As a consequence, these parameters have to be enhanced by the halo scale R_{halo}.

4.1.4. Higher Partial Waves

It is straightforward to extend our power counting arguments to partial waves beyond the D-wave. The higher-l interaction terms can be derived from the Cartesian (Buckingham) tensors [55], [56], which are symmetric and traceless in every pair of indices and are given by

$$M^{(l)}_{i,j,\cdots,t} = \frac{(-1)^l}{l!} r^{2l+1} \frac{\partial^l}{\partial x_i \partial x_j \cdots \partial x_t} \left(\frac{1}{r}\right) \qquad i,j,\cdots,t \in \{1,2,3\} \tag{4.22}$$

with $r = \sqrt{x_1^2 + x_2^2 + x_3^2}$. To obtain the specific interaction in momentum space for a given angular momentum l, r_j is simply replaced by $i\nabla_j$. In general, this leads to a tensor of rank l with 3^l components. However, because the tensors are symmetric and traceless in every pair of indices, only $[(2+l)(1+l)..3]/l! - l(l-1)/2 = 2l+1$ components are linearly independent. Thus, we obtain the correct number of linearly independent components for a given partial wave. However, beyond P-waves it becomes beneficial to use spherical representation for calculations depending on the considered observable.

In order to be able to absorb all power law divergences, the first $(l+1)$ effective range parameters are needed at LO for the l-th partial wave [13]. As discussed in the previous subsection, one of these parameters can be assumed to scale only with R_{core} if $l \geq 1$. Thus, we need l fine-tuned parameters for the l-th partial wave if we want to renormalize all power law divergences assuming the minimal fine tuning scenario. For arbitrary l,

this leads to the following power counting scheme

$$a_l = \begin{cases} R_{halo}, & l = 0 \\ R_{halo}^{2l}\, R_{core}, & l > 0 \end{cases} \tag{4.23}$$

$$r_l = \begin{cases} R_{core}, & l = 0 \\ 1/\left(R_{halo}^{2l-2}\, R_{core}\right), & l > 0 \end{cases} \tag{4.24}$$

$$\mathcal{P}_l = \begin{cases} R_{core}^{3-2l}, & l \leq 1 \\ 1/\left(R_{halo}^{2l-4}\, R_{core}\right), & l > 1 \end{cases} \tag{4.25}$$

$$\vdots\,,$$

where the l-th and higher effective range parameters in each partial wave scale with appropriate powers of R_{core}. Accordingly, our power counting scenario agrees with Ref. [14] up to P-waves but differs beyond that because the higher effective range parameters are counted differently. The condition that all power law divergences in the bubble diagram can be absorbed is relaxed and only a_l and r_l contribute at LO for arbitrary $l > 0$. As a consequence, only one fine tuning is required. If this counting is universally realized in nature, one would expect an approximately equal number of shallow states in low and high l-waves. Since experimental observation of shallow states in light nuclei is predominated by lower l-waves, we expect our counting to be more realistic. Later in our calculations for ^{15}C we compare both power countings and reveal that our scenario is more compatible with data in this case.

4.2. Electric Observables

In this Section, we use the Lagrangian (4.1) with minimal substitution plus the local, gauge invariant operators to compute the D-wave form factors and the E2 transition from the S- to the D-wave states. Eventually, we apply our results to ^{15}C to predict several electric observables.

4.2.1. Electric Interactions

Electric interactions are included via minimal substitution in the Lagrangian

$$\partial_\mu \to D_\mu = \partial_\mu + ie\hat{Q}A_\mu \,, \tag{4.26}$$

where the charge operator $\hat{Q}$ acting on the ^{14}C core yields $\hat{Q}c = 6c$. Additionally to the electric interactions resulting from the application of the minimal substitution in the Lagrangian, we have to consider further local gauge invariant operators involving the electric field $\mathbf{E}$ and the fields c, n, σ and d. Depending on the observable and respective partial wave, they contribute at different orders of our EFT. The local operators with one power of the photon field, relevant in our calculation of electric form factors and the B(E2) transition strength, are

$$\begin{aligned}
\mathcal{L}_E = &- L_{C01}^{(d)}\, d_m^\dagger \left(\nabla^2 A_0 - \partial_0(\boldsymbol{\nabla}\cdot\mathbf{A})\right) d_m \\
&- L_{C02}^{(d)}\, d_{m'}^\dagger \left(\frac{1}{2} m_s\; 2m_{l'}\middle|\, Jm'\right)\left(\frac{1}{2} m_s\; 2m_l\middle|\, Jm\right)(1\alpha\; 1\beta|\, 2m_{l'})\,(1\gamma\; 1\delta|\, 2m_l) \\
&\quad \left[(\nabla_\alpha\nabla_\gamma\delta_{\beta\delta}A_0) - \left(\partial_0\frac{(\nabla_\alpha A_\gamma + \nabla_\gamma A_\alpha)}{2}\delta_{\beta\delta}\right)\right] d_m \\
&- L_{E2}^{(sd)}\sigma_m d_{m'}^\dagger \left(\frac{1}{2} m\; Jm'\middle|\, 2m_l\right)(1\alpha\; 1\beta|\, 2m_l)\left[\nabla_\alpha\nabla_\beta A_0 - \partial_0\frac{(\nabla_\alpha A_\beta + \nabla_\beta A_\alpha)}{2}\right],
\end{aligned} \tag{4.27}$$

where repeated spin indices are summed over.

These additional operators are necessary in order to renormalize our results in the electric sector. This means that up to a certain order within our power counting, ultraviolet divergences can only be removed through interactions as in Eq. (4.27). In particular, the interaction terms proportional to $L_{C01}^{(d)}$ and $L_{C02}^{(d)}$ are required in order to remove the divergences occurring in the loop diagram in Fig. 4.3. Since this loop diagram is a NLO contribution, the corresponding interaction terms are entering first at NLO. This procedure allows us to determine the highest possible order within our power counting scheme that the interactions in Eq. (4.27) have to enter in order to eliminate divergences.

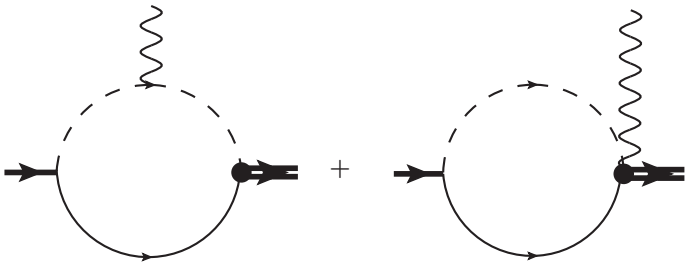

Figure 4.2.: The diagrams contributing to the irreducible vertex that determines the S-to-D state transition in Halo EFT. The thick double line denotes the dressed D-wave propagator and the thick single line the dressed S-wave propagator.

4.2.2. E2 Transition

The diagrams contributing to the irreducible vertex for the E2 transition from the S- to the D-wave state at LO are shown in Fig. 4.2. At higher order, the next contribution would be the counterterm $L_{E2}^{(sd)}$ from Eq. (4.27) which has to be fixed by experimental input. The interaction term proportional to $L_{E2}^{(sd)}$ is not required to cancel any divergence because the LO contributions to the B(E2) transition depicted in Fig. 4.2 are finite. Therefore, our minimal principle of including the counterterms when they are needed for renormalization cannot be used to determine its exact order beyond LO. Thus, we restrict ourselves to LO for the reduced E2 transition strength. This allows us to make predictions for other electric observables as discussed below.

The photon in Fig. 4.2 has a four momentum of $k = (\omega, \mathbf{k})$ and its polarization index is denoted by ν. The computation of the relevant diagrams yields a vertex function $\Gamma_{m'm_s\nu}$, where m' is the total angular momentum projection of the D-wave state and m_s denotes the spin projection of the S-wave state. Since the neutron spin is unaffected by this transition, we calculate the vertex function with respect to the specific components of the D-wave interaction

$$\Gamma_{m'm_s\nu} = \sum_{m_l} \left(\frac{1}{2} m_s \; 2m_l \middle| \, Jm' \right) \sum_{\alpha\beta} \left(1\alpha \; 1\beta | \, 2m_l \right) \tilde{\Gamma}_{\alpha\beta\nu} \; , \tag{4.28}$$

where J denotes the total spin of the D-wave state. In the case of $m_s = m' = \pm 1/2$,

only $m_l = 0$ contributes to the sum in Eq. (4.28) and we get for $J = 5/2$

$$\Gamma_{+\frac{1}{2}+\frac{1}{2}\,\nu} = \Gamma_{-\frac{1}{2}-\frac{1}{2}\,\nu} = \sqrt{\frac{2}{5}}\tilde{\Gamma}_{00\nu} \; + \sqrt{\frac{1}{10}}\tilde{\Gamma}_{1-1\nu} + \sqrt{\frac{1}{10}}\tilde{\Gamma}_{-11\nu} \; . \tag{4.29}$$

We calculate the irreducible vertex in Coulomb gauge so that we have $\mathbf{k} \cdot \epsilon = 0$ for real photons. In order to isolate the electric contribution to the irreducible vertex in a simple way, we choose $\mathbf{k} \cdot \mathbf{p} = 0$, where $\mathbf{p}$ denotes the incoming momentum of the S-wave state. Taking gauge invariance and symmetry properties into account, the space-space components of the vertex function in Cartesian coordinates can be written as

$$\tilde{\Gamma}_{ijk} = \Gamma_E \, \frac{1}{2} \left(k_j \delta_{ik} + k_i \delta_{jk} \right) \; + \; \Gamma_M \, p_k \left(k_i k_j \; - \frac{1}{3} \delta_{ij} k^2 \right) . \tag{4.30}$$

Choosing the photon to be traveling in the x_3 direction only Γ_E contributes to $\tilde{\Gamma}_{333}$, and we obtain

$$\tilde{\Gamma}_{333} = \Gamma_E \omega \; , \tag{4.31}$$

with $|\mathbf{k}| = k_3 = \omega$. By comparing the definitions for the transition rate depending on B(E2) and the transition rate as a function of the irreducible vertex Γ_E [57], we get the following relation

$$\text{B(E2: } 1/2^+ \to 5/2^+) = \frac{15}{\pi} \; \left(\frac{\Gamma_{+\frac{1}{2}+\frac{1}{2}\,0}}{\omega^2} \right)^2 \; .$$

Evaluating this using Eqs. (4.29, 4.31), it follows that $\Gamma_{+\frac{1}{2}+\frac{1}{2}\,0} = \sqrt{2/5} \; \tilde{\Gamma}_{333}$ and we obtain

$$\text{B(E2: } 1/2^+ \to 5/2^+) = \; \frac{6}{\pi} \; \left(\frac{\bar{\Gamma}_E}{\omega} \right)^2 \; ,$$

with the renormalized, irreducible vertex $\bar{\Gamma}_E = \sqrt{Z_\sigma Z_d} \, \Gamma_E$. At LO, Z_σ and Z_d are given in Eqs. (A.3) and (4.19), respectively. Using the result of our calculation of Γ_E for diagrams (a), we find at LO

$$\text{B(E2: } 1/2^+ \to 5/2^+) = \frac{4}{5\pi} \frac{Z_{\text{eff}}^2 e^2 \gamma_0}{-r_2 - \mathcal{P}_2 \gamma_2^2} \; \left[\frac{3\gamma_0^2 + 9\gamma_0\gamma_2 + 8\gamma_2^2}{(\gamma_0 + \gamma_2)^3} \right]^2 , \tag{4.32}$$

where γ_2, r_2, and $\mathcal{P}_2$ are the parameters of the $5/2^+$ state and the effective charge is $Z_{\text{eff}} = (m_n/M_{nc})^2 Q_c$. In general, the effective charge for arbitrary multipolarity λ is

given by $Z_{\text{eff}}^{(\lambda)} = Z_n \left(\frac{M}{M_{nc}}\right)^{\lambda} + Z_c \left(-\frac{m_n}{M_{nc}}\right)^{\lambda}$ [58]. In Halo EFT it comes automatically out of the calculation.

The same result for $\bar{\Gamma}_E$ can be obtained using current conservation,

$$\omega \tilde{\Gamma}_{ij0} = k_k \tilde{\Gamma}_{ijk} \,, \tag{4.33}$$

if we calculate the space-time components of the vertex function $\tilde{\Gamma}$. In contrast to $\tilde{\Gamma}_{ijk}$, we have to consider only the left diagram in Fig. 4.2 for $\tilde{\Gamma}_{ij0}$ at LO.

The calculation of the transition to the $3/2^+$ state can be carried out in the same way. The only difference is a relative factor of $2/3$ for B(E2) because of the different Clebsch-Gordan coefficient in Eq. (4.29)

$$\text{B(E2: } 1/2^+ \to 3/2^+) = \frac{8}{15\pi} \frac{Z_{\text{eff}}^2 e^2 \gamma_0}{-r_2 - \mathcal{P}_2 \gamma_2^2} \left[\frac{3\gamma_0^2 + 9\gamma_0\gamma_2 + 8\gamma_2^2}{(\gamma_0+\gamma_2)^3}\right]^2 , \tag{4.34}$$

where γ_2, r_2, and $\mathcal{P}_2$ are now the parameters of the $3/2^+$ state.

4.2.3. Form Factors

The result for the electric form factor of an S-wave halo state is discussed in Ref. [41] for ^{11}Be and in Ref. [42] for ^{15}C. The experimental result for the rms charge radius of ^{14}C is $\langle r_E^2 \rangle_{^{14}\text{C}}^{1/2} = 2.5025(87)$ fm [59] and the Halo EFT result for the $\frac{1}{2}^+$ S-wave ground state is $\langle r_E^2 \rangle_{^{15}\text{C}}^{(\sigma)} \approx 0.11$ fm^2 [42], but the authors do not quote an error for this number. In principle, both values can be combined to obtain a prediction for the full charge radius of the ^{15}C ground state.

Here, we focus on the form factors of the D-wave state in ^{15}C. The D-wave form factors can be extracted from the irreducible vertex for $A_0 dd$ interactions. The corresponding contributions are shown in Fig. 4.3 up to NLO. The first diagram represents three different direct couplings of the photon to the D-wave propagator. Two couplings emerge from the minimal substitution in the bare propagator proportional to r_2, $\mathcal{P}_2$ and contribute at LO. The last one is a term $\sim L_{C01/2}^{(d)}$ which comes out of Eq. (4.27) and is required for the renormalization of the loop divergences of diagram (b) and therefore contributes at NLO. The second diagram arises from minimal substitution in the core propagator and contributes at NLO. The computation is carried out in the Breit frame,

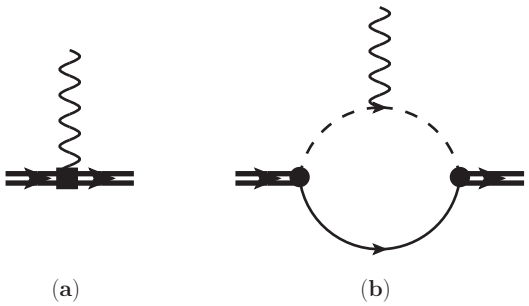

Figure 4.3.: The topologies contributing to the irreducible vertex for an A_0 photon coupling to the ^{14}C-neutron D-wave bound state up to NLO. Diagram (a) contains three different direct couplings. Two arise from minimal substitution in the bare propagator proportional to r_2, $\mathcal{P}_2$ and contribute at LO, while diagram (b) emerges from minimal substitution in the core propagator and contributes at NLO. The local gauge invariant operator $\sim L^{(d)}_{C01/2'}$ required for the renormalization of diagram (b), is also represented by diagram (a) and contributes at NLO. The thick double line denotes the dressed D-wave propagator.

$q = (0, \mathbf{q})$, and the irreducible vertex for the A_0 photon coupling to the D-wave state in Cartesian coordinates yields

$$\left\langle ij \left| J^0 \right| op \right\rangle = -ieQ_c \left[G_E(|\mathbf{q}|)\, E_{ij,op} + \frac{1}{2M_{nc}^2} G_Q(|\mathbf{q}|)\, Q_{ij,op} + \frac{1}{4M_{nc}^4} G_H(|\mathbf{q}|)\, H_{ij,op} \right] , \tag{4.35}$$

with the three-momentum of the virtual photon $\mathbf{q} = \mathbf{p}' - \mathbf{p}$ and three different D-wave tensors for each form factor $E_{ij,op} \sim q^0$, $Q_{ij,op} \sim q^2$ and $H_{ij,op} \sim q^4$. Note that we take out an overall factor of the elementary charge e from all form factors. As a consequence our definition of the quadrupole and hexadecapole moments does not contain a factor e. Evidently, the hexadecapole form factor is only observable for the $5/2^+$ D-wave state and unobservable for the $3/2^+$ state. This can be straightforwardly proven by considering the respective Clebsch-Gordan coefficients to couple the spin and angular momentum to total J for the two D-wave states in combination with $H_{ij,op}$ in spherical coordinates. For reasons of simplicity, the calculation is carried out in Cartesian coordinates and the

resulting Cartesian tensors are given below

$$\tilde{Q}_{ij,op} = \frac{1}{4}\left(q_j q_p \delta_{io} + q_j q_o \delta_{ip} + q_i q_p \delta_{jo} + q_i q_o \delta_{jp} - \frac{4}{3} q_i q_j \delta_{op} - \frac{4}{3} q_o q_p \delta_{ij} + \frac{4}{9} q^2 \delta_{ij}\delta_{op}\right) , \tag{4.36}$$

$$\tilde{H}_{ij,op} = \left(q_i q_j q_o q_p - \frac{1}{3} q^2 q_i q_j \delta_{op} - \frac{1}{3} q^2 q_o q_p \delta_{ij} + \frac{1}{9} q^4 \delta_{ij}\delta_{op}\right) , \tag{4.37}$$

$$E_{ij,op} = \frac{\left(\delta_{io}\delta_{jp} + \delta_{ip}\delta_{jo} - \frac{2}{3}\delta_{ij}\delta_{op}\right)}{2} , \tag{4.38}$$

$$Q_{ij,op} = \frac{3}{5}\tilde{Q}_{ij,op} - \frac{1}{5} q^2 E_{ij,op} , \tag{4.39}$$

$$H_{ij,op} = \frac{3}{2}\tilde{H}_{ij,op} - \frac{30}{35} q^2 \tilde{Q}_{ij,op} + \frac{3}{35} q^4 E_{ij,op} . \tag{4.40}$$

The Cartesian tensors $E_{ij,op}$, $Q_{ij,op}$ and $H_{ij,op}$ fulfill the following constraints

$$E_{ij,op}\, E_{ij,op} = 5, \qquad \delta_{ij}\, E_{ij,op} = \delta_{op}\, E_{ij,op} = 0 , \tag{4.41}$$

$$E_{ij,op}\, Q_{ij,op} = 0, \qquad \delta_{ij}\, Q_{ij,op} = \delta_{op}\, Q_{ij,op} = 0 , \tag{4.42}$$

$$E_{ij,op}\, H_{ij,op} = 0, \qquad Q_{ij,op}\, H_{ij,op} = 0, \qquad \delta_{ij}\, H_{ij,op} = \delta_{op}\, H_{ij,op} = 0 . \tag{4.43}$$

The neutron spin is unaffected by the charge operator up to the order considered here.

At LO, only the direct coupling from the minimal substitution in the bare D-wave propagator proportional to r_2 and $\mathcal{P}_2$, depicted in Fig. 4.3 (a), contribute. This reproduces the correct normalization condition of the electric form factor of $G_E(0) = 1$, but the form factor is just a constant. Therefore, there is no real prediction beyond charge conservation at LO.

At NLO, diagram (b) in Fig. 4.3 also contributes, and the counterterm is required for the renormalization of the loop divergences stemming from diagram (b). We then obtain

for the electric $G_E(|\mathbf{q}|)$, quadrupole $G_Q(|\mathbf{q}|)$ and hexadecapole $G_H(|\mathbf{q}|)$ form factors

$$G_E(|\mathbf{q}|) = \frac{1}{r_2 + \mathcal{P}_2\gamma_2^2}\left[\left(\tilde{L}_{C01}^{(d)} + \frac{4}{3}\tilde{L}_{C02}^{(d)}\right)|\mathbf{q}|^2 - \frac{21\gamma_2 f^2|\mathbf{q}|^2}{16} + \frac{\gamma_2^3}{4} + \gamma_2^2\mathcal{P}_2 + r_2 \right.$$
$$\left. - \arctan\left(\frac{f|\mathbf{q}|}{2\gamma_2}\right)\left(\frac{21f^3|\mathbf{q}|^3}{32} + \frac{13\gamma_2^2 f|\mathbf{q}|}{4} + \frac{\gamma_2^4}{2f|\mathbf{q}|}\right)\right], \tag{4.44}$$

$$G_Q(|\mathbf{q}|) = \frac{2M_{nc}^2}{r_2 + \mathcal{P}_2\gamma_2^2}\left[\frac{20}{3}\tilde{L}_{C02}^{(d)} - \frac{75\gamma_2 f^2}{14} - \frac{25\gamma_2^3}{7|\mathbf{q}|^2}\right.$$
$$\left. - \arctan\left(\frac{f|\mathbf{q}|}{2\gamma_2}\right)\left(\frac{75f^3|\mathbf{q}|}{28} + \frac{75\gamma_2^2 f}{14|\mathbf{q}|} - \frac{50\gamma_2^4}{7f|\mathbf{q}|^3}\right)\right], \tag{4.45}$$

$$G_H(|\mathbf{q}|) = \frac{2}{3}\,\frac{4M_{nc}^4}{r_2 + \mathcal{P}_2\gamma_2^2}\left[-\frac{45\gamma_2 f^2}{64|\mathbf{q}|^2} + \frac{45\gamma_2^3}{16|\mathbf{q}|^4}\right.$$
$$\left. - \arctan\left(\frac{f|\mathbf{q}|}{2\gamma_2}\right)\left(\frac{45f^3}{128|\mathbf{q}|} - \frac{15\gamma_2^2 f}{16|\mathbf{q}|^3} + \frac{45\gamma_2^4}{8f|\mathbf{q}|^5}\right)\right], \tag{4.46}$$

with $f = m_R/M$ while $\tilde{L}_{C01/2}^{(d)}$ represents the local gauge invariant operators from Eq. (4.27). These operators have a finite piece $L_{C01/2}^{(d)\,\text{fin}}$ as well as a μ-dependent part that cancels the renormalization scale dependence from the loop contribution. For a better readability, we have absorbed some prefactors in the definition of the counterterms and defined the low-energy constants

$$\tilde{L}_{C01}^{(d)} = \frac{15\pi}{eQ_c g_2^2 m_R^2} L_{C01}^{(d)\,\text{fin}}\,, \tag{4.47}$$

$$\tilde{L}_{C02}^{(d)} = \frac{15\pi}{eQ_c g_2^2 m_R^2} L_{C02}^{(d)\,\text{fin}}\,, \tag{4.48}$$

which are used in Eqs. (4.44, 4.45, 4.46). The remaining divergence emerging from the loop diagram in Fig. 4.3 is absorbed by $\mathcal{P}_2$ from the direct photon coupling in diagram (a). After the expansion of Eq. (4.44)

$$G_E(|\mathbf{q}|) \approx 1 - \frac{1}{6}\langle r_E^2\rangle\,|\mathbf{q}|^2 + \dots\,, \tag{4.49}$$

we obtain $G_E(0) = 1$ and an electric radius

$$\langle r_E^2\rangle^{(d)} \;=\; -\frac{12\tilde{L}_{C01}^{(d)} + 16\tilde{L}_{C02}^{(d)} - 35\gamma_2 f^2}{2\left(r_2 + \mathcal{P}_2\gamma_2^2\right)}\,, \tag{4.50}$$

such that the electric radius is not a prediction.

We expand Eq. (4.45) and (4.46)

$$\frac{1}{M_{nc}^2} G_Q(|\mathbf{q}|) \approx \mu_Q \left(1 - \frac{1}{6} \langle r_Q^2 \rangle |\mathbf{q}|^2 + \dots\right), \tag{4.51}$$

$$\frac{1}{M_{nc}^4} G_H(|\mathbf{q}|) \approx \mu_H \left(1 - \frac{1}{6} \langle r_H^2 \rangle |\mathbf{q}|^2 + \dots\right), \tag{4.52}$$

and find the respective multipole moments

$$\mu_Q^{(d)} = \frac{10\left(4\tilde{L}_{C02}^{(d)} - 5\gamma_2 f^2\right)}{3\left(r_2 + \mathcal{P}_2\gamma_2^2\right)}, \tag{4.53}$$

$$\mu_H^{(d)} = -\frac{2f^4}{3\gamma_2\left(r_2 + \mathcal{P}_2\gamma_2^2\right)}, \tag{4.54}$$

where we find the hexadecapole moment $\mu_H^{(d)}$ as a prediction. The electric radius $\langle r_E^2 \rangle^{(d)}$ and the quadrupole moment $\mu_Q^{(d)}$ are not predicted. They are used to fix the counterterms $L_{C02}^{(d)}$ and $L_{C01}^{(d)}$. The quadrupole and hexadecapole radii yield

$$\langle r_Q^2 \rangle^{(d)} = \frac{27 f^4}{7\gamma_2\left(4\tilde{L}_{C02}^{(d)} - 5\gamma_2 f^2\right)}, \tag{4.55}$$

$$\langle r_H^2 \rangle^{(d)} = \frac{9 f^2}{14\gamma_2^2}, \tag{4.56}$$

where the hexadecapole radius is predicted by Halo EFT and the quadrupole radius depends on the counterterm $L_{C02}^{(d)}$, fixed by the quadrupole moment. Thus, we can predict the quadrupole radius if the quadrupole moment is known.

Finally, we can reinsert the matching conditions, Eqs. (4.50, 4.53), into the results for the electric and quadrupole form factors, Eqs. (4.44, 4.45), in order to get expressions in terms of observables only.

4.2.4. Correlations Between Electric Observables

Up to this point, all results are universal and not specific for ^{15}C. In this Section, we explore universal relations between different observables for shallow D-wave bound

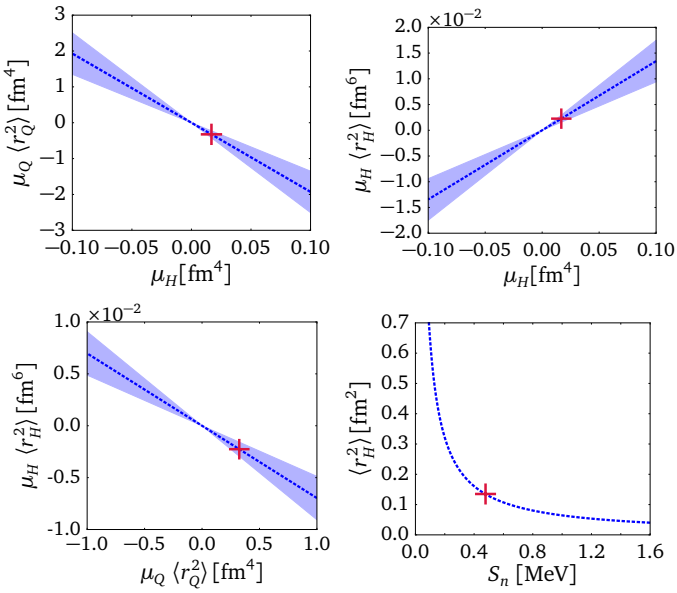

Figure 4.4.: Linear correlations between the hexadecapole moment and the quadrupole moment times quadrupole radius (top left), the hexadecapole moment and the hexadecapole moment times hexadecapole radius (top right) and between the quadrupole moment times quadrupole radius and hexadecapole moment times hexadecapole radius (bottom left). Bottom right: correlation between the neutron separation energy and the hexadecapole radius. The red cross denotes the numerical prediction for ^{15}C. The EFT uncertainties are given by the shaded bands.

states predicted by Halo EFT. Moreover, we combine our Halo EFT results with data and *ab initio* results from the IT-NCSM [29] to predict electric properties of ^{15}C. In a second step, the correlations obtained in Halo EFT are compared to the E2 correlation based on the rotational model by Bohr and Mottelson [31].

We note that the quantification of theory uncertainties is important in any application of EFT to actual systems. In our discussion below, we will estimate the theory uncertainties from the size of the expansion parameter R_{core}/R_{halo}. More sophisticated estimates can be obtained from Bayesian statistics [60]–[62], but such an analysis is beyond the scope of this work.

To make predictions, we use the experimental transition strength B(E2) $= 0.44(1)$ W.u. [28] for the $5/2^+ \to 1/2^+$ transition in ^{15}C to determine the denominator of the D-wave renormalization constant at LO, i.e. the combination $r_2 + \mathcal{P}_2\gamma_2^2$. Converting to physical units, we obtain the strength B(E2) $= 2.90(7)\ e^2$fm^4 for the transition $1/2^+ \to 5/2^+$. The experimental values of the binding momenta are $\gamma_0 = 0.235$ fm^{-1} and $\gamma_2 = 0.147$ fm^{-1} [28]. Moreover, Fernando et al. [42] argued that it is more appropriate to count $r_0 \sim R_{halo}$ for the specific case of ^{15}C and thus we keep this contribution at LO in our application to ^{15}C. The extracted value for $r_0 = 2.67$ fm [42] results from a fit to one-neutron capture data $^{14}\text{C}(n,\gamma)^{15}\text{C}$ [63]. With these data, we are able to determine the numerical value for $Z_d m_R^2 g_2^2 \sim 1/\left(r_2 + \mathcal{P}_2\gamma_2^2\right) = -181(4)$ fm^3.

Using our results from the previous Sections, we obtain the finite piece of the counterterms $\tilde{L}^{(d)}_{C01} + \frac{4}{3}\tilde{L}^{(d)}_{C02} = \langle r_E^2\rangle^{(d)}/1088(25)$ fm^{-1}, $\tilde{L}^{(d)}_{C02} = -\mu_Q^{(d)}/2418(55)$ fm^{-1}. For the hexadecapole moment and radius, we obtain the following predictions

$$\mu_H^{(d)} = 1.68(4)(50) \times 10^{-2}\ \text{fm}^4\,, \quad \text{and} \quad \langle r_H^2\rangle^{(d)} = 0.135(3)(40)\ \text{fm}^2\,, \tag{4.57}$$

where the first uncertainty is due to the experimental input and the second one is a theory uncertainty from higher order corrections of order $R_{core}/R_{halo} \approx 0.3$ (see below).

Comparing our findings with Ref. [41] we find, as a general rule, that the highest multipole form factor is always independent of additional parameters from short-range counterterms. Moreover, we can always find a smooth correlation between the highest radius and the neutron separation energy S_n

$$\langle r_H^2\rangle^{(d)} = \frac{9}{28}\frac{f^2}{m_R S_n^{(d)}}\ . \tag{4.58}$$

In the S- and P-wave case, we obtain

$$\langle r_Q^2\rangle^{(p)} = \frac{3}{10}\frac{f^2}{m_R S_n^{(p)}}\ , \tag{4.59}$$

$$\langle r_E^2\rangle^{(s)} = \frac{1}{4}\frac{f^2}{m_R S_n^{(s)}}\ . \tag{4.60}$$

For the D-wave, we can derive several linear correlations between different combinations of multipole moments and radii. This is illustrated in Fig. 4.4, where the red cross denotes the numerical prediction of the corresponding quantity for ^{15}C. Therefore, by

measuring one of these observables, we can immediately predict the correlated quantity. These correlations are universal and can be found in arbitrary one-neutron D-wave halo nuclei or similar weakly-bound systems.

With the numerical result for $Z_d m_R^2 g_2^2$, we can check if our power counting scenario, leading to the scaling $Z_d m_R^2 g_2^2 \sim R_{halo}^2 R_{core}$, can be confirmed or if the scenario of [14] yields better agreement. An approximation for the halo scale can be extracted from the neutron separation energy S_n, $R_{halo} \approx 1/\gamma_2 = 1/\sqrt{S_n 2m_R} = 6.81$ fm. We can approximate the core scale by looking at the energy of the first excitation of the ^{14}C nucleus $E_{ex} = 6.1$ MeV. Converting this energy into a length scale, we obtain $R_{core} \approx 1.91$ fm. By employing the experimental values for R_{halo} and R_{core}, we predict $Z_d m_R^2 g_2^2 \sim R_{halo}^2 R_{core} \approx 90$ fm^3. This value is only by a factor of 2 smaller than the one extracted from B(E2) and considering that this is an estimation grounded solely on the scaling within our power counting, our result is in reasonable agreement. The power counting of [14] does lead to the scaling $Z_d m_R^2 g_2^2 = 1/r_2 \sim R_{core}^3 \approx 7$ fm^3 which is around 26 times smaller than the extracted result. These numbers indicate that our power counting scenario is better suited for ^{15}C.

To obtain the correlation between the quadrupole transition from the $\frac{5}{2}^+$ to the $\frac{1}{2}^+$ state and the quadrupole moment of the $\frac{5}{2}^+$ state, we combine Eqs. (4.53) and (4.32) and apply a factor 2/6 to account for the different multiplicity of initial and final states. We obtain a linear dependence between B(E2) for the transition $\frac{5}{2}^+ \to \frac{1}{2}^+$ and the quadrupole moment

$$\text{B(E2)} = \frac{-1}{50\pi} \frac{Z_{\text{eff}}^2 e^2 \gamma_0}{(1 - r_0\gamma_0)} \left[\frac{3\gamma_0^2 + 9\gamma_0\gamma_2 + 8\gamma_2^2}{(\gamma_0 + \gamma_2)^3}\right]^2 \frac{\mu_Q^{(d)}}{\tilde{L}_{C02}^{(d)} - \frac{5}{4}\gamma_2 f^2} \,, \tag{4.61}$$

where $\tilde{L}_{C02}^{(d)}$ is treated as fit parameter and γ_0 and γ_2 are taken from experiment [28].

A similar correlation between the quadrupole transition and the quadrupole moment can be obtained from the rotational model by Bohr and Mottelson [31]

$$\begin{aligned} \text{B(E2}, J_i \to J_f) = \frac{5}{16\pi} \frac{\left((J+1)(2J+3)\right)^2}{\left(3K^2 - J(J+1)\right)^2} \\ \times \left(J_i K\ 20 | J_f K\right)^2 \left(\frac{Q^{0,t}}{Q^{0,s}}\right)^2 \mu_Q(J)^2 \,, \end{aligned} \tag{4.62}$$

where $K = 1/2$ denotes the projection of the total angular momentum on the symmetry axis of the intrinsically deformed nucleus and $Q^{0,t}/Q^{0,s}$ is the ratio between intrinsic

static (s) and transition (t) quadrupole moment in the rigid rotor model. The idea to employ this simple model is motivated by observations of Calci and Roth [30], who found a robust correlation between this pair of quadrupole observables in *ab initio* calculations for light nuclei. In the simple rigid rotor model the ratio $Q^{0,t}/Q^{0,s}$ is expected to be one. The results of Ref. [30] indicate that the correlation is robust as long as the ratio $Q^{0,t}/Q^{0,s}$ is treated as a fit parameter.

We use IT-NCSM data of ^{15}C, generated by different chiral EFT interactions and different model spaces, to check the quadratic and linear correlations and predict numerically the quadrupole moment of ^{15}C. This is demonstrated in Fig. 4.5. The varying symbols denote different NN+3N chiral EFT interactions which are similar to the ones used in Ref. [30]. We use the NN interaction developed by Entem and Machleidt (EM) [64] at N^{3}LO with a cutoff of 500 MeV/c for the nonlocal regulator function. This NN force is combined with the local 3N force at N^{2}LO using a cutoff of 400 or 500 MeV/c [65]. The second NN interaction by Epelbaum, Glöckle, Meißner (EGM) [66] at N^{2}LO uses a nonlocal regularization with a cutoff Λ_χ and an additional spectral function regularization with cutoff $\tilde{\Lambda}_\chi$. The EGM NN forces are combined with a consistent nonlocal 3N force at N^{2}LO used in several applications to neutron matter [67]–[69]. For reasons of convergence, the NN+3N potentials are softened by a similarity renormalization group evolution where all contributions up to the three-body level are included.

We note that these interactions are based on Weinberg's power counting [70] and their cutoff cannot be varied over a large range. However, chiral potentials based on Weinberg's power counting have been very successful phenomenologically in nuclear structure and are currently the only potentials available that are well tested for p-shell nuclei. In particular, N^{2}LO EGM interactions are still the only fully consistent set of two- and three-body interactions for which significant experience with structure calculations in the p-shell exists. Similarly, there is much experience with the EM interactions supplemented with (inconsistent) 3N forces. For this reason, we use these older interactions in our analysis. We believe that this is not a limiting factor of our analysis. After all, we are interested in universal properties which must emerge from any interaction that has the correct low-energy physics.

The different colors in Fig. 4.5 denote different N_{max} values. The EFT uncertainties for the linear correlation are given by the blue shaded bands. Since the IT-NCSM results are not fully converged and the results differ for different N_{max} values, the ordering of the ground and first excited state is exchanged for some data points. Leaving out the data sets with exchanged ordering does not significantly improve the fit. The plot on the left side employs the experimental values for the neutron separation energy as input for γ_0

and γ_2. For the plot on the right side, we use the excitation energy of the first excited state from the IT-NCSM to determine $\gamma_0^2 - \gamma_2^2$ and for γ_0 we use the experimental value.

We emphasize that in the *ab initio* calculations, both, the interactions (including short distance physics) and the model spaces are varied. If the *ab initio* calculations were (i) fully converged and (ii) all interactions and electric operators were unitarily equivalent at the A-body level, they would fall on a single point. However, neither (i) nor (ii) is the case here. So, naively, one would expect the calculations for B(E2) and μ_Q to fill the whole plane. Halo EFT and the rotational model, however, predict a one parameter correlation between B(E2) and μ_Q based on certain assumptions. If these assumptions, such as shallow binding and a corresponding separation of scales in the case of Halo EFT, are satisfied in the *ab initio* calculations, they should also show the correlation even if they are not converged and/or have different short distance physics. A similar behavior is observed in the case of the Phillips and Tjon line correlations in light nuclei which are also satisfied by "unphysical" calculations (See, e.g., Ref. [71] for an explicit example).

An additional complication here is the appearance of the two-body coupling $L_{C02}^{(d)}$ in Eq. (4.27) which could vary for the different *ab initio* data sets. In our analysis of the *ab initio* data, we explicitly assume that $L_{C02}^{(d)}$ varies only slowly and can be approximated by a constant for the *ab initio* data considered.[2] Under this assumption, it becomes possible to decide between the type of correlation using the *ab initio* data for ^{15}C.

From the left plot, we obtain for the quadratic fit $\mu_Q^{(d)} \approx -3.98(5)$ fm^2 and for the linear fit $\mu_Q^{(d)} \approx -5.46(12)(1.64)$ fm^2, where the uncertainties from B(E2) are given in parenthesis. The second uncertainty for the linear fit is from higher orders in the EFT. From the fits, we cannot decide which scenario describes the IT-NCSM data more appropriately since both lead to similar reduced χ^2 values of $\chi^2_{red} = 110$ for the quadratic fit and $\chi^2_{red} = 123$ for the linear fit. Please note that the absolute χ^2_{red} values have no significance since the theoretical errors of the *ab initio* results were not included in the fit, and only a relative comparison makes sense. The ratio $Q^{0,t}/Q^{0,s}$ should be equal to 1 for an ideal rigid rotor. Since the quadratic fit yields a ratio of $Q^{0,t}/Q^{0,s} \approx 0.5$, we assume that ^{15}C is not a good example of a rigid rotor. Perhaps for larger N_{max} values,

[2] A similar assumption is made in the analysis of three-body recombination rates for ultracold atoms near a Feshbach resonance to observe the Efimov effect. There the scattering length varies strongly with the magnetic field B while the three-body parameter is assumed to stay approximately constant [72]. Since the two parameters are independent it would be very unnatural if both had a resonance at the same value of B.

and thus better converged results, the matching between fit curves and data points would improve.

In the linear case, the slope of the fit depends also on the neutron separation energies of both states, which differ for each data point from the IT-NCSM. From the excitation energy obtained in the IT-NCSM calculation, we only know the difference between the neutron separation energies of the ground and excited state. Thus, one experimental input is still required to fix γ_0 and γ_2 from the IT-NCSM data, since we did not perform explicit calculations for ^{14}C. In the right plot of Fig. 4.5, we determine $\gamma_0^2 - \gamma_2^2$ from IT-NCSM data and take γ_0 from experiment. We deem this analysis to be more consistent than the previous one. The reduced χ^2 value for the linear fit then slightly improves to $\chi^2_{red} = 80$ compared to the fit using experimental values only. This leads to $\mu_Q^{(d)} \approx -4.21(10)(1.26)\ \mathrm{fm}^2$, which is closer to the value from the quadratic fit. The deviations of the data points from the linear fit might decrease further if consistent values for both neutron separation energies were extracted from the IT-NCSM. This NLO correlation is expected to hold up to corrections of order $R_{core}/R_{halo} \approx 0.3$ given by the blue shaded band. Taking this EFT uncertainty into account, the *ab initio* data satisfy the correlation very well.

With the extracted results of $\mu_Q^{(d)}$ and using the Halo EFT correlations, we can predict the quadrupole radius to be $\langle r_Q^2 \rangle^{(d)} = 5.93(13)(1.78) \times 10^{-2}$ fm^2 from the left linear fit and $\langle r_Q^2 \rangle^{(d)} = 7.70(17)(2.31) \times 10^{-2}$ fm^2 from the right linear fit in Fig. 4.5.

Finally, we note that the NCSM calculations for small N_{max} are not converged in the IR. However, it can be clearly seen in Fig. 4.5 that our conclusions are unchanged if the smallest $N_{max} = 2, 4, 6$ are omitted. In fact, Calci et al. [30] showed explicitly that the universal correlation between the B(E2: $0^+ \to 2^+$) and the quadrupole moment of the 2^+ state in ^{12}C is extremely well satisfied even for the smallest N_{max}.

4.3. Conclusion

We have extended the Halo EFT approach for electric observables to shallow D-wave bound states. Additionally, a basic framework for the extension of our Halo EFT to higher partial waves has been outlined. We have developed a power counting scheme for arbitrary l-th partial wave shallow bound states that differs from the scenario of [14] for $l > 1$. This power counting was applied to ^{17}C in Ref. [27] where also some

magnetic observables were considered. For higher partial waves the number of fine-tuned parameters increases. Based on the assumption that a larger number of fine tunings is less natural, this suggests that shallow bound states in higher partial waves are less likely than in lower ones, which is also observed experimentally.

Using this scheme, we have computed the B(E2) strength at LO and found that no additional counterterm is required at this order. We have also calculated the electric quadrupole as well as hexadecapole form factors at NLO and found a smooth, universal correlation between the quadrupole radius and the hexadecapole moment. We find that for the D-wave, the local gauge invariant operators become more important than in lower partial waves and counterterms are required for the form factors already at NLO. This continues the trend, observed in [41], that the counterterms enter in lower orders at larger l. The emergence of counterterms in low orders limits the predictive power of Halo EFT for D-waves. However, this limitation can be overcome by considering universal correlations between observables as discussed below.

We emphasize that, up to this point, all our results are universal and not specific for ^{15}C. Considering now ^{15}C as an example, the lack of data for the first excited $\frac{5}{2}^+$ state makes numerical predictions difficult. Using our result for the B(E2) and by comparing it to the measured B(E2) data, we have been able to make predictions for the hexadecapole moment $\mu_H^{(d)} = 1.68(4)(50) \times 10^{-2}$ fm^4 and radius $\langle r_H^2 \rangle^{(d)} = 0.135(3)(40)$ fm^2. We cannot directly predict values for the charge radius and quadrupole moment and radius at NLO since the expressions (4.50), (4.53) and (4.55) contain unknown counterterms. Nevertheless, we have determined a value for the quadrupole moment, $\mu_Q^{(d)} \approx -4.21(10)(1.26)\,\mathrm{fm}^2$, by exploiting the linear correlation between the reduced E2 transition strength B(E2) and the quadrupole moment in our Halo EFT and fitting the unknown counterterm to *ab initio* results from the IT-NCSM. For consistency reasons, we prefer the result from the right plot of Fig. 4.5 using the excitation energy from IT-NCSM calculation. With this result for the quadrupole moment, we have also predicted the quadrupole radius for ^{15}C, $\langle r_Q^2 \rangle^{(d)} \approx 7.70(17)(2.31) \times 10^{-2}\ \mathrm{fm}^2$, using universal correlations from Halo EFT. These correlations are not obvious in *ab initio* approaches, since the separation of scales is not explicit in the parameters of the theory. This demonstrates the complementary character of Halo EFT towards *ab initio* methods. In principle, the universal correlations allow to extract information even from unconverged *ab initio* calculations since the correlations are universal. We have compared the linear Halo EFT correlation to the quadratic correlation based on the simple rotational model by Bohr and Mottelson. The value for the quadrupole moment, $\mu_Q^{(d)} \approx -3.98(5)\ \mathrm{fm}^2$, obtained from the quadratic correlation deviates from the linear result by 5% – 30% depending

on the input used for $\gamma_0^2 - \gamma_2^2$.

While there is a clear correlation in the *ab initio* data, there are also some outliers. In the case of the linear Halo EFT correlation, this could be due to the use of the experimental value of the ground state neutron separation energy γ_0, which is presumably inconsistent with some of the *ab initio* data sets. Since the Halo EFT correlation depends on the exact neutron separation energy of the two states, consistent values should be used. However, within the EFT uncertainty the predicted correlation is well satisfied. Better converged data sets and the future determination of the neutron separation energy directly from the IT-NCSM would help to clarify the situation. This proves the usefulness of our Halo EFT approach even for D-wave bound states, but also demonstrates the limiting factors for the extension to higher partial waves.

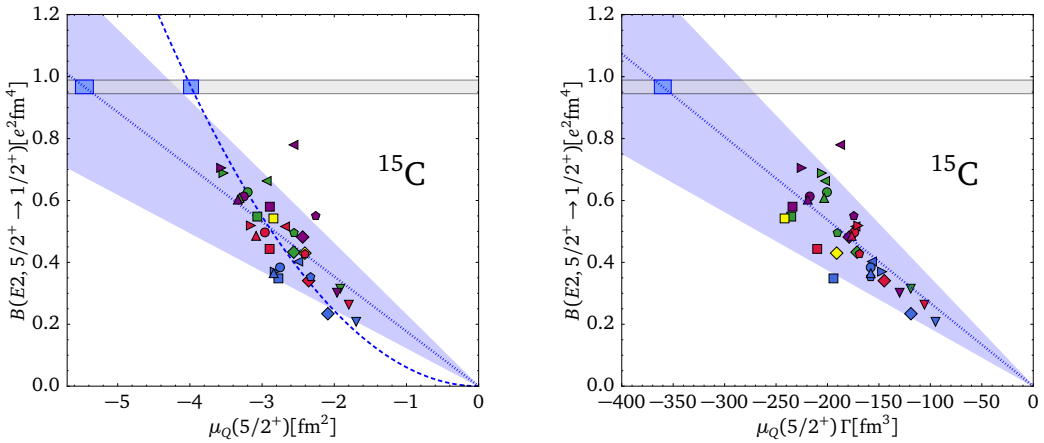

Figure 4.5.: Correlation between B(E2) and the quadrupole moment μ_Q. The IT-NCSM data is obtained with different NN+3N chiral EFT interactions: EM with cutoffs $\{400, 400, 500\}$ MeV/c (square, diamond, triangle down), and EGM with cutoffs $(\Lambda_\chi/\tilde{\Lambda}_\chi) = \{(450/500), (600/500), (550/600), (450/700), (600/700)\}$ MeV/c (triangle left, pentagon, circle, triangle right, and triangle up) with oscillator frequency $\hbar\Omega = 16$ MeV for all IT-NCSM calculations except for the diamond and triangle down data where $\hbar\Omega = 20$ MeV. Different colors denote different $N_{\max} = 2$ (blue), 4 (red), 6 (green), 8 (violet), and 10 (yellow) values. Left panel: Rigid rotor model with quadratic fit of $Q^{0,t}/Q^{0,s}$ ratio (dashed line, $\chi^2_{red} = 110$) and linear Halo EFT fit of $\tilde{L}^{(d)}_{C02}$ with fixed γ_2 from experiment (dotted line, $\chi^2_{red} = 123$). Right panel: Linear Halo EFT fit with $\gamma_0^2 - \gamma_2^2$ from IT-NCSM calculation and rescaled μ_Q/Γ (dotted line, $\chi^2_{red} = 80$), where $\Gamma = \gamma_0(3\gamma_0^2+9\gamma_0\gamma_2+8\gamma_2^2)^2/(1-r_0\gamma_0)/(\gamma_0+\gamma_2)^6$ divides out dependence on γ_0 and γ_2. The gray shaded area indicates the uncertainty band of the experimental B(E2) [28]. The blue box within the gray shaded area corresponds to the prediction for μ_Q. The EFT uncertainties are given by the blue shaded bands.

5. Spherical Formalism for EM Observables of Halo Nuclei

In this Chapter, we present an alternative approach to describe higher partial wave halo nuclei. Instead of using standard Cartesian coordinates, we introduce a spherical basis that is ideally suited for the description of halo nuclei beyond the S-wave. It uses the correct number of degrees of freedom by construction and therefore leads to more compact and simplified expressions. We present our findings for the case of the P-wave halo nucleus ^{31}Ne.

In order to describe ^{31}Ne as a shallow P-wave bound state between the ^{30}Ne core and the valence neutron, we use a Lagrangian including a bosonic field c for the core and a spinor field n_α for the neutron with $\alpha \in \{-1/2, 1/2\}$. Moreover, a dimer spinor field π_β is introduced which encodes the physics of ^{31}Ne with $\beta \in \{-3/2, -1/2, 1/2, 3/2\}$. A resonant P-wave interaction then enables transitions of the core and neutron into this dimer field and vice versa. The corresponding Lagrangian is given by

$$\begin{aligned}\mathcal{L} = {} & c^\dagger \left[i\partial_0 + \frac{\nabla^2}{2m_c} \right] c + n_\alpha^\dagger \left[i\partial_0 + \frac{\nabla^2}{2m_n} \right] n_\alpha + \pi_\beta^\dagger \left[\eta \left(i\partial_0 + \frac{\nabla^2}{2M_{nc}} \right) + \Delta \right] \pi_\beta \\ & - g \left[\left(c \overleftrightarrow{\nabla}_i n_\alpha \right) \pi_\beta^\dagger \, C^{\frac{3}{2}\beta}_{(1i)(\frac{1}{2}\alpha)} + \text{H.c.} \right],\end{aligned} \tag{5.1}$$

with $M_{nc} \equiv m_n + m_c$ denoting the mass of the two-particle state while $\eta \equiv \pm 1$ is a sign which will be fixed from matching. Moreover, $\overleftrightarrow{\boldsymbol{\nabla}} \equiv m_R \left[{m_c}^{-1} \overleftarrow{\boldsymbol{\nabla}} - {m_n}^{-1} \overrightarrow{\boldsymbol{\nabla}} \right]$ is the Galilean-invariant derivative where m_R denotes the core-neutron reduced mass. The coefficient $C^{\frac{3}{2}\beta}_{(1i)(\frac{1}{2}\alpha)}$ is a Clebsch-Gordan coefficient coupling the neutron spin and the core-neutron relative angular momentum to the total spin of the dimer field. Note that the index i of the derivative operator is a spherical index denoting the projection of the P-wave interaction whereas α and β are spinor indices denoting the projections of their corresponding spins.

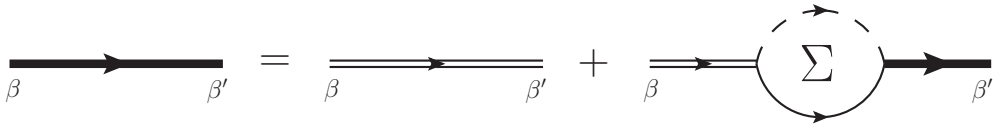

Figure 5.1.: Diagrammatic representation of the Dyson equation for the full dimer propagator representing the ^{30}Ne-n P-wave bound state. The thick line denotes the full dimer propagator, while the double solid line denotes the bare propagator. The single solid line represents the neutron field, whereas the dashed line represents the core field.

5.1. Full Dimer Propagator

As in Chapter 4, we work in the dimer formalism and use the power divergence subtraction scheme from Refs. [25] and [26] with renormalization scale μ. The corresponding dimer self-energy is diagonal in the spin indices of the incoming and outgoing dimer fields and reads

$$-i\Sigma_{\beta'\beta}(p_0,p) = -i\Sigma(p_0,p)\delta_{\beta'\beta}, \tag{5.2}$$

with the scalar dimer self-energy given by

$$-i\Sigma(p_0,p) = \frac{im_R g^2 2m_R\left(p_0-\frac{p^2}{2M_{nc}}\right)}{6\pi}\left(\frac{3}{2}\mu - \sqrt{-2m_R\left(p_0-\frac{p^2}{2M_{nc}}\right)-i\epsilon}\right), \tag{5.3}$$

where $p=|\boldsymbol{p}|$.

In order to determine the full dimer propagator, we dress the bare propagator given by

$$iD^0(p_0,p) = \frac{i}{\eta\left(p_0-\frac{p^2}{2M_{nc}}\right)+\Delta+i\epsilon} \tag{5.4}$$

with a geometric series of dimer self-energies. We end up with the Dyson equation which is diagramatically depicted in Fig. 5.1. Since the dimer self-energy and the bare dimer propagator are diagonal in the spin indices, also the full dimer propagator is diagonal and reads

$$iD_{\beta'\beta}(p_0,p) = iD(p_0,p)\delta_{\beta'\beta}, \tag{5.5}$$

where the scalar full propagator is given by

$$\begin{aligned} iD(p_0,p) &= \frac{iD^0(p_0,p)}{1-\Sigma(p_0,p)D^0(p_0,p)} \\ &= \frac{i}{\eta\left(p_0-\frac{p^2}{2M_{nc}}\right)+\Delta-\Sigma(p_0,p)+i\epsilon}. \end{aligned} \tag{5.6}$$

The full dimer propagator has to have a pole at the energy $p_0 = \frac{p^2}{2M_{nc}} - B$ with $B = \gamma^2/(2m_R)$ denoting the binding energy of the two-particle state given by the neutron separation energy of ^{31}Ne, whereas $\gamma > 0$ is the corresponding binding momentum. In order to calculate S-matrix elements by applying bare perturbation theory, we need to determine the wave function renormalization constant defined by

$$Z^{-1} = \left(\frac{\partial}{\partial p_0}\frac{1}{D(p_0,p)}\right)\Bigg|_{p_0=\frac{p^2}{2M_{nc}}-B}, \tag{5.7}$$

yielding the relation

$$Z = -\frac{6\pi}{m_R^2 g^2}\frac{1}{3\gamma+r_1}. \tag{5.8}$$

5.2. Scattering Amplitude

The on-shell neutron-core scattering amplitude for a P-wave with $J = 3/2$ in the center-of-mass frame reads

$$T_{\alpha'\alpha}(\boldsymbol{p}',\boldsymbol{p}) = \frac{6\pi}{m_R}\frac{\frac{2}{3}\boldsymbol{p}'\boldsymbol{p}\delta_{\alpha'\alpha}+\frac{i}{3}\left(\sum_l \boldsymbol{\sigma}_l\,(\boldsymbol{p}'\times\boldsymbol{p})_l\right)_{\alpha'\alpha}}{\left(\frac{6\pi\Delta}{m_R g^2}+\frac{3\pi\eta}{m_R^2 g^2}p^2+\frac{3}{2}\mu p^2+ip^3\right)}, \tag{5.9}$$

where the σ_l are the spherical Pauli matrices while $(\boldsymbol{p}'\times\boldsymbol{p})_l$ is the l-th component of the vector product in spherical basis representation. It is given by attaching external core and neutron propagators to the dressed dimer propagator as depicted in Fig. 5.2.

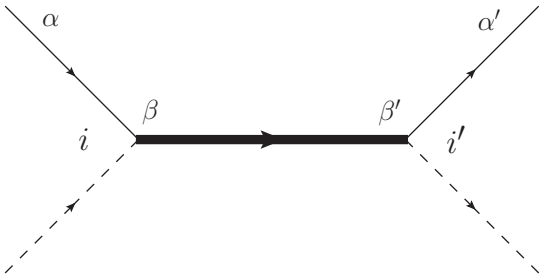

Figure 5.2.: Neutron-core scattering amplitude, finally only depending on the initial and final projections of the neutron spins given by α and α', respectively. This follows from the implied sum over the possible projections of all other indices.

5.2.1. Renormalization

Using renormalized instead of bare constants, the amplitude reads

$$T_{\alpha'\alpha}(\boldsymbol{p}',\boldsymbol{p}) = \frac{6\pi}{m_R} \frac{\frac{2}{3}\boldsymbol{p}'\boldsymbol{p}\delta_{\alpha'\alpha} + \frac{i}{3}\left(\sum_l \boldsymbol{\sigma}_l \left(\boldsymbol{p}'\times\boldsymbol{p}\right)_l\right)_{\alpha'\alpha}}{\left(\frac{6\pi\Delta^{\mathrm{R}}}{m_R\left(g^{\mathrm{R}}\right)^2} + \frac{3\pi\eta}{m_R^2\left(g^{\mathrm{R}}\right)^2}p^2 + ip^3\right)}, \tag{5.10}$$

where the renormalized coupling constants satisfy the following relations in order to ensure a renormalization-scale-independent amplitude

$$\frac{3\pi\eta}{m_R^2 g^2} + \frac{3}{2}\mu = \frac{3\pi\eta}{m_R^2\left(g^{\mathrm{R}}\right)^2}, \tag{5.11}$$

$$\frac{\Delta}{g^2} = \frac{\Delta^{\mathrm{R}}}{\left(g^{\mathrm{R}}\right)^2}. \tag{5.12}$$

5.2.2. Matching

Comparing this amplitude to the amplitude using effective range expansion parameters given by

$$T_{\alpha'\alpha}(\boldsymbol{p}',\boldsymbol{p}) = \frac{6\pi}{m_R} \frac{\frac{2}{3}\boldsymbol{p}'\boldsymbol{p}\delta_{\alpha'\alpha} + \frac{i}{3}\left(\sum_l \boldsymbol{\sigma}_l \left(\boldsymbol{p}'\times\boldsymbol{p}\right)_l\right)_{\alpha'\alpha}}{\left(\frac{1}{a_1} - \frac{1}{2}r_1 p^2 + ip^3\right)}, \tag{5.13}$$

leads to the following matching conditions

$$a_1 = \frac{m_R \left(g^{\mathrm{R}}\right)^2}{6\pi\Delta^{\mathrm{R}}}, \tag{5.14}$$

$$r_1 = -\frac{6\pi\eta}{m_R^2 \left(g^{\mathrm{R}}\right)^2}. \tag{5.15}$$

Since for causal scattering the parameter r_1 has to be negative, the sign η is determined to be $\eta = +1$ according to Eq. (5.15).

5.3. Power Counting

In the following, we assume only one combination of coupling constants to be fine-tuned, namely Δ/g^2. This is sufficient in order to produce a shallow P-wave bound state. With this choice, the scattering volume a_1 is enhanced by

$$a_1 \sim \frac{1}{M_{\mathrm{lo}}^2 M_{\mathrm{hi}}}, \tag{5.16}$$

whereas the P-wave effective momentum r_1 scales like

$$r_1 \sim M_{\mathrm{hi}}, \tag{5.17}$$

where M_{lo} and M_{hi} denote the typical low- and high-momentum scales of the system, respectively. The low-momentum scale is given by the binding momentum of the shallow P-wave bound state. In the case of ^{31}Ne with a binding energy of $B = 150$ keV [73], this yields

$$M_{\mathrm{lo}} \approx \gamma = \sqrt{2 m_R B} = 16.51 \text{ MeV}. \tag{5.18}$$

The high-momentum scale can be approximated by the breakdown scale of the theory. Therefore, we can estimate M_{hi} by the associated momentum scale of the core excitation energy $E_{\mathrm{ex}} = 792$ keV [74]. At this momentum scale, our theory is no longer valid because the core can no longer be treated as a fundamental degree of freedom as it is done in our theory. The corresponding value is given by

$$M_{\mathrm{hi}} \approx \sqrt{2 m_R E_{\mathrm{ex}}} = 37.95 \text{ MeV}. \tag{5.19}$$

Within this power counting scheme, the leading order wave function renormalization constant reads

$$Z^{\mathrm{LO}} = -\frac{6\pi}{m_R^2 g^2 r_1}. \tag{5.20}$$

The quantity $g^2 Z^{\mathrm{LO}}$ is proportional to the absolute value squared of the EFT wave function, namely with a positive proportionality constant. Thus, this quantity itself should be positive to ensure a normalizable state. Since r_1 is negative, the absolute value squared of the wave function at leading order is indeed positive. At NLO, the wave function renormalization is given by

$$Z^{\mathrm{NLO}} = -\frac{6\pi}{m_R^2 g^2}\frac{1}{3\gamma + r_1}, \tag{5.21}$$

and therefore only if $|r_1| > 3\gamma$ holds, we end up with a normalizable state. In other words, only if the high- and low-momentum scales are well enough separated, we achieve a normalizable state. Due to our results in Eqs. (5.18) and (5.19), this is not the case. Consequently, without including other degrees of freedom in our theory, we are limited to leading order calculations.

For a shallow P-wave state, we have at least two effective range expansion parameters, a_1 and r_1, which have to be fixed by observables. Until now, we only know the neutron separation energy of ^{31}Ne which is not enough in order to fix both effective range expansion parameters. Therefore, we will estimate the P-wave effective momentum r_1 in an interval around the breakdown scale, according to Eq. (5.17) and use the neutron separation energy to determine the scattering volume a_1. This enables us to calculate estimations of other observables accessible in our theory, such as the electromagnetic current and the corresponding multipole moments as well as the associated radii.

5.4. Electromagnetic Current

In this Section, we show how we include electromagnetic interactions to our theory. Moreover, we derive the corresponding form factors using spherical coordinates. Thereby, we not only present our results for the relevant form factors in ^{31}Ne but also for form factors of arbitrary high multipolarity L.

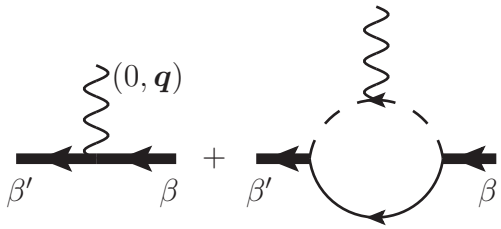

Figure 5.3.: Diagrams contributing to the irreducible vertex for an A_0 photon coupling to the ^{30}Ne-n P-wave bound state at LO.

5.4.1. Electromagnetic Interactions

In a first step, electromagnetic interactions are included via minimal substitution

$$\partial_\mu \to D_\mu = \partial_\mu + ie\hat{q}A_\mu, \tag{5.22}$$

meaning that the usual derivative ∂_μ in the Lagrangian in Eq. (5.1) is replaced by the covariant derivative D_μ containing the charge operator $\hat{q}$, the elementary charge $e > 0$ and the photon field $A^\mu = (A_0, \boldsymbol{A})$. In addition, all possible gauge-invariant operators involving the electric field $\boldsymbol{E}$ and also the magnetic field $\boldsymbol{B}$ have to be considered within our power counting scheme. It turns out that only gauge-invariant operators proportional to the magnetic field $\boldsymbol{B}$ are contributing at LO whereas operators involving the electric field $\boldsymbol{E}$ contribute at higher orders and therefore are not considered in our LO calculations.

5.4.2. Scalar Current

Firstly, we calculate the matrix element of the zeroth component of the electromagnetic current of ^{31}Ne. Therefore, we consider the amplitude with an irreducible vertex for an A_0 photon with four momentum $(0, \boldsymbol{q})$ coupling to the ^{30}Ne-n P-wave bound state whereby $\boldsymbol{q} = \boldsymbol{p}' - \boldsymbol{p}$ and $q = |\boldsymbol{q}|$. The initial and final states are characterized by their momenta and projections of the spin, denoted by $|\pi_\beta(\boldsymbol{p})\rangle$ and $|\pi_{\beta'}(\boldsymbol{p}')\rangle$, respectively. The LO contributions to this amplitude are depicted in Fig. 5.3. Since ^{31}Ne has a total spin of $3/2$, there are four possible projections for each the initial and final state. Hence, the tensors connecting initial and final state projections are 4×4 matrices.

The scalar electromagnetic transition amplitude can be written as

$$\begin{aligned}\langle \pi_{\beta'}(\boldsymbol{p}')|\, J_0\, |\pi_\beta(\boldsymbol{p})\rangle = &- iq_c e G_{\mathrm{E0}}(q)\sqrt{\frac{4\pi}{1}} q^0 Y_{00}(\boldsymbol{e_q}) \left[\tilde{T}^{00}_{3/2}\right]_{\beta'\beta} \\ &- i\mu_Q G_{\mathrm{E2}}(q)\frac{1}{2}\sqrt{\frac{4\pi}{5}} q^2 \sum_M Y_{2M}(\boldsymbol{e_q}) \left[\tilde{T}^{2M}_{3/2}\right]_{\beta'\beta},\end{aligned} \tag{5.23}$$

where $\boldsymbol{e_q}$ is the unit vector of $\boldsymbol{q}$, q_c is the charge of the core in terms of the elementary charge e and μ_Q is the quadrupole moment. Moreover, the electric monopole and quadrupole form factors are denoted by $G_{\mathrm{E0}}(q)$ and $G_{\mathrm{E2}}(q)$, respectively. The tensors $\tilde{T}^{00}_{3/2}$ and $\tilde{T}^{2M}_{3/2}$ are normalized 4×4 polarization matrices and in general normalized $(2J+1)\times(2J+1)$ matrices given by

$$\left[\tilde{T}^{LM}_J\right]_{\beta'\beta} = \frac{C^{J\beta'}_{(J\beta)(LM)}}{C^{JJ}_{(JJ)(L0)}}. \tag{5.24}$$

They are normalized such that they have a coefficient of 1 for maximal projections. Consequently, the multipole moments are defined for maximal projections as it is usually done by convention. The occurring subscript J is the spin of the considered two-particle bound state, while L stands for the angular momentum of the photon. The possible contributions for L result from overlapping the two P-wave spherical harmonics appearing in the right diagram of Fig. 5.3. Furthermore, M denotes the projection of the angular momentum L. The irreducible representation of this implicit coupling mentioned above is given by

$$3 \otimes 3 = 1 \oplus 3 \oplus 5, \tag{5.25}$$

which means that the possible angular momenta are $L \in \{0,1,2\}$. Due to parity conservation, only even numbers of L contribute so that we are left with $L \in \{0,2\}$. Hence, as we can read off Eq. (5.23), there is an electric monopole and quadrupole form factor appearing with their corresponding multipole moments but no dipole form factor. Note that if we would were to consider a spin $1/2$ dimer, there would be no quadrupole contribution in Eq. (5.23) because of the properties of the Clebsch-Gordan coefficients. The LO results for the electric form factors read

$$G_{\mathrm{E0}}(q) = \left[1 - \frac{\gamma}{r_1} + \frac{y^2q^2+2\gamma^2}{yqr_1}\arctan\left(\frac{yq}{2\gamma}\right)\right], \tag{5.26}$$

$$G_{\mathrm{E2}}(q) = -\frac{q_c e}{\mu_Q 2 r_1 y q^3}\left[2\gamma yq + \left(y^2q^2 - 4\gamma^2\right)\arctan\left(\frac{yq}{2\gamma}\right)\right], \tag{5.27}$$

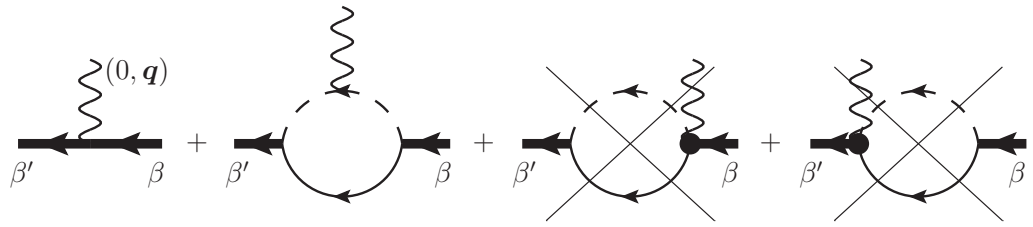

Figure 5.4.: Diagrams contributing to the irreducible vertex for an A_k photon coupling to the ^{30}Ne-n P-wave bound state at LO. The diagrams crossed out are indeed possible contributing diagrams but straightforward calculations reveal that they are vanishing and therefore can be left out.

with $y = m_n/M_{nc} = m_R/m_c$. These form factors should be normalized in the limit of vanishing photon momentum. Therefore, we demand

$$\lim_{q\to 0} G_{\mathrm{E0}}(q) \equiv 1, \tag{5.28}$$

$$\lim_{q\to 0} G_{\mathrm{E2}}(q) \equiv 1. \tag{5.29}$$

Since gauge-invariance ensures charge conservation, the limit in Eq. (5.28) should be naturally fulfilled and hence serves as a consistency check whereas the limit in Eq. (5.29) determines the quadrupole moment and yields

$$\mu_Q = -\frac{y^2 q_c e}{3\gamma r_1}. \tag{5.30}$$

Inserting this quadrupole moment in Eq. (5.27) gives the normalized quadrupole form factor

$$G_{\mathrm{E2}}(q) = \frac{3\gamma}{2y^3q^3}\left[2\gamma yq + \left(y^2q^2 - 4\gamma^2\right)\arctan\left(\frac{yq}{2\gamma}\right)\right]. \tag{5.31}$$

5.4.3. Vector Current

Secondly, we investigate the vector electromagnetic current of ^{31}Ne. For this reason, we consider the amplitude with an irreducible vertex for an A_k photon with four momentum $(0, \boldsymbol{q})$ coupling to the ^{30}Ne-n P-wave bound state. The corresponding diagrams are

depicted in Fig. 5.4. Furthermore, we have to take into account the magnetic moment coupling to the spins of the corresponding fields. Both, the magnetic moment coupling to the neutron spin and the one to the dimer spin already contribute at LO. The diagrams can be found in Fig. 5.5 and the corresponding magnetic interaction vertices are given by

$$\mathcal{O}^n_{\mathrm{M}} = \kappa_n \mu_N \, n^\dagger_{\alpha'} \left(\sum_l 2 \boldsymbol{S}^{\frac{1}{2}}_l \boldsymbol{B}_l \right)_{\alpha'\alpha} n_\alpha, \tag{5.32}$$

$$\mathcal{O}^\pi_{\mathrm{M}} = L_{\mathrm{M}} \mu_N \, \pi^\dagger_{\beta'} \left(\sum_l \frac{2}{3} \boldsymbol{S}^{\frac{3}{2}}_l \boldsymbol{B}_l \right)_{\beta'\beta} \pi_\beta, \tag{5.33}$$

where κ_n denotes the anomalous magnetic moment of the neutron, L_{M} is a counterterm and μ_N is the nuclear magneton. Furthermore, $\boldsymbol{B}_l = (\boldsymbol{\nabla} \times \boldsymbol{A})_l$ is the l-th component of the magnetic photon field in spherical coordinates. Moreover, the l-th spin matrix depending on the spin J of the considered field is denoted by S^J_l. The general expression in spherical basis representation is given by

$$\left[S^J_l \right]_{\sigma'\sigma} = \sqrt{J(J+1)} C^{J\sigma'}_{(J\sigma)(1l)}. \tag{5.34}$$

In our case, $J = 1/2$ for the neutron while $J = 3/2$ for the dimer field. The magnetic operators in Eqs. (5.32) and (5.33) are introduced in the form

$$\sum_l \frac{1}{J} \boldsymbol{S}^J_l \boldsymbol{B}_l. \tag{5.35}$$

Therefore, the matrix element for maximal projections is always given by B_0.

The vector electromagnetic transition amplitude can be written as

$$\begin{aligned} \langle \pi_{\beta'}(\boldsymbol{p}') | \, J_k \, | \pi_\beta(\boldsymbol{p}) \rangle = \Bigg(& i q_c e G_{\mathrm{E0}}(q) \sqrt{\frac{4\pi}{1}} q^0 Y_{00}(\boldsymbol{e_q}) \left[\tilde{T}^{00}_{3/2} \right]_{\beta'\beta} \\ & + i \mu_Q G_{\mathrm{E2}}(q) \frac{1}{2} \sqrt{\frac{4\pi}{5}} q^2 \sum_M Y_{2M}(\boldsymbol{e_q}) \left[\tilde{T}^{2M}_{3/2} \right]_{\beta'\beta} \Bigg) \frac{(\boldsymbol{p}' + \boldsymbol{p})^*_k}{2M_{nc}} \\ & + i \mu_D G_{\mathrm{M1}}(q) \sqrt{\frac{4\pi}{3}} q^1 \sum_M \sqrt{2} C^{1(M+k)}_{(1k)(1M)} Y^*_{1(M+k)}(\boldsymbol{e_q}) \left[\tilde{T}^{1M}_{3/2} \right]^\dagger_{\beta'\beta} \\ & + i \mu_O G_{\mathrm{M3}}(q) \frac{1}{2} \sqrt{\frac{4\pi}{7}} q^3 \sum_M \sqrt{2} C^{3(M+k)}_{(1k)(3M)} Y^*_{3(M+k)}(\boldsymbol{e_q}) \left[\tilde{T}^{3M}_{3/2} \right]^\dagger_{\beta'\beta}, \end{aligned} \tag{5.36}$$

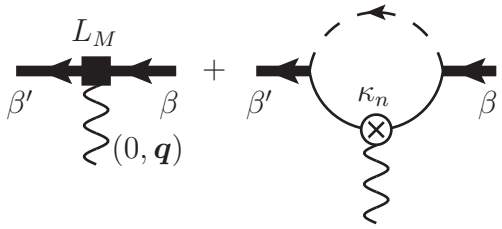

Figure 5.5.: Diagrams contributing to the irreducible vertex for a B_k photon coupling to the ^{30}Ne-n P-wave bound state at LO. On the one hand, the magnetic photon can couple to the neutron spin via the anomalous magnetic moment κ_n and on the other hand it can directly couple to the dimer spin via the counterterm L_{M}.

where μ_D denotes the magnetic dipole moment, μ_O is the magnetic octupole moment, whereas G_{M1} and G_{M3} are their corresponding magnetic form factors, respectively. Obviously, the physics of the vector electromagnetic current is richer. Not only the electric monopole and quadrupole form factor appear in Eq. (5.36) but also the magnetic contributions. In our case, or rather for a spin $3/2$ particle, in addition to the magnetic dipole moment there is also a magnetic octupole moment, similarly to the additional electric quadrupole moment. Due to the integral over the two P-wave spherical harmonics and over the spherical harmonic from the vector photon in the second diagram of Fig. 5.4, we now have an implicit coupling of three angular momenta. The corresponding irreducible representation is given by

$$3 \otimes 3 \otimes 3 = 1 \oplus 3 \oplus 5 \oplus 7, \tag{5.37}$$

meaning that the possible angular momenta are $L \in \{0, 1, 2, 3\}$. However, parity conservation restricts the possible values to $L \in \{1, 3\}$. The contributions of $L = 1$ and $L = 3$ manifest in Eq. (5.36) through terms proportional to $Y_{1(M+k)}$ and $Y_{3(M+k)}$, respectively. In contrast, the electric contributions to the vector current are apparent through the term proportional to $(\boldsymbol{p}' + \boldsymbol{p})_k$.

A closer look at the form factors in Eq. (5.36) suggests more generalized formulas for arbitrary high multipole electric and magnetic form factors. In particular, the electric form factors appearing in the vector current with an even multipolarity L for a particle

with total spin J might be written as

$$\left(i\mu_{\mathrm{EL}}G_{\mathrm{EL}}(q)\frac{1}{a(L)}\sqrt{\frac{4\pi}{2L+1}}q^L\sum_M Y_{LM}(\boldsymbol{e_q})\left[\tilde{T}_J^{LM}\right]_{\beta'\beta}\right)\frac{(\boldsymbol{p'}+\boldsymbol{p})_k^*}{2M_{nc}}, \tag{5.38}$$

where $a(L)$ denotes the leading denominators of the Legendre polynomials given by

$$a(L)=2^{\left(\mathrm{Floor}\left[\frac{L}{2}\right]+\mathrm{Floor}\left[\frac{L}{4}\right]+\mathrm{Floor}\left[\frac{L}{8}\right]+\mathrm{Floor}\left[\frac{L}{16}\right]+\ldots\right)}, \tag{5.39}$$

while μ_{EL} stands for the electric multipole moment.

The magnetic form factors appearing in the vector current with an odd multipolarity L for a particle with total spin J might be written as

$$i\mu_{\mathrm{ML}}G_{\mathrm{ML}}(q)\frac{1}{a(L)}\sqrt{\frac{4\pi}{2L+1}}q^L\sum_M\sqrt{2}C^{L(M+k)}_{(1k)(LM)}Y^*_{L(M+k)}(\boldsymbol{e_q})\left[\tilde{T}_J^{LM}\right]^\dagger_{\beta'\beta}, \tag{5.40}$$

where μ_{ML} denotes the magnetic multipole moment.

The LO results for the magnetic form factors for a $J=3/2$ dimer read

$$G_{\mathrm{M1}}(q)=\frac{1}{r_1}\left[\frac{aL_{\mathrm{M}}+b\kappa_n+c\frac{q_c}{A_c}}{\mu_D}\right]\mu_N, \tag{5.41}$$

$$G_{\mathrm{M3}}(q)=\frac{-\sqrt{6}\kappa_n\mu_N}{\mu_O 10r_1(1-y)q^3}\left[2\gamma(1-y)q+\left((1-y)^2q^2-4\gamma^2\right)\arctan\left(\frac{(1-y)q}{2\gamma}\right)\right], \tag{5.42}$$

with A_c denoting the mass number of the core while a, b and c are functions given by

$$a=\left[r_1+3\left(\mu-\gamma\right)\right], \tag{5.43}$$

$$b=\frac{1}{(1-y)q}\left[\frac{21}{10}\gamma(1-y)q+\left(\frac{21}{20}(1-y)^2q^2+\frac{9}{5}\gamma^2\right)\arctan\left(\frac{(1-y)q}{2\gamma}\right)\right]-3\mu, \tag{5.44}$$

$$c=3y\mu-\frac{3}{4q}\left[2\gamma yq+\left(4\gamma^2+y^2q^2\right)\arctan\left(\frac{yq}{2\gamma}\right)\right]. \tag{5.45}$$

The first term in the numerator of Eq. (5.41) proportional to L_{M} is a contribution due to the direct magnetic moment coupling to the spin of the dimer field. The second term is a contribution due to the magnetic moment of the neutron proportional to κ_n. Finally,

the origin of third contribution proportional to q_c/A_c lies in the rotation of the charged core. This rotation induces a magnetic dipole moment and therefore contributes to the magnetic dipole form factor.

Again, the form factors should be normalized in the limit of vanishing photon momentum. Therefore, we demand

$$\lim_{q\to 0} G_{\mathrm{M1}}(q) \equiv 1, \tag{5.46}$$

$$\lim_{q\to 0} G_{\mathrm{M3}}(q) \equiv 1. \tag{5.47}$$

These limits determine the dipole and octupole moment to be

$$\mu_D = \left[L_{\mathrm{M}} + \frac{3(\mu-\gamma)}{r_1} \left(L_{\mathrm{M}} - \kappa_n + y\frac{q_c}{A_c} \right) \right] \mu_N, \tag{5.48}$$

$$\mu_O = -\frac{\sqrt{6}(1-y)^2 \kappa_n \mu_N}{15\gamma r_1}. \tag{5.49}$$

Inserting this octupole moment in Eq. (5.42) yields

$$G_{\mathrm{M3}}(q) = \frac{3\gamma}{2(1-y)^3 q^3} \left[2\gamma(1-y)q + \left((1-y)^2 q^2 - 4\gamma^2\right) \arctan\left(\frac{(1-y)q}{2\gamma}\right) \right] \tag{5.50}$$

$$= G_{\mathrm{E2}}[y \to (1-y)]. \tag{5.51}$$

This is the exact same result as in Eq. (5.31) except for the substitution $y \to (1-y)$ as indicated in Eq. (5.51).

6. EM Breakup and Structure of ^{31}Ne

In this Chapter, we apply our results from Chapter 5 to ^{31}Ne. In Section 6.1, we show universal correlations between different electromagnetic observables and give numerical predictions for the multipole moments as well as their corresponding radii. The deformation of ^{31}Ne is discussed in Section 6.2 while the E1 breakup is investigated in Section 6.3.

6.1. Electromagnetic Observables and Their Correlations

In the previous Chapter, we determined various electromagnetic form factors, which can be expanded for low q^2 in order to extract the corresponding radii:

$$G_{(\mathrm{E/M})L}(q) \approx 1 - \frac{1}{6}\langle r^2_{(\mathrm{E/M})L}\rangle q^2 + ..., \tag{6.1}$$

where $\langle r^2_{(\mathrm{E/M})L}\rangle$ denotes the expectation values of the electric or magnetic squared radii with multipolarity L, respectively.

The LO results for the electric monopole and quadrupole radii are

$$\langle r^2_{\mathrm{E0}}\rangle = -\frac{5y^2}{2\gamma r_1}, \tag{6.2}$$

$$\langle r^2_{\mathrm{E2}}\rangle = \frac{3y^2}{5\gamma^2}. \tag{6.3}$$

Given these radii, we can establish universal correlations to other observables. Considering the result for the quadrupole moment in Eq. (5.30), we find the correlation

$$\mu_Q = \frac{2}{15} q_c \langle r^2_{\mathrm{E0}}\rangle. \tag{6.4}$$

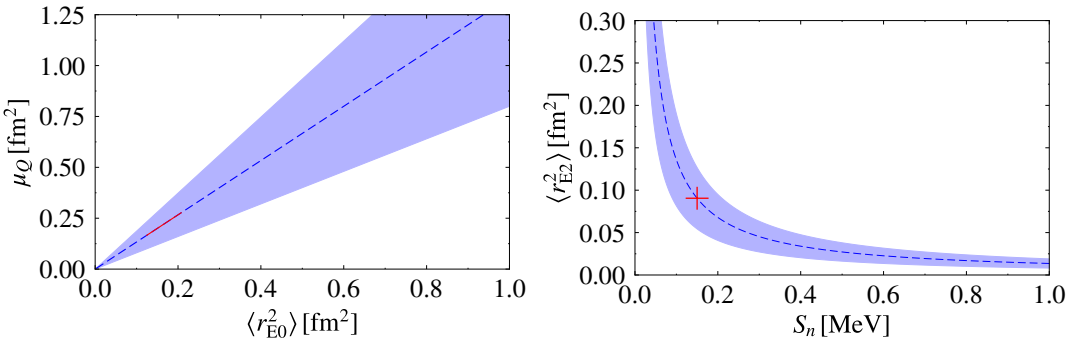

Figure 6.1.: Left panel: Correlation between the quadrupole moment and the squared charge radius. The red line indicates our results in case of r_1 within the estimated interval of $[-50, -30]$. Right panel: Correlation between the squared quadrupole radius and the neutron separation energy. The red cross indicates our result for $S_n = 0.15$ MeV. The blue shaded bands represent our EFT uncertainty.

This correlation is depicted in the left panel of Fig. 6.1. The red line indicates our results in case of r_1 within the estimated interval of $[-50, -30]$ MeV. Our results read

$$\sqrt{\langle r^2_{\rm E0}\rangle} \in [0.35(14), 0.46(18)] \text{ fm}\,, \tag{6.5}$$

$$\mu_Q \in [0.17(07), 0.28(11)] \text{ fm}^2\,, \tag{6.6}$$

where the numbers in parenthesis are the EFT uncertainties of 40%.

Furthermore, we find a correlation between the squared quadrupole radius $\langle r^2_{\rm E2}\rangle$ and the neutron separation energy S_n given by

$$\langle r^2_{\rm E2}\rangle = \frac{3y^2}{10 m_R}\frac{1}{S_n}. \tag{6.7}$$

It is depicted in the right panel of Fig. 6.1 where the red cross indicates our result for $S_n = 0.15$ MeV given by

$$\sqrt{\langle r^2_{\rm E2}\rangle} = 0.30(12) \text{ fm}. \tag{6.8}$$

The LO result for the squared magnetic octupole radius reads

$$\langle r^2_{\rm M3}\rangle = \frac{3(1-y)^2}{5\gamma^2} = \frac{3(1-y)^2}{10\mu}\frac{1}{S_n}. \tag{6.9}$$

This correlation between the squared octupole radius and the neutron separation energy is similar to the correlation in Eq. (6.7). The corresponding value for the octupole radius reads

$$\sqrt{\langle r^2_{\text{M3}}\rangle} = 9.0(3.6)\ \text{fm}\,. \tag{6.10}$$

Given the octupole moment in Eq. (5.49) and once again estimating r_1 yields the following result for the octupole moment

$$\mu_O \in [-23(9), -14(6)]\ \mu_N \text{fm}^2. \tag{6.11}$$

Since the magnetic dipole moment contains the counterterm proportional to L_{M}, it is not possible to predict its value. On the contrary, we need the magnetic dipole moment as an experimental input in order to determine the unknown parameter L_{M}. Having determined this parameter, it is then possible to predict the corresponding radius.

6.2. Nuclear Deformation

The appearance of higher multipole moments such as the electric quadrupole as well as the magnetic octupole moment indicates that ^{31}Ne is not a spherically symmetric nucleus. Following Ref. [75], we assume a quadrupolar deformed shape with a sharp edge at radius

$$R_{\text{def}} = R_0\left(1 + \beta_2 Y_{20}\right)/N, \tag{6.12}$$

where R_0 is the equilibrium radius, meaning the radius if the nucleus would be spherically symmetric. The additional term $\beta_2 Y_{20}$ accounts for the quadrupolar deformation where β_2 is called the deformation parameter. Having defined this surface radius and using $\beta_2 \ll 1$, we can relate it to the spectroscopic quadrupole moment via

$$\begin{aligned}\mu_Q\left(3/2\right) &= \frac{1}{5}\sqrt{\frac{16\pi}{5}}\frac{3}{4\pi} Z e R_0^2 \beta_2 \\ &= \sqrt{\frac{1}{5\pi}} Z e \beta_2 \langle r^2_{\text{E0}}\rangle.\end{aligned} \tag{6.13}$$

In the second line of Eq. (6.13) we used $\langle r^2_{\text{E0}}\rangle = (3/5)R_0^2$. As a result, we find a linear correlation between the quadrupole moment and the mean squared electric monopole radius. This is exactly the same correlation we found in our Halo EFT calculation and hence equating the proportionality factors allows us to determine the deformation parameter to be $\beta_2 = 0.53$. This value indicates a significant deformation due to the non-vanishing quadrupole moment.

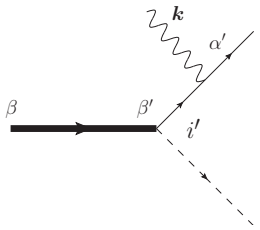

Figure 6.2.: E1 Breakup of ^{31}Ne into the continuum consisting of the core and neutron. We use the same notation as in Fig. 5.2.

6.3. E1 Breakup

In Fig. 6.2, we show the LO diagram contributing to the E1 breakup of ^{31}Ne. The photon transfers an angular momentum of 1 onto the two-body system consisting of the core and neutron. Since this two-body system is bound in a P-wave, the possible final angular momenta in the continuum are 0 and 2, corresponding to an S- and a D-wave, respectively.

The scalar transition amplitude in momentum space is given by

$$\Gamma_0^{\alpha'\beta} = \frac{i2m_R g_1 q_c e\sqrt{Z_\pi} C^{\frac{3}{2}\beta}_{(1i')(\frac{1}{2}\alpha')}(\boldsymbol{p} - y\boldsymbol{k})_{i'}}{\gamma_1^2 + (\boldsymbol{p} - y\boldsymbol{k})^2}\,, \tag{6.14}$$

$$= -iq_c e\,\langle \boldsymbol{p} - y\boldsymbol{k}|\psi^{\alpha'\beta}\rangle\,, \tag{6.15}$$

where $|\psi^{\alpha'\beta}\rangle$ represents the bound state of ^{31}Ne (see Appendix B.1), $\boldsymbol{p}$ is the relative momentum between the core and the neutron, while $\boldsymbol{k}$ is the photon momentum.

Without loss of generality, we choose the photon to be traveling in the $\hat{z}$-direction. We insert in Eq. (6.15) an identity operator in configuration space and express e^{iykz} by its plane wave expansion

$$e^{iykz} = \sqrt{4\pi}\sum_L \sqrt{2L+1} i^L j_L(ykz) Y_{L0}\,, \tag{6.16}$$

where $j_L(x)$ is the spherical Bessel function. In the low-energy limit, we use $j_L(ykz) \approx (ykz)^L/((2L+1)!!)$.

The scalar transition amplitude then reads

$$\Gamma_0^{\alpha'\beta} = -i \sum_L \int \mathrm{d}^3 r \, \langle \boldsymbol{p}| \, \hat{\tilde{\rho}}_L(\boldsymbol{r}) \, |\psi^{\alpha'\beta}\rangle \, \sqrt{4\pi}\sqrt{2L+1} i^L \frac{(kr)^L}{(2L+1)!!} Y_{L0} \,, \tag{6.17}$$

where

$$\hat{\tilde{\rho}}_L(\boldsymbol{r}) = e Z_{\text{eff}}^L \, |\boldsymbol{r}\rangle \, \langle \boldsymbol{r}| \tag{6.18}$$

with $Z_{\text{eff}}^L = q_c y^L$.

This means, that the photon in Fig. 6.2 transfers all possible angular momenta. For a specific angular momentum transfer, the amplitude reads

$$\Gamma_0^{\alpha'\beta}(\text{EL}; M=0) = -i \int \mathrm{d}^3 r \, \langle \boldsymbol{p}| \, \hat{\tilde{\rho}}_L(\boldsymbol{r}) \, |\psi^{\alpha'\beta}\rangle \, \sqrt{4\pi}\sqrt{2L+1} i^L \frac{(kr)^L}{(2L+1)!!} Y_{L0} \,. \tag{6.19}$$

The matrix element relevant for the calculation of the EL breakup is given by [76]

$$\mathcal{M}(\text{EL}; 0) = \int \mathrm{d}^3 r \, \langle \boldsymbol{p}| \, \hat{\tilde{\rho}}(\boldsymbol{r}) \, |\psi^{\alpha'\beta}\rangle \, r^L Y_{L0} \,, \tag{6.20}$$

$$= i \frac{(2L+1)!!}{k^L} (i)^{-L} \sqrt{\frac{1}{4\pi(2L+1)}} \Gamma_0^{\alpha'\beta}(\text{EL}; 0) \,. \tag{6.21}$$

Since we are interested in the E1 breakup, we set $L = 1$ in Eq. (6.21). Moreover, we plug in the bound state wave function in configuration space given by

$$\begin{aligned} \langle \boldsymbol{r}|\psi^{\alpha'\beta}\rangle &= -i\sqrt{\frac{-2\gamma_1^2}{r_1}} \frac{e^{-\gamma_1 r}}{r} \left(1 + \frac{1}{\gamma_1 r}\right) Y_{1i'}^* C^{\frac{3}{2}\beta}_{(1i')(\frac{1}{2}\alpha')} \\ &= C_\pi \frac{u(r)}{r} Y_{1i'}^* C^{\frac{3}{2}\beta}_{(1i')(\frac{1}{2}\alpha')} \,, \end{aligned} \tag{6.22}$$

with C_π denoting the asymptotic normalization constant (ANC) and $u(r)$ the radial wave function. They read

$$C_\pi = -i\sqrt{\frac{-2\gamma_1^2}{r_1}} \,, \tag{6.23}$$

$$u(r) = e^{-\gamma_1 r} \left(1 + \frac{1}{\gamma_1 r}\right) \,. \tag{6.24}$$

This yields

$$\mathcal{M}(\mathrm{E1};0) = eZ_{\mathrm{eff}}^{(1)} C_\pi \int \mathrm{d}^3 r e^{-i\boldsymbol{pr}} u(r) Y_{1i'}^* Y_{10} C^{\frac{3}{2}\beta}_{(1i')(\frac{1}{2}\alpha')} \,. \tag{6.25}$$

The product of the spherical harmonics in Eq. (6.25) can be expressed as an irreducible sum of spherical harmonics with $L = 0$ and $L = 2$. This allows us to extract the two relevant matrix elements for a transition into either an S-wave or a D-wave.

The $P \to S$ transition amplitude reads

$$\mathcal{M}(\mathrm{E1};0;P\to S) = \frac{eZ_{\mathrm{eff}}^{(1)} C_\pi}{\sqrt{4\pi}} \int \mathrm{d}^3 r e^{-i\boldsymbol{pr}} u(r) Y_{00} C^{\frac{3}{2}\beta}_{(10)(\frac{1}{2}\alpha')} \tag{6.26}$$

We use the plane wave expansion of $e^{-i\boldsymbol{pr}}$, integrate over $d\Omega$ and couple the angular momentum of $L = 0$ and the spin of the neutron to a two-particle continuum with total spin quantum numbers $(J'\beta')$ to find

$$\mathcal{M}^{J'\beta'\beta}(\mathrm{E1};0;P\to S) = eZ_{\mathrm{eff}}^{(1)} C_\pi \sqrt{4\pi} Y_{00}(\boldsymbol{e_p}) \int \mathrm{d}r j_0(pr) u(r) r^2 C^{\frac{3}{2}\beta}_{(10)(\frac{1}{2}\alpha')} C^{J'\beta'}_{(00)(\frac{1}{2}\alpha')} \tag{6.27}$$

We proceed similarly for the $P \to D$ transition amplitude and find

$$\begin{aligned}\mathcal{M}^{J'\beta'\beta}(\mathrm{E1};0;P\to D) = &- eZ_{\mathrm{eff}}^{(1)} C_\pi \sqrt{\frac{24\pi}{5}} \sum_m Y_{2m}(\boldsymbol{e_p}) (-1)^{i'} \\ &\times \int \mathrm{d}r j_2(pr) u(r) r^2 C^{2m}_{(1-i')(10)} C^{\frac{3}{2}\beta}_{(1i')(\frac{1}{2}\alpha')} C^{J'\beta'}_{(2m)(\frac{1}{2}\alpha')} \,.\end{aligned} \tag{6.28}$$

Performing the radial integral and sum (average) over final (initial) spins and multiply our results with a factor of 3 to make up for the fact that we chose the photon to propagate in the $\hat{z}$-direction, we finally get

$$\overline{|\mathcal{M}(\mathrm{E1};P\to S)|}^2 = e^2 Z_{\mathrm{eff}}^{(1)^2} |C_\pi|^2 \, 4\pi \, |Y_{00}(\boldsymbol{e_p})|^2 \, \frac{(3\gamma_1^2 + p^2)^2}{\gamma_1^2(\gamma_1^2+p^2)^4} \,, \tag{6.29}$$

$$\overline{|\mathcal{M}(\mathrm{E1};P\to D)|}^2 = e^2 Z_{\mathrm{eff}}^{(1)^2} |C_\pi|^2 \, \frac{24\pi}{5} \sum_m |Y_{2m}(\boldsymbol{e_p})|^2 \, \frac{4p^4}{\gamma_1^2(\gamma_1^2+p^2)^4} \left(C^{2m}_{(1-i')(10)} \right)^2 \,. \tag{6.30}$$

The differential E1 transition strength is given by [58]

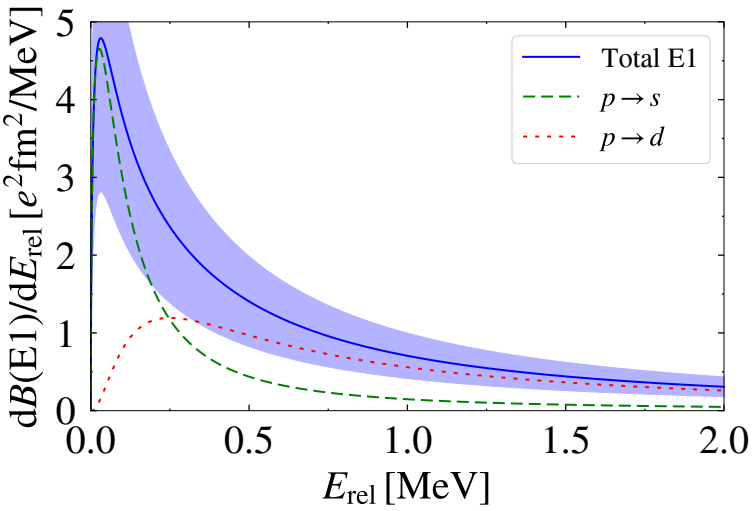

Figure 6.3.: Differential E1 transition strength of ^{31}Ne as a function of the relative energy $E = E_{\text{rel}}$ of the ^{30}Ne core and the neutron. Explanation of curves is given in inset.

$$\mathrm{dB(E1)} = |\mathcal{M}(\mathrm{E1})|^2 \, \frac{\mathrm{d}^3 p}{(2\pi)^3} \,. \tag{6.31}$$

Using $E = p^2/(2m_R)$, the differential E1 transition strength as a function of the relative energy E between the core and neutron reads

$$\frac{\mathrm{dB(E1)}}{\mathrm{d}E} = \frac{1}{(2\pi)^3} \int \mathrm{d}\Omega_{\boldsymbol{p}} m_R \, p \, |\mathcal{M}(\mathrm{E1})|^2 \,. \tag{6.32}$$

The final results for both transitions read

$$\frac{\mathrm{dB(E1}; P \to S)}{\mathrm{d}E} = e^2 Z_{\text{eff}}^{(1)2} \frac{m_R}{2\pi^2} \, |C_\pi|^2 \, \frac{p}{\gamma_1^2} \frac{(3\gamma_1^2 + p^2)^2}{(\gamma_1^2 + p^2)^4} \,, \tag{6.33}$$

$$\frac{\mathrm{dB(E1}; P \to D)}{\mathrm{d}E} = e^2 Z_{\text{eff}}^{(1)2} \frac{m_R}{\pi^2} \, |C_\pi|^2 \, \frac{p}{\gamma_1^2} \frac{4p^4}{(\gamma_1^2 + p^2)^4} \,. \tag{6.34}$$

The corresponding plots are given in Fig. 6.3. The total differential B(E1) transition strength is given in blue while the blue shaded band represents our uncertainty estimate according to our power counting. As expected for low-energy scattering, the S-wave contribution in the continuum is dominating.

6.4. Conclusion

We have applied the spherical formalism introduced in Chapter 5 and investigated the electromagnetic properties of ^{31}Ne. In our study of the electric properties, we found that our numerical predictions are fairly small. We calculated the charge radius to $\langle r^2_{\text{E0}}\rangle^{1/2} \in [0.35(14), 0.46(18)]$ fm, the quadrupole moment to $\mu_Q \in [0.17(07), 0.28(11)]$ fm^2 and the corresponding quadrupole radius to $\langle r^2_{\text{E2}}\rangle^{1/2} = 0.30(12)$ fm. The reason for our small predictions is that these observables are solely determined by the motion of the electrically charged core around the center of mass. Since the ^{30}Ne core is almost as heavy as the total system ^{31}Ne, this yields such small predictions. Therefore, we expect internal electric properties of the core to be important, at least in the electric sector. This is also reflected by the small separation of scales in ^{31}Ne. In the future, once more experimental data is available, we would like to include the first excited state of the ^{30}Ne core as an explicit degree of freedom within our Halo EFT. This would lead to more precise predictions in the electric sector and would also improve our power counting. Nevertheless, in the magnetic sector the observables result from the motion of the valence neutron around the center of mass. This means that corrections due to the internal core properties should be negligible which is confirmed by our large numerical predictions, $\langle r^2_{\text{M3}}\rangle^{1/2} = 9.0(3.6)$ fm and $\mu_O \in [-23(9), -14(6)]$ $\mu_N$fm^2. The large octupole radius reveals the size of the halo system. Unfortunately, the magnetic dipole moment cannot be predicted since it depends on the counterterm L_{M}.

In general, the non-vanishing higher multipole moments with multipolarity $L > 1$ indicate that ^{31}Ne is not a spherically symmetric nucleus. We extracted the β_2-deformation parameter from the linear correlation between the quadrupole moment and the charge radius and found $\beta_2 = 0.53$. This value indicates a significant deformation due to the quadrupole moment.

Moreover, we derived the differential B(E1) transition strength as a function of the relative energy E between the ^{30}Ne core and the neutron. Comparing this result to future data will help us to further determine unknown parameters which in turn enables us to improve our Halo EFT for ^{31}Ne.

7. Beta-Delayed Proton Emission and ^{11}Be

In this Chapter, we will consider for the first time the weak decay of the valence neutron of the halo nucleus ^{11}Be into the continuum within Halo EFT. This process, denoted $^{11}\text{Be} \to {}^{10}\text{Be} + p + e^- + \bar{\nu}_e$, is called beta-delayed proton emission from ^{11}Be. Parts of this Chapter have been published in this or similar form in our manuscript "β-delayed proton emission from ^{11}Be in effective field theory" (arXiv:1909.12206 [nucl-th]) [77].

7.1. Introduction

First experimental results for the rare decay mode were presented in Refs. [78], [79]. Riisager *et al.* [80] measured a surprisingly large branching ratio for this decay process of $b_p = 8.3(9) \times 10^{-6}$, which could only be explained in their Woods-Saxon model analysis if the decay proceeds through a new single-particle resonance in ^{11}B. This value is more than two orders of magnitude larger than the cluster model prediction by Baye and Tursunov [81]. This led Pfützner and Riisager [82] to suggest that β-delayed proton emission in ^{11}Be is also a possible pathway to detect a dark matter decay mode as proposed by Fornal and Grinstein [83]. More recently, in another experiment by Ayyad *et al.* [84], the branching ratio was remeasured as $b_p = 1.3(3) \times 10^{-5}$, similar in size to the previous measurement. Instead of detecting the decay product ^{10}Be as in the previous experiment, they directly measured the emitted protons and their energy distributions in the final channel and found new evidence for a low-lying resonance in ^{11}B with resonance energy $E_R = 0.196(20)$ MeV and width $\Gamma_R = 12(5)$ keV. Based on these resonance parameters, the authors calculated the decay rate in a Woods-Saxon model assuming a pure Gamow-Teller transition. They obtained $b_p = 8 \times 10^{-6}$, which has the correct order of magnitude but is only consistent within a factor of two with their experimental result. The work by Ayyad *et al.* was criticized in a recent comment by Fynbo *et al.* [85]. A new experiment by Riisager *et al.* [86] attempted to reproduce the results from their previous experiment. They extracted an upper limit for the

branching ratio of $b_p \leq 2.2 \times 10^{-6}$ but some questions remain due to inconsistencies between different measurements. In conclusion, the branching ratio for β-delayed proton emission in ^{11}Be remains an important unsolved problem.

The ground state of ^{11}Be is a well-understood S-wave halo nucleus. We describe it in Halo EFT with the ^{10}Be core and valence neutron as effective degrees of freedom. The expansion parameter of the power counting can be extracted from the ratio of the one-neutron separation energy of ^{11}Be and the excitation energy of the ^{10}Be core. Expressed in length scales, this ratio is given by $R_{\text{core}}/R_{\text{halo}} \approx 0.4$ [41] where R_{core} and R_{halo} denote the length scales of the core and halo, respectively. In principle, both the ^{10}Be core and the halo neutron can β-decay. Since the half-life of the neutron ($T_{1/2} = 10$ min) is much shorter than the half-life of the core ($T_{1/2} = 10^6$ a), it is safe to assume that for β-delayed proton emission it is always the halo neutron that decays in the halo picture. Therefore, one would naively expect the nucleus to emit this proton due to the repulsive Coulomb interaction: $^{11}\text{Be} \to {}^{10}\text{Be} + p + e^- + \bar{\nu}_e$.

This process has well-defined experimental signatures. However, it is also known that short-distance mechanisms such as the decay into excited states of ^{11}B (that are beyond the halo interpretation) dominate the total β-decay rate of ^{11}Be [17], [87].

Halo EFT offers a new perspective on β-delayed proton emission from ^{11}Be. It enables us to provide predictions for the decay observables in terms of a few measurable parameters including a robust uncertainty estimate. Thus, it is perfectly suited for the theoretical description of low-energy processes such as β-delayed proton emission from halo nuclei. Kong and Ravndal [88] used these ideas to successfully describe the inverse process of pp-fusion into a deuteron and leptons. In contrast to the previous calculation in Ref. [81], we will use new experimental input parameters and put additional emphasis on the uncertainties associated with using effective degrees of freedom. The halo neutron can β-decay through both the Gamow-Teller and Fermi operators. The Fermi operator can only connect states in the same isospin multiplet. If all neutrons in ^{11}Be contribute to the β-decay, this implies that the final state must have $T = 3/2$. No such states are currently known in ^{11}B within the β-decay window. However, due to the halo character of ^{11}Be we expect that only the halo neutron decays, such that the final state has no definite isospin. Thus, we will keep our analysis general and consider both the scenarios of Gamow-Teller and Fermi decay as well a pure Gamow-Teller decay in the following. Specifically, we will show that based on the measured branching ratio, a low-lying resonance is the likely reason for the large partial decay rate, confirming the suggestion of Ref. [80]. Furthermore, in ^{11}B, we explore the impact of the resonance energy and width on the

decay rate and show that the recent results for the resonance energy and width of a low-lying resonance are consistent with the experimentally measured branching ratio.

In order to keep the presentation self-contained, we start by summarizing the concepts of Halo EFT for S-wave halo nuclei. We discuss the calculation of decay rates with and without strong final state interactions and then display our results. We conclude with a summary.

7.2. Theoretical Foundations

The Halo EFT Lagrangian $\mathcal{L}$ for ^{11}Be as well as the low-lying resonance in ^{11}B up to next-to-leading order can be written as $\mathcal{L} = \mathcal{L}_0 + \mathcal{L}_d$, where $\mathcal{L}_0$ is the free Lagrangian of the ^{10}Be core, neutron and proton

$$\begin{aligned}\mathcal{L}_0 = c^\dagger \left(i\partial_t + \frac{\nabla^2}{2m_c} \right) c + n^\dagger \left(i\partial_t + \frac{\nabla^2}{2m_n} \right) n \\ + p^\dagger \left(i\partial_t + \frac{\nabla^2}{2m_p} \right) p \,,\end{aligned} \tag{7.1}$$

with c, n and p the core, neutron and proton fields, respectively. The masses of core, neutron and proton are denoted by m_c, m_n and m_p. The S-wave core-neutron as well as core-proton interaction are described by $\mathcal{L}_d$, which reads

$$\begin{aligned}\mathcal{L}_d = d_{\text{Be}}^\dagger \left[\eta \left(i\partial_t + \frac{\nabla^2}{2M_{nc}} \right) + \Delta \right] d_{\text{Be}} \\ + d_{\text{B}}^\dagger \left[\tilde{\eta} \left(i\partial_t + \frac{\nabla^2}{2M_{pc}} \right) + \tilde{\Delta} \right] d_{\text{B}} \\ - g \left[c^\dagger n^\dagger d_{\text{Be}} + \text{H.c.} \right] - \tilde{g} \left[c^\dagger p^\dagger d_{\text{B}} + \text{H.c.} \right] ,\end{aligned} \tag{7.2}$$

where d_{Be} and d_{B} are spinor fields, with spin indices suppressed, that represent the $J^P = 1/2^+$ ground state of ^{11}Be and the $J^P = 1/2^+$ low-lying resonance in ^{11}B, respectively, while $M_{nc} = m_n + m_c$ and $M_{pc} = m_p + m_c$.

The renormalization of the low-energy constants for ^{11}Be has been discussed in Ref. [41]. Here, we will briefly summarize the relevant results to define our notation. Due to the non-perturbative nature of the interaction, we need to resum the self-energy diagrams

to all orders. After matching the low-energy constants for ^{11}Be appearing in Eq. (7.2) to the effective range expansion, we obtain the full two-body T-matrix

$$T_0(E) = \frac{2\pi}{m_R}\left[\frac{1}{a_0} - r_0 m_R E - \sqrt{-2m_R E - i\epsilon}\right]^{-1} . \tag{7.3}$$

where m_R is the reduced mass, and a_0, r_0 are the S-wave ^{10}Be$-n$ scattering length and effective range, respectively. The residue at the bound state pole of Eq. (7.3) is required to calculate physical observables, $Z = \frac{2\pi\gamma_0}{m_R^2}/(1 - r_0\gamma_0)$, with $\gamma_0 = (1 - \sqrt{1 - 2r_0/a_0})/r_0 \equiv \sqrt{2m_R S_n}$ the binding momentum of the S-wave halo state, and S_n the one-neutron separation energy of the halo nucleus.

In order to investigate β-delayed proton emission from ^{11}Be, we include the weak interaction current allowing transitions of a neutron into a proton, electron and antineutrino which corresponds to the hadronic one-body current. Moreover, we have to consider hadronic two-body currents that appear in the dimer formalism once the effective range is included. The corresponding Lagrangian is given by

$$\mathcal{L}_{\text{weak}} = -\frac{G_F}{\sqrt{2}} l_-^\mu \left(\left(J_\mu^+\right)^{\text{1b}} + \left(J_\mu^+\right)^{\text{2b}} \right) , \tag{7.4}$$

where $l_-^\mu = \bar{u}_e \gamma^\mu (1 - \gamma^5) v_{\bar{\nu}}$ and $\left(J_\mu^+\right)^{\text{1b}} = (V_\mu^1 - A_\mu^1) + i(V_\mu^2 - A_\mu^2)$ denote the leptonic and hadronic one-body currents, respectively. Here the hadronic one-body current is decomposed into vector and axial-vector contributions. At leading order, the contributions to this current are $V_0^a = N^\dagger \frac{\tau^a}{2} N$, $A_k^a = g_A N^\dagger \frac{\tau^a}{2} \sigma_k N$, where $|g_A| \simeq 1.27$ is the ratio of the axial-vector to vector coupling constants [51]. Terms with more derivatives and/or more fields (many-body currents) will appear at higher orders. The first and second term give the conventional Fermi and Gamow-Teller operators, respectively. The two-body current is also decomposed into vector and axial-vector contributions and reads

$$\left(J_\mu^+\right)^{\text{2b}} = \begin{cases} -d_{\text{B}}^\dagger \, d_{\text{Be}} & \mu = 0 \, , \\ g_A \, d_{\text{B}}^\dagger \, \sigma_k \, d_{\text{Be}} & \mu = k = 1, 2, 3 \, . \end{cases} \tag{7.5}$$

7.3. Weak Matrix Element and Decay Rate

We ignore recoil effects in the β-decay and take both the Gamow-Teller and Fermi transitions into account. After lepton sums, spin averaging, and partial phase space

integration, we obtain the decay rate

$$\Gamma = \frac{G_F^2(1+3g_A^2)}{4\pi^5} \int dp \int dp_e p^2 p_e^2 (E_0 - E - E_e)^2 \times C^2(\eta_e)\, \overline{|\mathcal{A}(\mathbf{p})|^2}\, \Theta(E_0 - E - E_e)\,, \quad (7.6)$$

where $\mathcal{A}$ is the *reduced* hadronic amplitude for Gamow-Teller and Fermi transitions whose operator coefficients have been factored out and Θ is the Heaviside step function. Moreover, $\mathbf{p}$ is the relative momentum of the outgoing proton and core, while $E = p^2/(2m_R)$ is their kinetic energy. Furthermore, $E_0 = \Delta m - S_n$, where $\Delta m = 1.29$ MeV is the mass difference between neutron and proton, and $E_e = \sqrt{m_e^2 + p_e^2}$ is the energy of the electron.

The Sommerfeld factor of the electron is given by

$$C^2(\eta_e) = \frac{2\pi\eta_e}{(e^{2\pi\eta_e} - 1)}\,, \quad (7.7)$$

where $\eta_e = \alpha Z Z_e E_e/|\mathbf{p_e}|$ with $\alpha = 1/137$ the fine structure constant. We use $Z = Z_p$ in order to ensure that we reproduce the free neutron decay width in the limit of a vanishing one-neutron separation energy of ^{11}Be. This means that the electron is only interacting with the outgoing proton. We assume this to be a good approximation since the ^{10}Be core is far away from the decaying valence neutron due to the small one-neutron separation energy. If a pure Gamow-Teller transition is considered, the factor $1 + 3g_A^2$ is replaced by $3g_A^2$. This results in a reduction of the decay rate by 17 %.

7.4. Beta-Strength Sum Rule

The so-called Fermi and Gamow-Teller sum rules (also collectively known as beta-strength sum rule) count the number of weak charges that can decay in the initial state. We will require that this beta-strength sum rule is fulfilled at each order within our EFT power counting. For a transition into the continuum, the sum rule is exactly fulfilled when integrating the differential beta-strengths

$$\frac{dB_{\mathrm{F}}}{dE} = \frac{G_F^2}{4\pi^5}\, m_R \sqrt{2m_R E}\; \overline{|\mathcal{A}(\mathbf{p})|^2}\; \frac{m_e^5\, B}{\ln 2}\,, \quad (7.8)$$

$$\frac{dB_{\mathrm{GT}}}{dE} = 3\frac{dB_{\mathrm{F}}}{dE}\,, \quad (7.9)$$

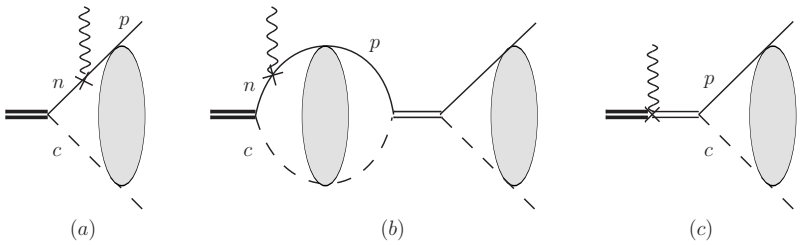

Figure 7.1.: (a): Feynman diagram for the weak decay of a one-neutron halo nucleus into the corresponding core and a proton with Coulomb final state interactions only. $(b) + (c)$: Contributions of strong final state interactions. The thin double line in the middle denotes the dressed ^{10}Be$-p$ propagator. The shaded ellipse denotes the Coulomb Green's function.

over the whole continuum where $B = 6147$ s is the β-decay constant [89]. In the halo picture, we therefore expect beta-strengths B_{F} and B_{GT} to be at most 1 and 3, respectively, when integrating over the available Q-window. The beta-strengths are related to the comparative half-life of a decay, the so-called ft value given by

$$ft = \frac{B}{B_{\mathrm{F}} + g_A^2 B_{\mathrm{GT}}}. \tag{7.10}$$

At LO where the full non-perturbative solution for a zero-range interaction is used in the incoming as well as outgoing channel, the sum rule is always satisfied. At NLO where range corrections are included, the sum rule puts strong constraints on the ranges in the incoming and outgoing channels such that only certain combinations are allowed.

7.5. Hadronic Current Without Final State Interactions

The amplitude for the charge changing weak transition of a two-body system is illustrated as diagram (a) of Fig. 7.1. It was first calculated in pionless EFT by Kong and Ravndal [88]. The corresponding hadronic current can be written as [90]

$$\mathcal{A}_C^{(a)}(\mathbf{p}) = -ig\sqrt{Z}C(\eta_p)e^{i\sigma_0}\frac{2m_R}{\mathbf{p}^2 + \gamma_0^2}e^{2\eta_p \arctan(|\mathbf{p}|/\gamma_0)}\,, \tag{7.11}$$

where σ_0 is the Coulomb phase and $C^2(\eta_p)$ is the Sommerfeld factor from Eq. (7.7). In the $^{10}\text{Be}-p$ system, the Sommerfeld parameter is $\eta_p = \alpha Z_p Z_c m_R/|\mathbf{p}|$, with $Z_p = 1$ and $Z_c = 4$.

7.6. Hadronic Current with Final State Interactions

The current (7.11) includes only the final state interaction from the exchange of Coulomb photons. We now consider strong final state interactions whose signature is a low-lying resonance in the $^{10}\text{Be}-p$ channel up to NLO. These contributions are shown as diagrams (b) and (c) of Fig. 7.1. Diagram (c) contributes only at NLO to the amplitude. It arises from a two-body current (with known coupling strength) that appears as a result of the energy-dependent interactions used in the initial state (see Eq. (7.2)) and the final state (see Ref. [36]). The thin double line together with the shaded ellipses that represent Coulomb Green's functions as depicted in diagram (b) essentially combine to the strong scattering amplitude T_{CS} given either in Eq. (7.12) or (7.18) [36], [88].

The degrees of freedom in Halo EFT are the emitted outgoing proton and ^{10}Be. Our treatment of the resonance follows Ref. [36]. The corresponding strong scattering amplitude modified by Coulomb corrections is [36]

$$T_{CS} = \frac{-4\pi/m_R}{\left(r_C - \frac{1}{3k_C}\right)\left(p^2 - k_R^2\right) + \frac{p^2}{3k_C} - 4k_C H(\eta_p)}\,, \tag{7.12}$$

where $H(\eta_p) = \text{Re}[\psi(1+i\eta_p)] - \ln\eta_p + \frac{i}{2\eta_p}C^2(\eta_p)$, with the digamma function $\psi(z)$. The parameters in Eq. (7.12) are directly related to the resonance momentum k_R and width Γ_R:

$$-\frac{1}{a_C} = -\left(r_C - \frac{1}{3k_C}\right)\frac{k_R^2}{2}, \tag{7.13}$$

$$r_C = -\frac{4\pi k_C}{m_R \Gamma_R}\frac{1}{e^{2\pi k_c/k_R} - 1} + \frac{1}{3k_C}, \tag{7.14}$$

where a_C and r_C are the Coulomb-modified scattering length and effective range, respectively. The resonance energy is given by $E_R = k_R^2/(2m_R)$.

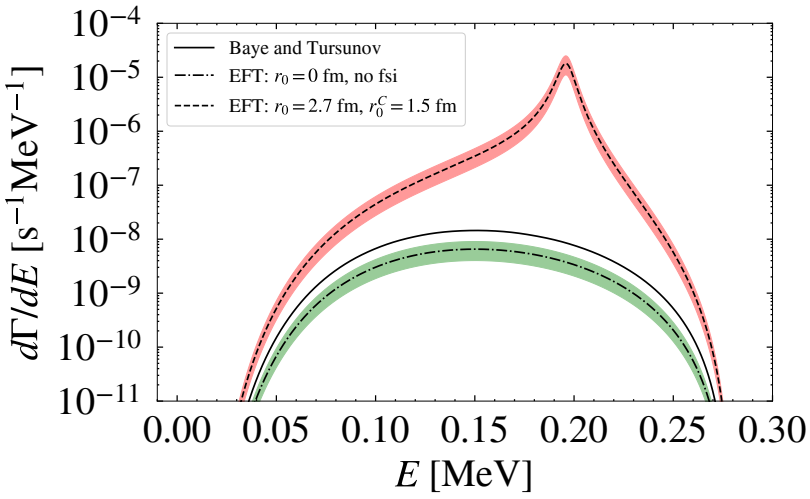

Figure 7.2.: Differential decay rate $d\Gamma/dE$ for β-delayed proton emission from ^{11}Be as a function of the final-state particle energy E. The dash-dotted line shows our EFT result without final state interactions while the solid line gives the result obtained by Baye and Tursunov [81]. The dashed line shows the EFT result including a resonance at $E_R = 0.196$ MeV in the outgoing channel at NLO. The colored bands give the EFT uncertainty.

The diagrams (b) and (c) of Fig. 7.1 lead to

$$\mathcal{A}_{CS}^{(b)} = -ig\sqrt{Z}4m_R^2 C(\eta_p) e^{i\sigma_0} \mathcal{I} T_{CS} \,, \tag{7.15}$$

$$\mathcal{A}_{CS}^{(c)} = -ig\sqrt{Z}4m_R^2 C(\eta_p) e^{i\sigma_0} \left(\frac{\sqrt{r_0 r_0^C}}{8\pi} \right) T_{CS} \,, \tag{7.16}$$

with the complex-valued integral

$$\mathcal{I} = \int \frac{d^3\mathbf{q}}{(2\pi)^3} \frac{C^2(\eta_q) e^{2\eta_q \arctan(|\mathbf{q}|/\gamma_0)}}{\mathbf{q}^2 + \gamma_0^2} \frac{1}{\mathbf{p}^2 - \mathbf{q}^2 + i\epsilon} \,. \tag{7.17}$$

The total amplitude $\mathcal{A}$ is the sum of the amplitudes with and without resonance $\mathcal{A} = \mathcal{A}_C^{(a)} + \mathcal{A}_{CS}^{(b)} + \mathcal{A}_{CS}^{(c)}$.

At LO, the Coulomb-modified effective range in the $^{10}\text{Be} - p$ system is zero and the

amplitude reduces to

$$T_{CS} = -\frac{2\pi}{m_R}\left[\frac{1}{-1/a_C - 2k_C H(\eta_p)}\right] . \tag{7.18}$$

7.7. Results Without Final State Interactions

We consider two scenarios: beta-delayed proton emission with and without final state interactions from a low-lying resonance in ^{11}B. We start with the first scenario and use the one-neutron separation energy of ^{11}Be $S_n = 0.5016$ MeV [17]. In Fig. 7.2, we plot the differential decay rate $d\Gamma/dE$ as a function of the kinetic energy E of the outgoing hadrons. The solid line gives the result obtained by Baye and Tursunov [81]. The dash-dotted line shows the EFT result with an uncertainty band obtained by adding an uncertainty of order $R_{\text{core}}/R_{\text{halo}} \approx 40$ % from higher order corrections. The remaining curve includes final state interactions and will be discussed below.

For the branching ratio, we obtain $b_p = \Gamma/\Gamma_{\text{total}} = (1.31 \pm 0.51) \times 10^{-8}$ where the EFT uncertainty is again estimated to be of the order of 40 %. Correspondingly, we obtain for the decay rate $\Gamma = (6.6 \pm 2.6) \times 10^{-10}\ \text{s}^{-1}$. Baye and Tursunov [81] obtain $\Gamma = 1.5 \times 10^{-9}\ \text{s}^{-1}$ which differs by a factor of 2.3 from our result. We note, however, that they used a Woods-Saxon potential with Coulomb interactions tuned to reproduce ^{11}B properties in the final state. Both theoretical results are significantly smaller than the experimental results reported in Refs. [78]–[80], [84].

7.8. Results with Final State Interactions

We now discuss the second scenario including final state interactions. In Fig. 7.3, we show the possible resonance parameter combinations that fulfill the beta-strength sum rule. The dash-dotted line is the result at LO where the effective range in the incoming channel as well as the Coulomb-modified effective range in the outgoing channel are zero. At NLO, we use $r_0 = 2.7$ fm determined in Ref. [41] from the measured B(E1) strength for Coulomb dissociation of ^{11}Be. The one-neutron separation energy as well as the effective range of ^{11}Be determine the Coulomb-modified effective range in the outgoing channel to be $r_0^C = 1.5$ fm. The sum rule is then satisfied to very good approximation for a wide range of Coulomb-modified scattering lengths in the outgoing channel. The

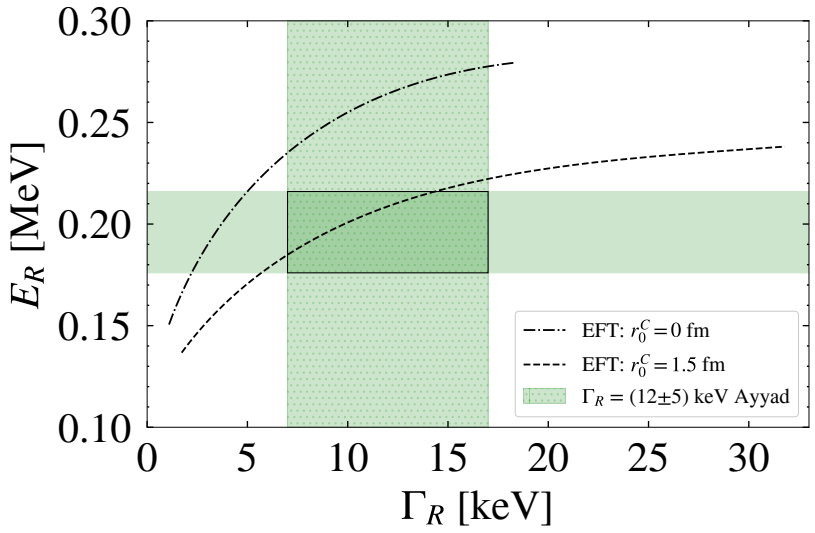

Figure 7.3.: Possible resonance parameter combinations fulfilling the sum rule. The dash-dotted line shows the combinations for $r_0 = 0$ fm at LO corresponding to $r_0^C = 0$ fm while the dashed line shows the combinations for $r_0 = 2.7$ fm at NLO corresponding to $r_0^C = 1.5$ fm. The green bands show the resonance parameters given in Ref. [84].

square shows the experimentally measured resonance parameter combinations given in Ref. [84]. Our NLO curve depicted as the dashed line exhibits combinations that are in agreement with this measurement as indicated by the overlap of the square and the curve.

In Fig. 7.4, we show the results for the decay rate as a function of the resonance energy at NLO while using the corresponding resonance width that satisfies the sum rule as shown in Fig. 7.3. The black line represents the decay rate obtained moving along the NLO curve in Fig. 7.3 while the red shaded envelope gives the theoretical uncertainty estimated from the counterterm contribution in the axial current scaling with $R_{\text{core}}/R_{\text{halo}} \approx 40$ %. The green bands show the experimentally measured branching ratio and resonance energy of Ref. [84]. The horizontal blue dashed line denotes the result of the model calculation carried out in Ref. [84] whereas the horizontal blue dash-dotted line gives the upper bound of Ref. [86]. Comparing our results with Ref. [86], we find that resonance energies $E_R \geq 0.214$ MeV give results compatible with this upper bound. The corresponding resonance widths can be read off in Fig. 7.3. When comparing our

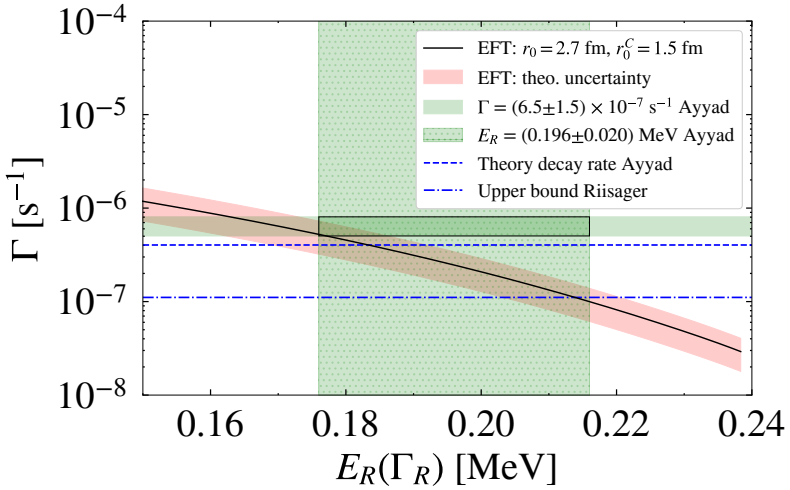

Figure 7.4.: Partial decay rate as a function of the resonance energy at NLO using the corresponding resonance width in accordance with the sum rule (see Fig 7.3). Explanation of curves and bands is given in inset. The Riisager upper bound is given in Ref. [86] and the values from Ayyad are given in Ref. [84].

results with Ref. [84], we find that the low-lying resonance measured in Ref. [84] with $E_R = 0.196(20)$ MeV and width $\Gamma_R = 12(5)$ keV is consistent with their experimentally measured branching ratio as indicated by the overlap of the square and the red shaded band. According to Fig. 7.3, we determine the width corresponding to the resonance energy $E_R = 0.196(20)$ MeV as $\Gamma_R = (9.0^{+4.8}_{-3.3}\text{(exp.)}^{+5.3}_{-2.2}\text{(theo.)})$ keV, which agrees well with the experimental value. Using this value for E_R, we calculate the logarithm of the comparative half-life $\log(ft) = 3.0$ with $B_{\text{GT}} = 2.88$ and $B_{\text{F}} = 0.96$ for a decay including both Gamow-Teller and Fermi transitions and $\log(ft) = 3.1$ with $B_{\text{GT}} = 2.88$ for a pure Gamow-Teller transition. The latter result can be compared to $\log(ft) = 4.8(4)$ calculated by Ayyad *et al.* [84] which was obtained using a pure Gamow-Teller transition as well, but is significantly larger than our result. This large $\log(ft)$ value was also criticized in the comment by Fynbo *et al.* [85]. Ayyad et. al corrected the value to $\log(ft) = 2.8(4)$ in their recent erratum [84]. This new value is now in good agreement with our result. Using the half-life for ^{11}Be given in Ref. [17] we convert the Halo EFT result for $E_R = 0.196(20)$ MeV and $\Gamma_R = (9.0^{+4.8}_{-3.3}\text{(exp.)}^{+5.3}_{-2.2}\text{(theo.)})$ keV into the final result for the branching ratio $b_p = 4.9^{+5.6}_{-2.9}\text{(exp.)}^{+4.0}_{-0.8}\text{(theo.)} \times 10^{-6}$. The corresponding differential decay rate is shown by the dashed line in Fig. 7.2.

7.9. Conclusion

In this Chapter, we considered β-delayed proton emission from ^{11}Be. We compared the scenario with no strong final state interactions with the scenario of a resonant enhancement in the final $^{10}\text{Be}-p$ channel up to NLO. In the case of no strong final state interactions, we obtained results that are in qualitative agreement with Baye and Tursunov with remaining small differences that can be explained by the different treatment of the final state channel. Including a low-lying resonance with the energy measured in Ref. [84] results in a resonance width and partial decay rate in agreement with this experiment. Thus, our model-independent calculation supports the experimental finding of a low-lying resonance[1]. Furthermore, we have explored the sensitivity of the partial decay rate to the resonance energy and decay width and found that this problem is fine tuned, *i.e.* only certain combinations of width and resonance energy can reproduce the partial decay rate. In contrast to the model calculation in Ref. [84], we included both, Fermi and Gamow-Teller transitions. However, if a pure Gamow-Teller decay is considered, their partial decay rate can also be reproduced with slightly smaller resonance parameters. Thus, our result implies that ^{11}Be is not a good laboratory to detect dark neutron decays since no exotic mechanism is needed to explain the partial decay rate.

The uncertainties are largely determined by higher order contributions of the EFT expansion. The next contribution within our power counting that we did not include is a counterterm contribution in the axial current scaling with $R_{\text{core}}/R_{\text{halo}}$. Uncertainties of the S-wave input parameter (the one-neutron separation energy) do not impact the total uncertainty significantly. Therefore, we estimate the uncertainty in the final decay rate to be approximately $R_{\text{core}}/R_{\text{halo}} \approx 40$ %. Experimental data with higher precision could be used to constrain the $^{10}\text{Be}-n$ and $^{10}\text{Be}-p$ interactions. It will be interesting to test whether the inclusion of this resonance changes the Halo EFT predictions for deuteron induced neutron transfer reactions off ^{11}Be which were investigated in Ref. [92].

[1] See Ref. [91] for another recent theoretical calculation in support of this resonance.

8. Universality in Charged Halos in 3d & 1d

In this Chapter, we discuss universal properties of weakly bound charged systems in three- and one-dimensional space. In particular, we focus on one-proton halo nuclei bound in an S-wave. For comparison, the universal properties for S-wave one-neutron halo nuclei are governed by the large scattering length a_0 or the small binding momentum γ_0 while corrections are given by higher order effective range expansion parameters which are treated perturbatively. For charged systems, the effective range expansion parameters are modified due to the presence of the Coulomb interaction and are called Coulomb-modified effective range expansion parameters. In addition to these parameters, the Coulomb force introduces an additional length scale D (or momentum scale k_C) for the description of the system under consideration.

Our approach for investigating such systems is the following. Firstly, we determine the wave function depending on the binding momentum γ_0 and the additional Coulomb momentum scale k_C. Secondly, using this wave function, we calculate the mean square radius $\langle r^2 \rangle$ and study its dependence on the Coulomb-modified effective range expansion parameters. This will allow us to conclude whether or not the impact of higher order parameters is important which in turn reveals the sensitivity of the system to short-distance physics.

We summarize the current literature regarding this topic in Sections 8.1 to 8.3 using the conventions introduced in Ref. [93]. In Sections 8.4 to 8.7, we derive the Coulomb-modified effective range expansion in 1d, extract the Halo EFT wave functions in 3d and 1d, and identify the universal regimes depending on the magnitude k_C.

8.1. Scattering Amplitude in 3d

We consider the scattering between the core and proton in the center-of-mass system with energy E and incoming and outgoing relative momenta $\boldsymbol{p}$ and $\boldsymbol{p}'$, respectively.

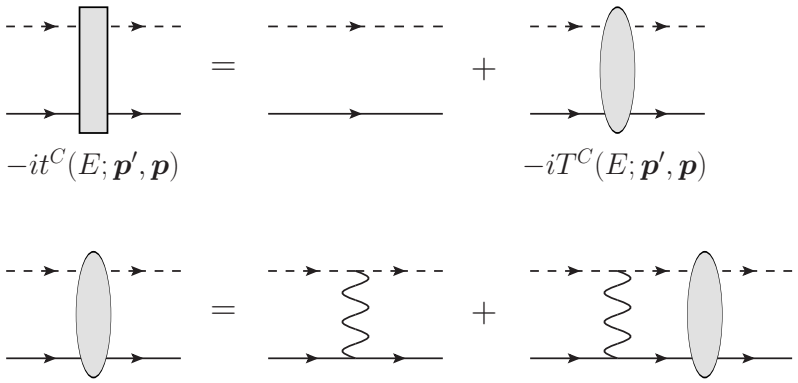

Figure 8.1.: Coulomb ladder diagrams. The dashed line denotes the core, the single solid line the proton, while the wavy lines represent photons.

They interact via multiple Coulomb photon exchanges which is why we resum the Coulomb ladder diagrams as depicted in Fig. 8.1. For the full dimer propagator, we sum a geometric series of dimer self-energies which also include multiple Coulomb photon exchanges as depicted in Fig. 8.2.

Then, the scattering amplitude is given by attaching external core and proton propagators to the full dimer which also interact via multiple photon exchanges in the initial and final channel as depicted in Fig. 8.3. The corresponding elastic scattering amplitude $T(E;\boldsymbol{p}',\boldsymbol{p})$ in the presence of both short-range strong and long-range Coulomb interactions can be written like

$$T(E;\boldsymbol{p}',\boldsymbol{p}) = T^C(E;\boldsymbol{p}',\boldsymbol{p}) + T^{SC}(E;\boldsymbol{p}',\boldsymbol{p})\,, \tag{8.1}$$

where T^C denotes the pure Coulomb contribution while T^{SC} is the so-called Coulomb-modified amplitude. As we are interested in the description of one-proton halo nuclei, only the Coulomb-modified amplitude which includes both the strong as well as Coulomb interaction is relevant. The corresponding partial wave expansion of the on-shell amplitude reads

$$\begin{aligned} T_l^{SC} &= T_l - T_l^C\,, \\ &= \frac{e^{2i(\sigma_l+\tilde{\delta}_l)}-1}{2ip} - \frac{e^{2i\sigma_l}-1}{2ip}\,, \\ &= \frac{p^{2l}e^{2i\sigma_l}}{p^{2l+1}(\cot\tilde{\delta}_l - i)}\,, \end{aligned} \tag{8.2}$$

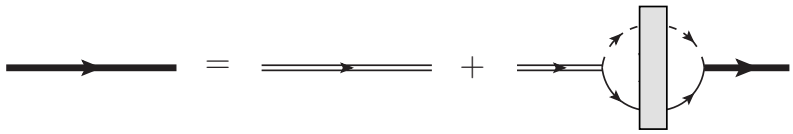

Figure 8.2.: Full dimer propagator in the presence of multiple photon exchanges. We use the same notation as in Fig. 8.1. In addition, the bare dimer propagator is given by the thin double line, while the thick line represents the full dimer propagator.

where $\sigma_l = \arg\Gamma(l+1+i\eta_p)$ is the Coulomb phase shift while $\tilde{\delta}_l$ is the so-called Coulomb-modified phase shift. Note that these phase shifts depend on the momentum p.

8.2. Coulomb-Modified Effective Range Expansion in 3d

The denominator in the last line of Eq. (8.2) has an effective range expansion called Coulomb-modified effective range expansion [93]. It reads

$$p^{2l+1}(\cot\tilde{\delta}_l - i) = \frac{-\frac{1}{a_l^C} + \frac{1}{2}r_l^C\, p^2 + \cdots - 2k_C p^{2l}\frac{C_l^2(\eta_p)}{C_0^2(\eta_p)}H(\eta_p)\left[\frac{\Gamma(2l+2)}{2^l\Gamma(l+1)}\right]}{C_l^2(\eta_p)\left[\frac{\Gamma(2l+2)}{2^l\Gamma(l+1)}\right]}\,, \tag{8.3}$$

where $\eta_p = \alpha Z_C Z_p m_R/p$ is the Sommerfeld parameter with $\alpha = e^2/(4\pi) \approx 1/137$ denoting the electromagnetic fine structure constant while Z_C and Z_p are the charge numbers of the core and proton, respectively. Moreover, the functions $C_l(\eta_p)$ and $H(\eta_p)$ are given by

$$C_l(\eta_p) = \frac{2^l e^{-\pi\eta_p/2}\,|\Gamma(l+1+i\eta_p)|}{\Gamma(2l+2)}\,, \tag{8.4}$$

$$H(\eta_p) = \Psi(i\eta_p) + \frac{1}{2i\eta_p} - \ln(i\eta_p)\,, \tag{8.5}$$

with $\Psi(x)$ the digamma function. The ellipses in Eq. (8.3) represent terms with higher powers in p^2. As indicated by the superscript C, the coefficients of the p^2 expansion in Eq. (8.3) are in general now Coulomb-modified parameters. The non-analytic part of the denominator is no longer given by ip^{2l+1} as for neutral systems but is replaced with

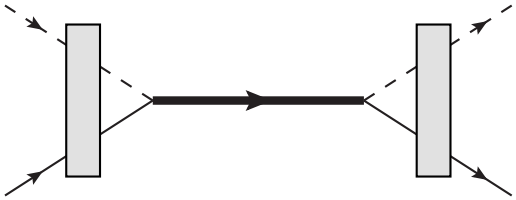

$$-iT^{SC}(E;\boldsymbol{p}',\boldsymbol{p})$$

Figure 8.3.: Scattering amplitude for two charged particles. We use the same notation as in Fig. 8.2.

the more complicated expression $2k_C p^{2l} \frac{C_l^2(\eta_p)}{C_0^2(\eta_p)} H(\eta_p) \left[\frac{\Gamma(2l+2)}{2^l \Gamma(l+1)}\right]$, which results from the finite non-analytic part of the self-energy.

Since we are interested in S-wave one-proton halo nuclei, we present the final result for the S-wave scattering amplitude

$$\begin{aligned} T_0^{SC} &= \frac{e^{2i\sigma_0}}{p\cot\tilde{\delta}_0 - ip} \\ &= \frac{e^{2i\sigma_0}}{-\frac{1}{a_0^C} + \frac{1}{2} r_0^C\, p^2 + \cdots - 2k_C H(\eta_p)}\,. \end{aligned} \tag{8.6}$$

The second line is obtained by inserting Eq. (8.3) into Eq. (8.2).

8.3. Scattering Amplitude in 1d

In one-dimensional space, there are only two "scattering angles", namely 0° and 180°, corresponding to forward- and backward-scattering, respectively. Therefore, we expect the partial wave expansion of the scattering amplitude to consist of only two contributions. Indeed, any analytic function on the interval $(-\infty, +\infty)$ can be written as a sum of unique even and odd parts [94]

$$g(x) = g_e(x) + g_o(x) = g_e(r) + \epsilon g_o(r)\,, \tag{8.7}$$

where $g_e(-x) = g_e(x)$ and $g_o(-x) = -g_o(x)$, and where $r = |x|$ and $\epsilon = x/|x|$. Thus, any function can be expanded in two "partial waves"

$$g(x) = \sum_{l=0,1} \epsilon^l g_l(r)\,, \tag{8.8}$$

with the definitions $g_0(x) = g_e(x)$ and $g_1(x) = g_o(x)$. In analogy to the S-wave in the three-dimensional case, we focus on the parity-symmetric partial wave given by $l = 0$. The corresponding Coulomb-modified scattering amplitude reads [95]

$$T_0^{SC} = \frac{e^{2i\sigma_0}}{\frac{1}{p}\cot\tilde{\delta}_0 - \frac{i}{p}}\,. \tag{8.9}$$

8.4. Coulomb-Modified Effective Range Expansion in 1d

In order to determine the partial wave expansion of the denominator in Eq. (8.9), we identify the non-analytic part in the denominator with the one resulting from the finite part of the self-energy (see Appendix C). The remaining terms are analytic in p^2 [95] where the coefficients are the corresponding effective range expansion parameters. For the parity-symmetric partial wave ($l = 0$), we find the Coulomb-modified effective range expansion

$$\frac{1}{p}\cot\tilde{\delta}_0 - \frac{i}{p} = -\frac{1}{a_0^C} + \frac{1}{2} r_0^C\, p^2 + \cdots - \frac{2\eta_p^2}{k_C} H(\eta_p)\,, \tag{8.10}$$

where the parameter a_0^C has dimension $(\text{length})^{-1}$ and r_0^C has dimension $(\text{length})^3$. Therefore, the scattering amplitude in Eq. (8.9) can be written as

$$T_0^{SC} = \frac{e^{2i\sigma_0}}{-\frac{1}{a_0^C} + \frac{1}{2} r_0^C\, p^2 + \cdots - \frac{2\eta_p^2}{k_C} H(\eta_p)}\,. \tag{8.11}$$

8.5. Halo EFT Wave Functions in Configuration Space

For the calculation of the wave function, we follow the procedure presented in Ref. [96]. We extract the wave function from the expansion of the fully interacting Green's function

around the bound state pole

$$G \sim \frac{|\psi\rangle \langle\psi|}{E + B_0} \text{ for } E \to -B_0 \,, \tag{8.12}$$

where G denotes the full Green's function and B_0 is the binding energy of the S-wave bound state.

The full Green's function fulfills

$$\begin{aligned} G &= G^0 + G^0 \left(T^C + T^{SC}\right) G^0 \\ &= G^0 + G^0 T^C G^0 + G^0 T^{SC} G^0 \\ &= G^C + G^0 T^{SC} G^0 \,, \end{aligned} \tag{8.13}$$

with G^0 and G^C denoting the free and Coulomb Green's function, respectively. They read

$$G^{0\pm} = \left(E - H^0 \pm i\epsilon\right)^{-1} \tag{8.14}$$

$$G^{C\pm} = \left(E - H^0 - V^C \pm i\epsilon\right)^{-1} \,, \tag{8.15}$$

where the signs of the $i\epsilon$ terms define the retarded and advanced Green's functions.

8.5.1. 3d Halo EFT Wave function

We evaluate both Eq. (8.12) and the last line of Eq. (8.13) in configuration space which yields

$$\lim_{E \to -B_0} \frac{\langle \boldsymbol{r}' | \psi \rangle \langle \psi | \boldsymbol{r} \rangle}{E + B_0} = \lim_{E \to -B_0} \langle \boldsymbol{r}' | \, G^0 T^{SC} G^0 \, | \boldsymbol{r} \rangle \,, \tag{8.16}$$

where we have used that the first term in the last line of Eq. (8.13) has no contribution to the pole. After inserting identity operators in momentum space and expanding the result for the T^{SC}-matrix around the bound-state pole, we finally find (see Appendix B.2)

$$\psi(\boldsymbol{r}) = -g_0 \sqrt{Z_\sigma} \, \langle \boldsymbol{r} | \, G^{C+}(-B_0) \, | \boldsymbol{0} \rangle \,. \tag{8.17}$$

Here, g_0 is the S-wave coupling and Z_σ denotes the wave function renormalization constant of the corresponding full dimer field. The combination $g_0^2 Z_\sigma$ including all possible higher effective range expansion parameters is given by

$$g_0^2 Z_\sigma = \frac{2\pi\gamma_0}{m_R^2} \frac{1}{\left[\frac{2k_C}{\gamma_0}\left(\frac{k_C}{\gamma_0}\Psi^1\left(\frac{k_C}{\gamma_0}\right) - 1\right) - 1 - r_0^C\gamma_0 + \cdots\right]}\,, \tag{8.18}$$

where Ψ^1 denotes the first derivative of the digamma function Ψ. The ellipses represent higher order effective range parameter terms of order $\mathcal{O}(\gamma_0^3)$.

In 3d, the closed expression for the Coulomb Green's function for a bound state in any partial wave is known [93] as

$$G_l^{C\pm}(-B_l, r', r) = -i\frac{m_R\gamma_l}{2\pi}\frac{F_l(\eta_{i\gamma_l}, i\gamma_l r')}{i\gamma_l r'}\frac{H_l^+(\eta_{i\gamma_l}, i\gamma_l r)}{i\gamma_l r}\,, \tag{8.19}$$

where the definition assumes $r' < r$ while $\gamma_l = \sqrt{2m_R B_l}$ is the binding momentum. The functions F_l and H_l^+ are given by

$$F_l(\eta_p, \rho) = C_l(\eta_p)2^{-l-1}(-i)^{l+1}M_{i\eta_p, l+1/2}(2i\rho)\,, \tag{8.20}$$

$$H_l^+(\eta_p, \rho) = (-i)^l e^{\pi\eta_p/2}e^{i\sigma_l(\eta_p)}W_{-i\eta_p, l+1/2}(-2i\rho)\,, \tag{8.21}$$

with conventionally defined Whittaker functions $M_{k,\mu}(z)$ and $W_{k,\mu}(z)$.

Therefore, the final 3d wave function in configuration space for an S-wave bound state reads

$$\psi(\boldsymbol{r}) = \frac{m_R g_0\sqrt{Z_\sigma}}{\sqrt{\pi}}\,\Gamma\left(1 + \frac{k_C}{\gamma_0}\right)\frac{W_{-k_C/\gamma_0, 1/2}(2\gamma_0 r)}{r}Y_{00}(\boldsymbol{e_r})\,. \tag{8.22}$$

Taking the limit $\gamma_0 \to 0$ and plugging in Eq. (8.18) yields

$$\psi(\boldsymbol{r}) = \sqrt{\frac{6k_C}{1 - 3r_0^C k_C}}\sqrt{8k_C r}\frac{K_1(\sqrt{8k_C r})}{r}Y_{00}(\boldsymbol{e_r})\,, \tag{8.23}$$

where K_1 is the modified Bessel function of the second kind with $n = 1$.

We note that once the wave function includes higher order terms of the Coulomb-modified effective range expansion, it is no longer normalized to one. For the calculation of expectation values, correction terms might have to be taken into account. In the future, the form of these correction terms will be investigated by using restrictions due to gauge symmetry. Subsequently, the order at which the correction terms enter follows from the power counting.

8.5.2. 1d Halo EFT Wave Function

For the 1d wave function, we use that the S-wave radial Schrödinger equation in 3d corresponds to the Schrödinger equation in 1d. This means that the solution is also given by the Whittaker function $W_{-k_C/\gamma_0,1/2}(2\gamma_0|x|)$. As a boundary condition, we choose that the limit $k_C \to 0$ reproduces the well-known solution for the neutral one-dimensional wave function. Including all possible effective range parameter contributions, this gives

$$\begin{aligned}\psi(x) = &\sqrt{\frac{\frac{4k_C}{\gamma_0}\left(\ln\left(\frac{k_C}{\gamma_0}\right) - \Psi\left(\frac{k_C}{\gamma_0}\right)\right) - \frac{2k_C}{\gamma_0}\left(\frac{k_C}{\gamma_0}\Psi^1(\frac{k_C}{\gamma_0}) - 1\right) - 1}{\frac{4k_C}{\gamma_0}\left(\ln\left(\frac{k_C}{\gamma_0}\right) - \Psi\left(\frac{k_C}{\gamma_0}\right)\right) - \frac{2k_C}{\gamma_0}\left(\frac{k_C}{\gamma_0}\Psi^1\left(\frac{k_C}{\gamma_0}\right) - 1\right) - 1 - \gamma_0^3 r_0^C}} \\ &\times \sqrt{\frac{\gamma_0}{\frac{2k_C}{\gamma_0}\left(\frac{k_C}{\gamma_0}\Psi^1\left(\frac{k_C}{\gamma_0}\right) - 1\right) - 1}}\,\Gamma\left(1 + \frac{k_C}{\gamma_0}\right) W_{-k_C/\gamma_0,1/2}(2\gamma_0|x|)\,.\end{aligned} \tag{8.24}$$

Taking the limit $\gamma_0 \to 0$ yields

$$\psi(x) = \sqrt{\frac{3k_C}{1 - 30k_C^3 r_0^C}}\,\sqrt{8k_C|x|}K_1\left(\sqrt{8k_C|x|}\right)\,. \tag{8.25}$$

8.6. Weak Coulomb Regime

We define the weak Coulomb regime by

$$k_C \ll \gamma_0 \ll M_{\text{hi}}\,. \tag{8.26}$$

Here, M_{hi} denotes the high momentum scale of the short-distance physics that is not treated explicitly within the Halo EFT under consideration. In this regime, Coulomb corrections can be treated perturbatively. Therefore, the power counting is basically the same one as for neutral systems. This means that the universal properties in 3d (1d) are also governed by the large scattering length a_0 (or scattering momentum) or small binding momentum γ_0 with no significant impact due to Coulomb corrections.

8.7. Strong Coulomb Regime

The strong Coulomb regime is defined by

$$\gamma_0 \ll k_C \ll M_{\rm hi}\,. \tag{8.27}$$

In this regime, the corrections due to Coulomb interactions have to be treated non-perturbatively. Therefore, Coulomb photon interactions have to be resummed to all orders. The power counting is modified due to the large Coulomb momentum scale $k_C \gg \gamma_0$. Roughly speaking, k_C takes over the role of the binding momentum γ_0.

For simplicity, we perform our analysis in the limit of vanishing binding momentum $\gamma_0 \to 0$ for which the results have analytic expressions. In this limit, the only parameters describing the system are the momentum scale k_C and r_0^C.

First of all, we emphasize that even in the limit of vanishing binding momentum, the wave functions in three- and one-dimensional space still depend on the effective range parameter r_0^C. For comparison, in neutral systems, the limit $\gamma_0 \to 0$ implies that all effective range parameters beyond a_0 are not contributing which is the reason that for large a_0, the universal properties are solely determined by this parameter. In the presence of the long-range Coulomb interaction, this is obviously no longer the case. That is already a first indication that one might need to include at least r_0^C for an adequate description of one-proton halo nuclei.

To further determine the importance of the parameter r_0^C and to get more quantitative insights, we calculate the mean square radius and discuss its dependence on r_0^C, or rather on the dimensionless quantity $r_0^C k_C$. We use the Halo EFT wave functions calculated in the previous Section. In the 3d case, we calculate

$$\langle r^2\rangle = \frac{1}{1-3k_C r_0^C}\frac{9}{35}\frac{1}{k_C^2}\,. \tag{8.28}$$

Note that in contrary to neutral systems, the value for $\langle r^2\rangle$ in the limit $\gamma_0 \to 0$ is not diverging (for $r_0^C \neq 1/(3k_C)$). We show the corresponding plot for the mean square radius in units of $\langle r^2\rangle_{r_0^C k_C=0}$ as a function of $r_0^C k_C$ in Fig. 8.4. In this plot, we compare the Halo EFT results given in blue to different model potential calculations (data from Ref. [97]). In general, we see that the dependence of $\langle r^2\rangle / \left(\langle r^2\rangle_{r_0^C k_C=0}\right)$ on $r_0^C k_C$ is rather small for $r_0^C k_C < 0.15$. Approaching the value of $r_0^C = 1/(3k_C)$, the dependence on $r_0^C k_C$ gets strong leading to large corrections due to the inclusion of r_0^C. This value is

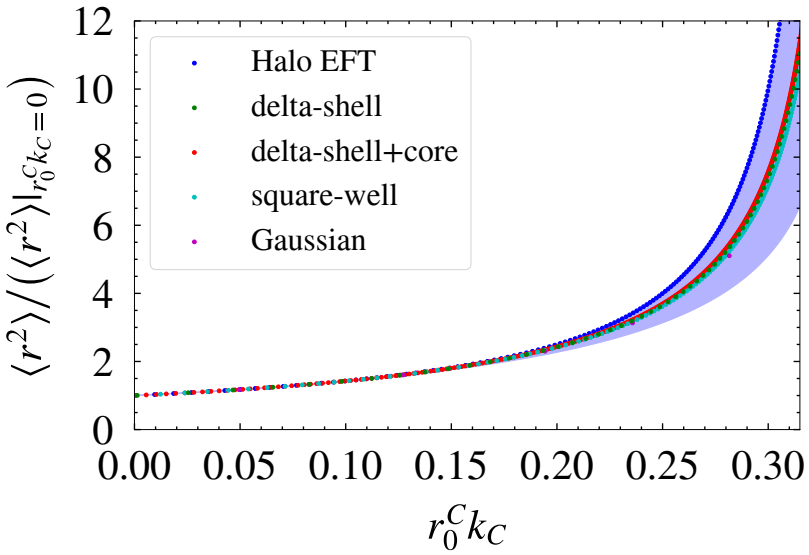

Figure 8.4.: $\langle r^2\rangle$ in units of $\langle r^2\rangle_{r_0^C k_C=0}$ as a function of $r_0^C k_C$. Explanation of different curves is given in inset.

the so-called Wigner causality bound (Wigner bound) for the effective range parameter. In Ref. [98], Phillips and Cohen derived this bound for S-wave scattering with finite-range interactions. It is a result from constraints of causality for two-body scattering which was first derived for finite-range interactions by Wigner [99].

For the calculation of the Wigner bound for r_0^C, we assume the following behavior of the Halo EFT wave function: At large distances ($r \geq R$), it is identical to the unknown exact wave function while at short distances ($r < R$) it is greater or equal than the unknown exact one which falls off to zero at the origin. This implies that the asymptotic normalization coefficient (ANC) of the exact wave function is coinciding with the one of Halo EFT wave function. The parameter R can be estimated by $1/M_{\text{hi}}$. This implies that the unknown short-distance physics lies in the interval $(0, R)$.

From the normalization condition of the exact wave function

$$1 = \int_0^R u^2(r)\mathrm{d}r + \int_R^\infty v^2(r)\mathrm{d}r\,, \tag{8.29}$$

we can derive an expression for r_0^C depending on R. Here, $u(r)$ and $v(r)$ denote the radial wave functions of the unknown exact wave function and the Halo EFT wave

function, respectively. Using the relations

$$\int_0^\infty v^2 \mathrm{d}r = \frac{C_\sigma^2}{6k_C} \tag{8.30}$$

$$= \frac{1}{1-3k_C r_0^C}\,, \tag{8.31}$$

where C_σ denotes the ANC and assuming that both ANCs coincide

$$v(r) = C_\sigma \tilde{v}(r)\,, \tag{8.32}$$

$$u(r) = C_\sigma \tilde{u}(r)\,, \tag{8.33}$$

yields

$$r_0^C = 2\int_0^R (\tilde{v}^2(r) - \tilde{u}^2(r))\mathrm{d}r\,. \tag{8.34}$$

For $u \leq v$, the Wigner bound for r_0^C is given by

$$\begin{aligned}\left(r_0^C\right)^{\max} &= 2\int_0^R \tilde{v}^2(r)\mathrm{d}r \\ &= \frac{\sqrt{\pi}}{8k_C} G_{1,1}^{3,1}\left(\begin{smallmatrix}1,5/2\\1,2,3,0\end{smallmatrix}\middle|\, 8k_C R\right)\,,\end{aligned} \tag{8.35}$$

where $G_{p,q}^{m,n}\left(\begin{smallmatrix}a_1,\ldots,a_p\\b_1,\ldots,b_q\end{smallmatrix}\middle|\, z\right)$ is the Meijer G-function.

According to Eq. (8.35), we can establish a relation between the Wigner bound for the effective range $\left(r_0^C\right)^{\max}$ and the parameter R. This is depicted in Fig. 8.5 as the solid red line. The other curves are the corresponding model potential results [97] which lie below our calculated upper bound.

Again using $u \leq v$, we can determine the maximal uncertainty estimate for the mean square radius similar to the Wigner bound calculation for r_0^C:

$$\Delta\langle r^2\rangle^{\max} = \int_0^R v^2(r) r^2 \mathrm{d}r \tag{8.36}$$

This approach can be generalized to other observables. We refer to this estimation as the uncertainty estimation based on the Wigner bound calculation. For our numerical calculations of the uncertainty, we estimate the unknown parameter R using the maximal

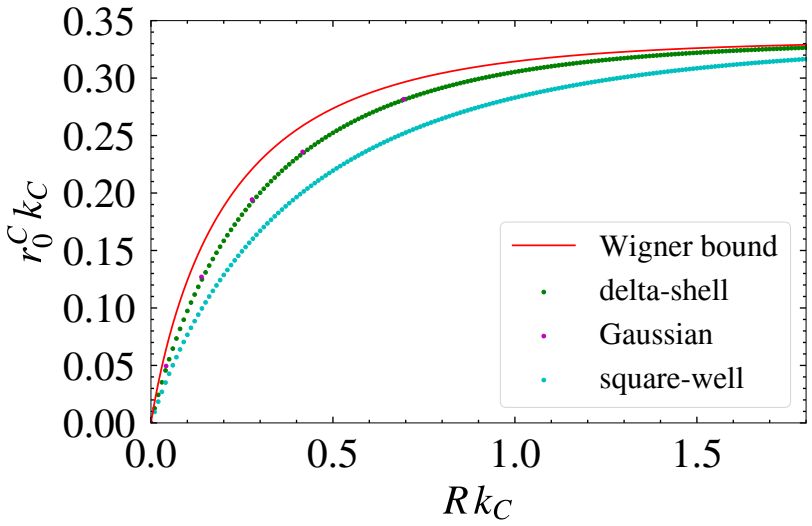

Figure 8.5.: Relation between $r_0^C k_C$ and Rk_C for the different model potentials and for the Wigner bound. Explanation of curves is given in inset.

value for a given r_0^C resulting from the model-potential calculations as depicted in Fig. 8.5. The corresponding uncertainty band is shown in Fig. 8.4. From this plot, we can conclude that we expect small corrections due to the Coulomb-modified effective range parameter r_0^C for $r_0^C k_C < 0.15$. This is corroborated by the fact that in this region, the maximal uncertainties are very small and that basically all results using different model potentials lie on top of our Halo EFT result. However, once $r_0^C k_C$ approaches the Wigner bound, the corrections due to r_0^C as well as the uncertainties get very large. Hence, in the regime close to the Wigner bound, in the *Wigner-saturated regime*, we find that the inclusion of the effective range parameter r_0^C is important and therefore has to be treated at LO. Otherwise, the corrections from LO to NLO would be unnaturally large indicating an inconsistent power counting of the Halo EFT.

In nuclear physics, we find that most systems are realized in the strong Coulomb regime close to the Wigner bound, in the so-called *Wigner-saturated regime*. Thus, we expect that for one-proton halo nuclei the inclusion of the effective range parameter r_0^C is crucial for precise predictions, see also Refs. [100], [101]. This suggests to construct a one-proton Halo EFT treating r_0^C at LO. Ryberg *et al.* [102] calculated the charge radius for the S-wave one-proton halo nucleus ^{17}F and employed one parameter at leading order and found that the inclusion of the effective range results in a $3.6 - 3.8$ larger

charge radius, also indicating the hierarchy-of-scales problem.

In 1d, we also find a finite $\langle r^2 \rangle$ determined by k_C and r_0^C. The mean square radius is given by

$$\langle r^2 \rangle = \frac{1}{1 - 30 k_C^3 r_0^C} \frac{9}{35} \frac{1}{k_C^2} \,. \tag{8.37}$$

Therefore, we also expect to find large corrections due to r_0^C close to the 1d Wigner bound of $\left(r_0^C\right)^{\text{max}} = 1/(30 k_C^3)$. We note, that due to the factor of 30, this behavior is even further enhanced.

8.8. Conclusion

We investigated the universal properties of S-wave one-proton halo nuclei in the weak and strong Coulomb regime. In the weak Coulomb regime, defined by $k_C \ll \gamma_0 \ll M_{\text{hi}}$, Coulomb corrections can be treated perturbatively. Therefore, the power counting is the same one as for neutral systems. This implies that the universal properties in 3d (1d) are given solely by the large scattering length (scattering momentum). In the strong Coulomb regime, defined by $\gamma_0 \ll k_c \ll M_{\text{hi}}$, Coulomb interactions have to be treated non-perturbatively. In this regime, the power counting is modified due to the large Coulomb momentum scale $k_C \gg \gamma_0$. Roughly speaking, k_C takes over the role of the binding momentum γ_0. Moreover, we find that corrections due to the parameter r_0^C are important in the so-called *Wigner-saturated regime*. In this saturated regime, the effective range r_0^C is close to the Wigner causality bound parametrized by k_C. Since in nuclear physics most systems are realized in the *Wigner-saturated regime*, the parameter r_0^C has to be treated at LO in the Halo EFT power counting. Observables are then largely driven by the parameters k_C and r_0^C. Therefore, we call such systems less universal as compared to the weak Coulomb or the neutral scenario. Possible higher order counterterms can be estimated by our uncertainty estimate based on the Wigner bound calculation. This allows to describe one-proton halo nuclei within Halo EFT with a consistent power counting and realistic theoretical uncertainties. In the future, we would like to apply our results to the S-wave one-proton halo nucleus ^{17}F and confront our findings with previous calculations [101], [102] and experimental data [103]. This will allow testing our proposed power counting as well as our new approach to assign theoretical uncertainties based on the Wigner bound calculation.

9. Summary and Outlook

In this thesis, we investigated electroweak properties of halo nuclei. Our theoretical approach to describe these exotic nuclei is called Halo EFT. It exploits the significant scale separations in halo nuclei and allows making predictions with quantified theoretical uncertainties. In general, results calculated in Halo EFTs are universal, meaning that they do not depend on the details of the underlying microscopic interactions.

We studied three different halo nuclei including four different halo states: the ground states of ^{11}Be, ^{31}Ne and ^{15}C as well as the first excited state of ^{15}C. Their quantum numbers and corresponding partial wave interactions read:

- ^{11}Be: $J^P = 1/2^+$, S-wave interaction
- ^{31}Ne: $J^P = 3/2^-$, P-wave interaction
- ^{15}C: $J^P = 1/2^+$ S-wave and $J^P = 5/2^+$ D-wave interaction

For each system, we constructed a dedicated Halo EFT reflecting the quantum numbers under consideration. Thereby, we showed that a Halo EFT using a spherical basis rather than Cartesian coordinates is better suited for the inclusion of higher partial wave interactions (in particular P-wave and D-wave interactions). Such a formalism uses the correct number of degrees of freedom by construction and therefore leads to more compact expressions, yielding more feasible calculations.

In Chapter 4, we studied the ground and the first excited state of ^{15}C. For this purpose, we extended the Halo EFT approach for electric observables to shallow D-wave bound states using the standard Cartesian coordinates. We outlined the basic framework for extending Halo EFT to higher partial waves. We developed a power counting for shallow bound states in an arbitrarily high partial wave. It is based on the requirement of a minimal number of fine-tuned parameters needed to generate the shallow bound state. Based on the assumption that a large number of fine tunings is less natural, we found that shallow bound states are less likely to occur in higher partial waves than in lower ones. This

trend is also observed experimentally [104]. By applying our general results for shallow D-wave states to ^{15}C, we investigated electromagnetic transitions of ^{15}C as well as its structure. We determined the electric form factors and extracted the corresponding multipole moments as well as their corresponding radii at NLO and computed the B(E2) transition strength at LO. Due to the lack of data for the first excited $5/2^+$ state, numerical predictions for the computed observables were impossible. However, comparing our result for the B(E2) transition strength to the measured B(E2) data [28] allowed us to predict the hexadecapole moment $\mu_H^{(d)} = 1.68(4)(50) \times 10^{-2}$ fm^4 and the corresponding radius $\langle r_H^2 \rangle^{(d)} = 0.135(3)(40)$ fm^2, where the first uncertainty is due to the experimental input and the second one is our EFT uncertainty of 30%. Moreover, we exploited the universal correlation between the reduced E2 transition strength B(E2) and the quadrupole moment in order to determine the unknown counterterm by fitting it to *ab initio* results from the IT-NCSM [30]. In doing so, we were able to predict the quadrupole moment to be $\mu_Q^{(d)} = -4.21(10)(1.26)$ fm^2. With this result, we also predicted the quadrupole radius for ^{15}C to be $\langle r_Q^2 \rangle^{(d)} = 7.70(17)(2.31) \times 10^{-2}$ fm^2, using universal correlations from our Halo EFT. These correlations are not obvious in *ab initio* approaches, since the separation of scales is not explicit in the parameters of the theory. This demonstrates the complementary character of Halo EFT with regard to *ab initio* methods. In principle, universal correlations allow to extract information even from unconverged *ab initio* calculations since the correlations are universal. This proves the usefulness of our Halo EFT approach even for D-wave bound states, but also demonstrates the limiting factors for the extension to higher partial waves due to the lack of known parameters.

In Chapter 6, we investigated the one-neutron halo nucleus ^{31}Ne within a P-wave Halo EFT using a spherical basis which was introduced in Chapter 5. Again, we determined the static electromagnetic properties by calculating the form factors. From these, we extracted the corresponding multipole moments and radii in the electric and magnetic sector. The numerical predictions in the electric sector are fairly small, $\langle r_{\text{E0}}^2 \rangle^{1/2} \in [0.35(14), 0.46(18)]$ fm, $\mu_Q \in [0.17(07), 0.28(11)]$ fm^2 and $\langle r_{\text{E2}}^2 \rangle^{1/2} = 0.30(12)$ fm, where the uncertainties result from our EFT uncertainty of 40%. This can be explained by the fact that these observables are solely determined by the motion of the electrically charged core around the center of mass. Since the ^{30}Ne core is almost as heavy as the total system ^{31}Ne, yields such small predictions. Therefore, we expect internal electric properties of the core to be important, at least in the electric sector. This is also reflected by the small separation of scales in ^{31}Ne. Nevertheless, in the magnetic sector the observables for the octupole moment and the corresponding radius result

from the motion of the valence neutron around the center of mass. This means that corrections due to the internal core properties should be negligible. In fact, we calculated $\langle r^2_{\mathrm{M3}}\rangle^{1/2} = 9.0(3.6)$ fm and $\mu_O \in [-23(9), -14(6)]\ \mu_N\mathrm{fm}^2$, where the large octupole radius reveals the size of the halo system. Unfortunately, the magnetic dipole moment cannot be predicted since it depends on the counterterm L_{M}. Furthermore, the non-vanishing higher multipole moments indicate that ^{31}Ne is not a spherically symmetric nucleus. From the linear correlation between the quadrupole moment and the charge radius, we extracted the β_2-deformation parameter to be $\beta_2 = 0.53$. This value indicates a significant deformation due to the quadrupole moment. Moreover, we studied the E1 breakup into the continuum consisting of the ^{30}Ne core and the neutron. We calculated the differential B(E1) transition strength as a function of the relative energy between the ^{30}Ne core and the neutron. This will help us to further determine unknown parameters by comparing our predictions to experimental data once they are available. The data analysis of the experiment by Nakamura *et al.* [73] is ongoing. In general, more experimental input would help us improving our predictions in the electric sector by treating the first excited state of the ^{30}Ne core as an explicit degree of freedom within our Halo EFT. This would also improve our power counting and would lead to more precise predictions.

In Chapter 7, we performed a pilot study of the weak decay of the valence neutron of ^{11}Be into the continuum. This process, denoted $^{11}\mathrm{Be} \to {}^{10}\mathrm{Be} + p + e^- + \bar{\nu}_e$, is called beta-delayed proton emission from ^{11}Be. The experimental determination of the branching ratio [80], [84], [86] remains an unsolved problem due to inconsistent measurements in different experiments. We compared our findings including theoretical uncertainties to experiment and found that the inclusion of strong final state interactions is needed to reproduce the correct order of the partial decay rate. Therefore, we included a resonant enhancement in the final ^{10}Be-p channel up to NLO according to the recently discovered low-lying resonance in ^{11}B by Ayyad *et al.* [84]. Using their measurement for the resonance energy $E_R = 0.196(20)$ MeV, yields a resonance width and branching ratio of $\Gamma_R = (9.0^{+4.8}_{-3.3}\text{(exp.)}^{+5.3}_{-2.2}\text{(theo.)})$ keV and $b_p = 4.9^{+5.6}_{-2.9}\text{(exp.)}^{+4.0}_{-0.8}\text{(theo.)} \times 10^{-6}$, respectively. These numbers agree with the experimental values $\Gamma_R = 12(5)$ keV and $b_p = 1.3(3) \times 10^{-5}$. Thus, our model-independent calculations support the experimental finding of this low-lying resonance. In future, experimental data with higher precision could be used to further constrain the ^{10}Be-n and ^{10}Be-p interactions. Moreover, it will be interesting to study the impact of the inclusion of this resonance in other Halo EFT calculations, e.g., for deuteron-induced neutron transfer reactions of ^{11}Be which were investigated in Ref. [92].

In Chapter 8, we investigated weakly bound systems of charged particles in three- and

one-dimensional space. In particular, we considered one-proton halo nuclei bound in an S-wave. In addition to the strong force binding these nuclei, the charged particles also interact via the repulsive Coulomb force, introducing an additional length scale D (or momentum scale k_C) to the system. Depending on the magnitude of D (or k_C) and the Coulomb-modified scattering length a_C, we identified different universal regimes by studying the corresponding wave function as well as the mean square radius $\langle r^2 \rangle$. Expressed in momentum scales, we found that in the weak Coulomb regime, defined by $k_C \ll \gamma_0 \ll \mathrm{M_{hi}}$, the power counting is basically the same as for neutral halos, where γ_0 is the S-wave binding momentum. This implies that the system exhibits universal properties dominated by the large Coulomb-modified scattering length a_C. Coulomb corrections and higher-order corrections from the effective range expansion can be treated perturbatively. This is true in three- and one-dimensional space. In the strong Coulomb regime defined by $\gamma_0 \ll k_C \ll \mathrm{M_{hi}}$, we treat Coulomb corrections nonperturbatively. For simplicity, we focused on the limit $\gamma_0 \to 0$. The power counting is modified due to the large Coulomb momentum scale $k_C \gg \gamma_0$. Roughly speaking, k_C takes over the role of the binding momentum $\gamma_0 \sim M_{\mathrm{lo}}$. In three- and one-dimensional space, we found that corrections due to the Coulomb-modified effective range parameter r_0^C are important (see also Refs [100]–[102]) once the parameter is close to the Wigner causality bound. We call this regime the *Wigner-saturated regime*. For a consistent power counting within that regime, the parameter r_0^C has to be treated at LO. In this case, observables are largely driven by k_C as well as r_0^C. Therefore, we call such systems less universal as compared to the weak Coulomb or the neutral scenario. Higher order contributions solely result from counterterms that can be estimated according to our uncertainty estimate based on the Wigner bound calculation proposed in Chapter 8. Since in nuclear physics most systems are realized in the *Wigner-saturated regime*, our proposed power counting as well as the uncertainty estimate based on the Wigner bound calculation allows for a systematic description of one-proton halo nuclei including realistic theoretical uncertainties.

In the future, it would be interesting to confront our findings with experimental data. It would allow testing our proposed power counting with our new approach to assign theoretical uncertainties in Halo EFT for charged systems. More specifically, we would like to apply our results to the S-wave one-proton halo nucleus ^{17}F and compare them to previous calculations [101], [102] and experimental data [103]. Moreover, we could extend our approach to the three-body sector. This would allow us to go beyond one-proton halo nuclei and study for example the two-proton halo nucleus ^{17}Ne [104].

Appendices

A. Dimer Propagator

A.1. *S*-Wave Propagator

The dressed σ propagator and the S-wave scattering amplitude are computed by summing the bubble diagrams analog to the D-wave case shown in Fig. 4.1. The result for the dressed σ propagator is

$$D_\sigma(p) = \frac{1}{\Delta_0 + \eta_0[p_0 - \mathbf{p}^2/(2M_{nc}) + i\epsilon] - \Sigma_\sigma(p)} \,, \tag{A.1}$$

$$\Sigma_\sigma(p) = -\frac{g_0^2 m_R}{2\pi}\left[i\sqrt{2m_R\left(p_0 - \frac{\mathbf{p}^2}{2M_{nc}}\right)} + \mu\right] \,, \tag{A.2}$$

where PDS is employed as regularization scheme with scale μ [25], [26]. After matching to the effective range expansion, we obtain for the σ propagator

$$D_\sigma(p) = Z_\sigma \frac{1}{p_0 - \frac{\mathbf{p}^2}{2M_{nc}} + B_0} + R_\sigma(p) \,,$$

with

$$Z_\sigma = \frac{2\pi\gamma_0}{m_R^2 g_0^2} \quad \text{(LO)} \,, \quad Z_\sigma = \frac{2\pi}{m_R^2 g_0^2}\gamma_0\left[1 + \gamma_0 r_0\right] \quad \text{(NLO)} \,. \tag{A.3}$$

Here, Z_σ denotes the wave-function renormalization, $B_0 = \gamma_0^2/(2m_R)$ denotes the binding energy and the remainder $R_\sigma(p)$ is regular at the pole.

B. Halo EFT Wave Function

In this Appendix, we present the details of the calculation of the Halo EFT wave functions.

B.1. *P*-Wave Halo EFT Wave Function

In this Section, we derive the calculation of the wave function for a P-wave bound state mentioned in Section 6.3.

For the derivation of the wave function, we use

$$G_{i'i} \sim \frac{|\psi_{i'}\rangle \langle\psi_i|}{E + B_1} \text{ for } E \to -B_1 \,, \tag{B.1}$$

where $G_{i'i}$ is the fully interacting Green's function, B_1 is the binding energy, and $|\psi_i\rangle$ denotes the corresponding P-wave bound state.

Furthermore, we use

$$G_{i'i} = G^0 \delta_{i'i} + G^0 T_{i'i} G^0 \,, \tag{B.2}$$

where G^0 and $T_{i'i}$ are the free Green's function and the P-wave T-matrix, respectively.

Since the free Green's function gives no contribution to the pole, we find from Eq. (B.1) and Eq. (B.2)

$$\lim_{E\to -B_1} \frac{\langle \boldsymbol{k}'|\psi_{i'}\rangle \langle\psi_i|\boldsymbol{k}\rangle}{E + B_1} = \lim_{E\to -B_1} \langle \boldsymbol{k}'| G^0 T_{i'i} G^0 |\boldsymbol{k}\rangle \,. \tag{B.3}$$

We consider

$$\begin{aligned}\lim_{E\to -B_1} \langle \boldsymbol{k}'|\, G^0 T_{i'i} G^0\, |\boldsymbol{k}\rangle &= \lim_{E\to -B_1} \frac{1}{E-\frac{k'^2}{2m_R}+i\epsilon}\, \langle \boldsymbol{k}'|T_{i'i}|\boldsymbol{k}\rangle\, \frac{1}{E-\frac{k^2}{2m_R}+i\epsilon} \\ &= \lim_{E\to -B_1} \frac{1}{-B_1-\frac{k'^2}{2m_R}+i\epsilon}\, \langle \boldsymbol{k}'|T_{i'i}|\boldsymbol{k}\rangle\, \frac{1}{-B_1-\frac{k^2}{2m_R}+i\epsilon} \\ &= \lim_{E\to -B_1} \frac{1}{-B_1-\frac{k'^2}{2m_R}+i\epsilon}\, \left(g_1^2 D_1(-B_1) k_{i'} k_i\right)\, \frac{1}{-B_1-\frac{k^2}{2m_R}+i\epsilon}\,, \end{aligned} \tag{B.4}$$

where we have used

$$\langle \boldsymbol{k}'|T_{i'i}|\boldsymbol{k}\rangle = g_1^2 D_1(-B_1) k_{i'} k_i\,, \tag{B.5}$$

with $D_1(E)$ denoting the full dimer propagator for the P-wave bound state.

We use the expansion of the full dimer propagator around the bound state energy B_1

$$\lim_{E\to -B_1} D_1(E) = \frac{Z_\pi}{E+B_1}\,, \tag{B.6}$$

and obtain

$$\lim_{E\to -B_1} \langle \boldsymbol{k}'|\, G^0 T_{i'i} G^0\, |\boldsymbol{k}\rangle = \lim_{E\to -B_1} \frac{-2m_R g_1\sqrt{Z_\pi} k_i'}{\gamma_1^2+k'^2} \frac{1}{E+B_1} \frac{-2m_R g_1\sqrt{Z_\pi} k_i}{\gamma_1^2+k^2}\,. \tag{B.7}$$

Comparing this result to Eq. (B.2) yields the final result for the wave function in momentum space

$$\langle \boldsymbol{k}|\psi_i\rangle = \frac{-2m_R g_1\sqrt{Z_\pi} k_i}{\gamma_1^2+k^2}\,. \tag{B.8}$$

Finally, coupling the orbital angular momentum with quantum numbers $(1i)$ with the spin of the neutron with quantum numbers $(\frac{1}{2}\alpha)$ gives

$$\langle \boldsymbol{k}|\psi^{\alpha\beta}\rangle = \frac{-2m_R g_1\sqrt{Z_\pi} k_i C^{\frac{3}{2}\beta}_{(1i)(\frac{1}{2}\alpha')}}{\gamma_1^2+k^2}\,. \tag{B.9}$$

B.2. *S*-Wave Halo EFT Wave Function with Coulomb

In this Section, we present the details of the calculation of the 3d wave function mentioned in Section 8.5.

For the calculation of

$$\lim_{E\to -B_0} \frac{\langle \boldsymbol{r}'|\psi\rangle \langle\psi|\boldsymbol{r}\rangle}{E+B_0} = \lim_{E\to -B_0} \langle \boldsymbol{r}'| G^0 T^{SC} G^0 |\boldsymbol{r}\rangle \ , \tag{B.10}$$

we consider

$$\begin{aligned}
\langle \boldsymbol{r}'| G^0 T^{SC} G^0 |\boldsymbol{r}\rangle &= \int \frac{\mathrm{d}^3 p}{(2\pi)^3} \int \frac{\mathrm{d}^3 p'}{(2\pi)^3} \langle \boldsymbol{r}'|\boldsymbol{p}'\rangle \langle \boldsymbol{p}'|G^0 T^{SC} G^0|\boldsymbol{p}\rangle \langle \boldsymbol{p}|\boldsymbol{r}\rangle \\
&= \int \frac{\mathrm{d}^3 p}{(2\pi)^3} \int \frac{\mathrm{d}^3 p'}{(2\pi)^3} e^{i\boldsymbol{p}'\boldsymbol{r}'} e^{-i\boldsymbol{p}\boldsymbol{r}} \langle \boldsymbol{p}'|G^0 T^{SC} G^0|\boldsymbol{p}\rangle \\
&= \int \frac{\mathrm{d}^3 p}{(2\pi)^3} \int \frac{\mathrm{d}^3 p'}{(2\pi)^3} e^{i\boldsymbol{p}'\boldsymbol{r}'} e^{-i\boldsymbol{p}\boldsymbol{r}} \frac{1}{E-\frac{p'^2}{2m_R}+i\epsilon} \langle \boldsymbol{p}'|T^{SC}|\boldsymbol{p}\rangle \frac{1}{E-\frac{p^2}{2m_R}+i\epsilon} \\
&= \int \frac{\mathrm{d}^3 p}{(2\pi)^3} \int \frac{\mathrm{d}^3 p'}{(2\pi)^3} e^{i\boldsymbol{p}'\boldsymbol{r}'} e^{-i\boldsymbol{p}\boldsymbol{r}} \frac{1}{E-\frac{p'^2}{2m_R}+i\epsilon} \\
&\quad \times \left(\int \frac{\mathrm{d}^3 k}{(2\pi)^3} \frac{t_C(E;\boldsymbol{k},\boldsymbol{p})}{E-\frac{k^2}{2m_R}+i\epsilon} g_0^2 D_0(E) \int \frac{\mathrm{d}^3 l}{(2\pi)^3} \frac{t_C(E;\boldsymbol{p}',\boldsymbol{l})}{E-\frac{l^2}{2m_R}+i\epsilon} \right) \\
&\quad \times \frac{1}{E-\frac{p^2}{2m_R}+i\epsilon} \, ,
\end{aligned} \tag{B.11}$$

where we have used

$$\langle \boldsymbol{p}'|T^{SC}|\boldsymbol{p}\rangle = \int \frac{\mathrm{d}^3 k}{(2\pi)^3} \frac{t_C(E;\boldsymbol{k},\boldsymbol{p})}{E-\frac{k^2}{2m_R}+i\epsilon} g_0^2 D_0(E) \int \frac{\mathrm{d}^3 l}{(2\pi)^3} \frac{t_C(E;\boldsymbol{p}',\boldsymbol{l})}{E-\frac{l^2}{2m_R}+i\epsilon} \, , \tag{B.12}$$

with $D_0(E)$ denoting the full dimer propagator illustrated in Fig. 8.2.

We rearrange the last line of Eq. (B.11) to get

$$\begin{aligned}\langle \boldsymbol{r}' |\, G^0 T^{SC} G^0 \,| \boldsymbol{r} \rangle =& g_0^2 D_0(E) \int \frac{\mathrm{d}^3 p}{(2\pi)^3} \int \frac{\mathrm{d}^3 p'}{(2\pi)^3} \int \frac{\mathrm{d}^3 k}{(2\pi)^3} \int \frac{\mathrm{d}^3 l}{(2\pi)^3} e^{i\boldsymbol{p}'\boldsymbol{r}'} e^{-i\boldsymbol{p}\boldsymbol{r}} \\ & \times \frac{t_C(E;\boldsymbol{k},\boldsymbol{p})}{\left(E - \frac{k^2}{2m_R} + i\epsilon\right)\left(E - \frac{p^2}{2m_R} + i\epsilon\right)} \\ & \times \frac{t_C(E;\boldsymbol{p}',\boldsymbol{l})}{\left(E - \frac{p'^2}{2m_R} + i\epsilon\right)\left(E - \frac{l^2}{2m_R} + i\epsilon\right)} \,. \end{aligned} \tag{B.13}$$

Now we use the relation

$$G^{C+}(E;\boldsymbol{k},\boldsymbol{p}) = \frac{t_C(E;\boldsymbol{k},\boldsymbol{p})}{\left(E - \frac{k^2}{2m_R} + i\epsilon\right)\left(E - \frac{p^2}{2m_R} + i\epsilon\right)} \,, \tag{B.14}$$

and obtain

$$\begin{aligned}\langle \boldsymbol{r}' |\, G^0 T^{SC} G^0 \,| \boldsymbol{r} \rangle =& g_0^2 D_0(E) \int \frac{\mathrm{d}^3 p}{(2\pi)^3} \int \frac{\mathrm{d}^3 p'}{(2\pi)^3} \int \frac{\mathrm{d}^3 k}{(2\pi)^3} \int \frac{\mathrm{d}^3 l}{(2\pi)^3} \\ & \times e^{-i\boldsymbol{p}\boldsymbol{r}} G^{C+}(E;\boldsymbol{k},\boldsymbol{p}) e^{i\boldsymbol{p}'\boldsymbol{r}'} G^{C+}(E;\boldsymbol{p}',\boldsymbol{l}) \\ =& g_0^2 D_0(E) G^{C+}(E;\boldsymbol{r}'=\boldsymbol{0},\boldsymbol{r}) G^{C+}(E;\boldsymbol{r}',\boldsymbol{r}=\boldsymbol{0}) \\ =& g_0^2 D_0(E) \,\langle \boldsymbol{0}|G^{C+}(E)|\boldsymbol{r}\rangle \,\langle \boldsymbol{r}'|G^{C+}(E)|\boldsymbol{0}\rangle \,. \end{aligned} \tag{B.15}$$

Finally, we use the expansion of the full dimer propagator around the bound state pole energy B_0

$$\lim_{E\to -B_0} D_0(E) = \frac{Z_\sigma}{E + B_0} \,, \tag{B.16}$$

and obtain

$$\begin{aligned}\lim_{E\to -B_0} \frac{\langle \boldsymbol{r}'|\psi\rangle \,\langle \psi|\boldsymbol{r}\rangle}{E + B_0} =& \lim_{E\to -B_0} \\ & \times \left(g\sqrt{Z_\sigma}\,\langle \boldsymbol{r}'|G^{C+}(-B_0)|\boldsymbol{0}\rangle\right) \frac{1}{E+B_0} \left(g\sqrt{Z_\sigma}\,\langle \boldsymbol{0}|G^{C+}(-B_0)|\boldsymbol{r}\rangle\right) \,. \end{aligned} \tag{B.17}$$

This yields

$$\psi(\boldsymbol{r}) = g_0\sqrt{Z_\sigma}\,\langle \boldsymbol{r}|G^{C+}(-B_0)|\boldsymbol{0}\rangle \,. \tag{B.18}$$

C. 1d Scattering

In this Appendix, we briefly demonstrate the derivation of the 1d dimer self-energy including Coulomb interactions.

C.1. 1d Coulomb Wave Function

Firstly, we consider the Coulomb wave function in 3d [93]

$$\left(\chi_{\boldsymbol{p}}(\boldsymbol{r})^{+}\right)^{\mathrm{3d}} = \sum_{l=0}^{\infty}(2l+1)i^{l}e^{i\sigma_l}P_l(\hat{p}\hat{r})\frac{F_l(\eta_p,pr)}{pr} \tag{C.1}$$

where $\hat{p}$ and $\hat{r}$ are the unit vectors of $\boldsymbol{p}$ and $\boldsymbol{r}$, respectively. Moreover, P_l is the l-th Legendre polynomial and the function F_l is given by

$$F_l(\eta_p,pr) = C_l(\eta_p)2^{-l-1}(-i)^{l+1}M_{i\eta_p,l+1/2}(2ipr)\,, \tag{C.2}$$

while $M_{k,\mu}(z)$ is a conventionally defined Whittaker function and $C_l(\eta_p)$ reads

$$C_l(\eta_p) = \frac{2^l e^{-\pi\eta_p/2}\left|\Gamma(l+1+i\eta_p)\right|}{\Gamma(2l+2)}\,. \tag{C.3}$$

In analogy to the transition from 3d to 1d of a plane wave, we set $P_l(\hat{p}\hat{r}) = 1$. This yields the 1d Coulomb wave function

$$\left(\chi_p(x)^{+}\right)^{\mathrm{1d}} = \sum_{l=0}^{\infty}(2l+1)i^{l}e^{i\sigma_l}\frac{F_l(\eta_p,px)}{px}\,. \tag{C.4}$$

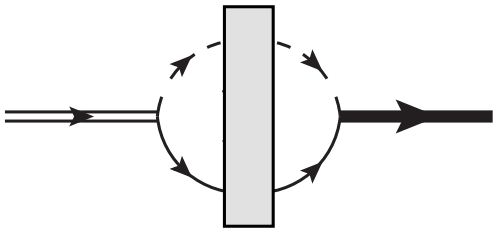

Figure C.1.: 1d self-energy with Coulomb interactions. We use the same notation as in Fig. 8.1.

C.2. 1d Self-Energy with Coulomb Interactions

In arbitrary dimension d, the dimer self-energy depicted in Fig. C.1 reads

$$-i\Sigma(E) = -ig_0^2 \int \frac{\mathrm{d}^\mathrm{d} q}{(2\pi)^d} \int \frac{\mathrm{d}^\mathrm{d} k}{(2\pi)^d} \frac{t^C(E;\boldsymbol{k},\boldsymbol{q})}{\left(E - \frac{q^2}{2m_R} + i\epsilon\right)\left(E - \frac{k^2}{2m_R} + i\epsilon\right)} \tag{C.5}$$

$$= -ig_0^2 \int \frac{\mathrm{d}^\mathrm{d} q}{(2\pi)^d} \int \frac{\mathrm{d}^\mathrm{d} k}{(2\pi)^d} G^{C+}(E;\boldsymbol{k},\boldsymbol{q}) \tag{C.6}$$

$$= -ig_0^2 G^{C+}(E;\boldsymbol{r}'=\boldsymbol{0},\boldsymbol{r}=\boldsymbol{0}) \tag{C.7}$$

$$= -ig_0^2 \left\langle \boldsymbol{r}'=\boldsymbol{0}|G^{C+}(E)|\boldsymbol{r}=\boldsymbol{0})\right\rangle \,, \tag{C.8}$$

where $E = p^2/(2m_R)$ is the center-of-mass energy.

We insert a complete set of Coulomb wave functions to find

$$-i\Sigma(E) = -ig_0^2 \left\langle \boldsymbol{r}'=\boldsymbol{0}\right| G^{C+}(E) \int \frac{\mathrm{d}^\mathrm{d} q}{(2\pi)^d} \left|\chi_{\boldsymbol{q}}^+\right\rangle \left\langle \chi_{\boldsymbol{q}}^+ | \boldsymbol{r}=\boldsymbol{0}\right\rangle \tag{C.9}$$

$$= -ig_0^2 \int \frac{\mathrm{d}^\mathrm{d} q}{(2\pi)^d} \frac{\chi_q^+(\boldsymbol{r}'=\boldsymbol{0})\chi_q^{+*}(\boldsymbol{r}=\boldsymbol{0})}{E - \frac{q^2}{2m_R} + i\epsilon} \tag{C.10}$$

$$= i2m_R g_0^2 \int \frac{\mathrm{d}^\mathrm{d} q}{(2\pi)^d} \frac{\chi_q^+(\boldsymbol{r}'=\boldsymbol{0})\chi_q^{+*}(\boldsymbol{r}=\boldsymbol{0})}{q^2 - 2m_R E - i\epsilon} \,. \tag{C.11}$$

In the limit $r \to 0$, only $l = 0$ contributes to the Coulomb wave function and we obtain

$$\chi_q^{+*}(\boldsymbol{r} = \boldsymbol{0})\chi_q^{+*}(\boldsymbol{r} = \boldsymbol{0}) = C_0^2(\eta_q) \tag{C.12}$$

$$= \frac{2\pi\eta_q}{e^{2\pi\eta_q} - 1}\,. \tag{C.13}$$

Inserting this result in Eq. (C.11) yields

$$-i\Sigma(E) = i2m_R g_0^2 \int \frac{\mathrm{d}^\mathrm{d} q}{(2\pi)^d} \frac{1}{q^2 - 2m_R E - i\epsilon} \frac{2\pi\eta_q}{e^{2\pi\eta_q} - 1}\,. \tag{C.14}$$

We use [105]

$$\int \frac{\mathrm{d}^\mathrm{d} q}{(2\pi)^d} f(|\boldsymbol{q}|) = \int \mathrm{d}\Omega_\mathrm{d} \int \frac{\mathrm{d}q}{(2\pi)^\mathrm{d}} q^{\mathrm{d}-1} f(|\boldsymbol{q}|) \tag{C.15}$$

$$= \frac{1}{2^{\mathrm{d}-1}\Gamma(\mathrm{d}/2)\pi^{\frac{\mathrm{d}}{2}}} \int \mathrm{d}q q^{\mathrm{d}-1} f(|\boldsymbol{q}|)\,, \tag{C.16}$$

and introduce a new integration variable $x = 2\pi\eta_q = 2\pi k_C/q$ to find

$$-i\Sigma(E) = -i2m_R g_0^2 \frac{(2\pi k_C)^\mathrm{d}}{p^2 2^{\mathrm{d}-1}\Gamma(\mathrm{d}/2)\pi^{\frac{\mathrm{d}}{2}}} \int \mathrm{d}x \frac{x^{2-\mathrm{d}}}{x^2 - (2\pi\eta_p)^2 + i\epsilon} \frac{1}{e^x - 1}\,. \tag{C.17}$$

The result for d$= 1$ is finite and we obtain [106]

$$-i\Sigma(E) = -i2m_R g_0^2 \frac{2\pi k_C}{p^2\sqrt{\pi}\sqrt{\pi}} \left(-\frac{1}{2} H(\eta_p)\right) \tag{C.18}$$

$$= i\frac{2m_R g_0^2}{k_C} \eta_p^2 H(\eta_p)\,, \tag{C.19}$$

with

$$H(\eta_p) = \Psi(i\eta_p) + \frac{1}{2i\eta_p} - \ln(i\eta_p)\,, \tag{C.20}$$

where $\Psi(x)$ is the digamma function.

Finally, the 1d self-energy with Coulomb interactions reads

$$\Sigma(E) = -\frac{2m_R g_0^2}{k_C} \eta_p^2 H(\eta_p)\,. \tag{C.21}$$

Bibliography

[1] K. G. Wilson, "Confinement of Quarks", J. C. Taylor, Ed., pp. 45–59, Feb. 1974.

[2] S. Durr *et al.*, "Ab-Initio Determination of Light Hadron Masses", *Science*, vol. 322, pp. 1224–1227, 2008.

[3] G. Bertsch, D. Dean, and W. Nazarewicz, "Computing atomic nuclei: The universal nuclear energy density functional", *SciDAC Review*, vol. 6, Jan. 2007.

[4] E. Epelbaum, H.-W. Hammer, and U.-G. Meißner, "Modern theory of nuclear forces", *Rev. Mod. Phys.*, vol. 81, pp. 1773–1825, 2009.

[5] R. Machleidt and D. R. Entem, "Chiral effective field theory and nuclear forces", *Phys. Rept.*, vol. 503, pp. 1–75, 2011.

[6] P. Navratil, S. Quaglioni, I. Stetcu, and B. R. Barrett, "Recent developments in no-core shell-model calculations", *J. Phys. G*, vol. 36, p. 083 101, 2009.

[7] G. Hagen, D. J. Dean, M. Hjorth-Jensen, T. Papenbrock, and A. Schwenk, "Benchmark calculations for ^{3}H, ^{4}He, ^{16}O and ^{40}Ca with *ab initio* coupled-cluster theory", *Phys. Rev. C*, vol. 76, p. 044 305, 2007.

[8] K. Tsukiyama, S. K. Bogner, and A. Schwenk, "In-Medium Similarity Renormalization Group For Nuclei", *Phys. Rev. Lett.*, vol. 106, p. 222 502, 2011.

[9] H. Hergert, "A Guided Tour of *ab initio* Nuclear Many-Body Theory", *Front. in Phys.*, vol. 8, p. 379, 2020.

[10] F. Hoyle, "On Nuclear Reactions Occuring in Very Hot STARS.I. the Synthesis of Elements from Carbon to Nickel.", vol. 1, p. 121, Sep. 1954.

[11] I. Tanihata, H. Hamagaki, O. Hashimoto, Y. Shida, N. Yoshikawa, K. Sugimoto, O. Yamakawa, T. Kobayashi, and N. Takahashi, "Measurements of Interaction Cross Sections and Nuclear Radii in the Light p-Shell Region", *Phys. Rev. Lett.*, vol. 55, pp. 2676–2679, 1985.

[12] I. Tanihata *et al.*, “Measurements of Interaction Cross Sections and Radii of He Isotopes”, *Phys. Lett. B*, vol. 160, pp. 380–384, 1985.

[13] C. A. Bertulani, H.-W. Hammer, and U. Van Kolck, “Effective field theory for halo nuclei”, *Nucl. Phys. A*, vol. 712, pp. 37–58, 2002.

[14] P. F. Bedaque, H.-W. Hammer, and U. van Kolck, “Narrow resonances in effective field theory”, *Phys. Lett. B*, vol. 569, pp. 159–167, 2003.

[15] H.-W. Hammer, C. Ji, and D. R. Phillips, “Effective field theory description of halo nuclei”, *J. Phys. G*, vol. 44, no. 10, p. 103 002, 2017.

[16] D. R. Tilley, J. H. Kelley, J. L. Godwin, D. J. Millener, J. E. Purcell, C. G. Sheu, and H. R. Weller, “Energy levels of light nuclei A=8,9,10”, *Nucl. Phys. A*, vol. 745, pp. 155–362, 2004.

[17] J. H. Kelley, E. Kwan, J. E. Purcell, C. G. Sheu, and H. R. Weller, “Energy levels of light nuclei”, *Nucl. Phys. A*, vol. 880, pp. 88–195, 2012.

[18] *National nuclear data center, information extracted from the nudat 2 database*. [Online]. Available: `https://www.nndc.bnl.gov/nudat2/`.

[19] I. Tanihata, “Nuclear Physics with RIB’s: How it all started”, *Eur. Phys. J. Plus*, vol. 131, no. 4, p. 90, 2016.

[20] T. Nakamura, “Neutron Halo - Recent Experimental Progress at RIBF”, *AAPPS Bull.*, vol. 29, no. 5, 2019.

[21] J. J. Sakurai and J. Napolitano, *Modern Quantum Mechanics*, 2nd ed. Cambridge University Press, 2017.

[22] J. R. Taylor, *Scattering theory: the quantum theory of nonrelativistic collisions*. Dover, 2006.

[23] S. Weinberg, “Phenomenological Lagrangians”, *Physica A*, vol. 96, no. 1-2, S. Deser, Ed., pp. 327–340, 1979.

[24] J. Braun, W. Elkamhawy, R. Roth, and H.-W. Hammer, “Electric structure of shallow *D*-wave states in Halo EFT”, *J. Phys. G*, vol. 46, no. 11, p. 115 101, 2019.

[25] D. B. Kaplan, M. J. Savage, and M. B. Wise, “A New expansion for nucleon-nucleon interactions”, *Phys. Lett. B*, vol. 424, pp. 390–396, 1998.

[26] D. B. Kaplan, M. J. Savage, and M. B. Wise, “Two nucleon systems from effective field theory”, *Nucl. Phys. B*, vol. 534, pp. 329–355, 1998.

[27] J. Braun, H.-W. Hammer, and L. Platter, “Halo structure of ^{17}C”, *Eur. Phys. J. A*, vol. 54, no. 11, p. 196, 2018.

[28] F. Ajzenberg-Selove, “Energy levels of light nuclei A = 13−15”, *Nucl. Phys. A*, vol. 449, pp. 1–155, 1986.

[29] R. Roth, “Importance Truncation for Large-Scale Configuration Interaction Approaches”, *Phys. Rev. C*, vol. 79, p. 064 324, 2009.

[30] A. Calci and R. Roth, “Sensitivities and correlations of nuclear structure observables emerging from chiral interactions”, *Phys. Rev. C*, vol. 94, no. 1, p. 014 322, 2016.

[31] A. Bohr and B. R. Mottelson, *Nuclear structure, vol. II*. Benjamin, New York, 1975.

[32] A. S. Jensen, K. Riisager, D. V. Fedorov, and E. Garrido, “Structure and reactions of quantum halos”, *Rev. Mod. Phys.*, vol. 76, pp. 215–261, 2004.

[33] K. Riisager, “Halos and related structures”, *Phys. Scripta T*, vol. 152, p. 014 001, 2013.

[34] S.-I. Ando, “Hypernuclei in Halo/Cluster Effective Field Theory”, *Int. J. Mod. Phys. E*, vol. 25, no. 05, p. 1 641 005, 2016.

[35] G. Rupak, “Radiative reactions in halo effective field theory”, *Int. J. Mod. Phys. E*, vol. 25, no. 05, p. 1 641 004, 2016.

[36] R. Higa, H.-W. Hammer, and U. van Kolck, “alpha alpha Scattering in Halo Effective Field Theory”, *Nucl. Phys. A*, vol. 809, pp. 171–188, 2008.

[37] D. L. Canham and H.-W. Hammer, “Universal properties and structure of halo nuclei”, *Eur. Phys. J. A*, vol. 37, pp. 367–380, 2008.

[38] D. L. Canham and H.-W. Hammer, “Range corrections for two-neutron halo nuclei in effective theory”, *Nucl. Phys. A*, vol. 836, pp. 275–292, 2010.

[39] J. Rotureau and U. van Kolck, “Effective Field Theory and the Gamow Shell Model: The ^6He Halo Nucleus”, *Few Body Syst.*, vol. 54, pp. 725–735, 2013.

[40] C. Ji, C. Elster, and D. R. Phillips, “^{6}He nucleus in halo effective field theory”, *Phys. Rev. C*, vol. 90, no. 4, p. 044 004, 2014.

[41] H.-W. Hammer and D. R. Phillips, “Electric properties of the Beryllium-11 system in Halo EFT”, *Nucl. Phys. A*, vol. 865, pp. 17–42, 2011.

[42] L. Fernando, A. Vaghani, and G. Rupak, “Electromagnetic form factors of one neutron halos with spin 1/2+ ground state”, Nov. 2015.

[43] G. Rupak and R. Higa, “Model-Independent Calculation of Radiative Neutron Capture on Lithium-7”, *Phys. Rev. Lett.*, vol. 106, p. 222 501, 2011.

[44] X. Zhang, K. M. Nollett, and D. R. Phillips, "Combining *ab initio* calculations and low-energy effective field theory for halo nuclear systems: The case of $^7\mathrm{Li} + n \to {}^8\mathrm{Li} + \gamma$", *Phys. Rev. C*, vol. 89, no. 2, p. 024 613, 2014.

[45] G. Rupak, L. Fernando, and A. Vaghani, "Radiative Neutron Capture on Carbon-14 in Effective Field Theory", *Phys. Rev. C*, vol. 86, p. 044 608, 2012.

[46] B. Acharya and D. R. Phillips, "^{19}C in halo EFT: Effective-range parameters from Coulomb dissociation experiments", *Nucl. Phys. A*, vol. 913, pp. 103–115, 2013.

[47] P. Hagen, H.-W. Hammer, and L. Platter, "Charge form factors of two-neutron halo nuclei in halo EFT", *Eur. Phys. J. A*, vol. 49, p. 118, 2013.

[48] X. Zhang, K. M. Nollett, and D. R. Phillips, "Combining *ab initio* calculations and low-energy effective field theory for halo nuclear systems: The case of $^7\mathrm{Be}+p \to {}^8\mathrm{B}+\gamma$", *Phys. Rev. C*, vol. 89, no. 5, p. 051 602, 2014.

[49] L. S. Brown and G. M. Hale, "Field Theory of the $d + t \to n + \alpha$ Reaction Dominated by a $^5\mathrm{He}^*$ Unstable Particle", *Phys. Rev. C*, vol. 89, no. 1, p. 014 622, 2014.

[50] H. W. Griesshammer, "Improved convergence in the three-nucleon system at very low energies", *Nucl. Phys. A*, vol. 744, pp. 192–226, 2004.

[51] M. Tanabashi *et al.*, "Review of Particle Physics", *Phys. Rev. D*, vol. 98, no. 3, p. 030 001, 2018.

[52] S. R. Beane and M. J. Savage, "Rearranging pionless effective field theory", *Nucl. Phys. A*, vol. 694, pp. 511–524, 2001.

[53] U. van Kolck, "Nucleon-nucleon interaction and isospin violation", *Lect. Notes Phys.*, vol. 513, A. Bernstein, D. Drechsel, and T. Walcher, Eds., p. 62, 1998.

[54] U. van Kolck, "Effective field theory of short range forces", *Nucl. Phys. A*, vol. 645, pp. 273–302, 1999.

[55] A. Buckingham, "Molecular quadrupole moments", *Quarterly Reviews, Chemical Society*, vol. 13, no. 3, pp. 183–214, 1959.

[56] R. A. Briceno, Z. Davoudi, and T. C. Luu, "Two-Nucleon Systems in a Finite Volume: (I) Quantization Conditions", *Phys. Rev. D*, vol. 88, no. 3, p. 034 502, 2013.

[57] W. Greiner, D. A. Bromley, and J. Maruhn, *Nuclear Models*. Springer Berlin Heidelberg, 1996.

[58] S. Typel and G. Baur, "Electromagnetic strength of neutron and proton single-particle halo nuclei", *Nucl. Phys. A*, vol. 759, pp. 247–308, 2005.

[59] I. Angeli and K. P. Marinova, "Table of experimental nuclear ground state charge radii: An update", *Atom. Data Nucl. Data Tabl.*, vol. 99, no. 1, pp. 69–95, 2013.

[60] R. J. Furnstahl, N. Klco, D. R. Phillips, and S. Wesolowski, "Quantifying truncation errors in effective field theory", *Phys. Rev. C*, vol. 92, no. 2, p. 024 005, 2015.

[61] S. Wesolowski, N. Klco, R. J. Furnstahl, D. R. Phillips, and A. Thapaliya, "Bayesian parameter estimation for effective field theories", *J. Phys. G*, vol. 43, no. 7, p. 074 001, 2016.

[62] H. W. Griesshammer, J. A. McGovern, and D. R. Phillips, "Nucleon polarisabilities at and beyond hysical Pion Masses", *Eur. Phys. J. A*, vol. 52, no. 5, p. 139, 2016.

[63] T. Nakamura *et al.*, "Neutron capture cross section of ^{14}C of astrophysical interest studied by Coulomb breakup of ^{15}C", *Phys. Rev. C*, vol. 79, p. 035 805, 2009.

[64] D. R. Entem and R. Machleidt, "Accurate charge dependent nucleon nucleon potential at fourth order of chiral perturbation theory", *Phys. Rev. C*, vol. 68, p. 041 001, 2003.

[65] P. Navratil, "Local three-nucleon interaction from chiral effective field theory", *Few Body Syst.*, vol. 41, pp. 117–140, 2007.

[66] E. Epelbaum, W. Glöckle, and U.-G. Meißner, "Improving the convergence of the chiral expansion for nuclear forces. 1. Peripheral phases", *Eur. Phys. J. A*, vol. 19, pp. 125–137, 2004.

[67] K. Hebeler and R. J. Furnstahl, "Neutron matter based on consistently evolved chiral three-nucleon interactions", *Phys. Rev. C*, vol. 87, no. 3, p. 031 302, 2013.

[68] I. Tews, T. Krüger, K. Hebeler, and A. Schwenk, "Neutron Matter at Next-to-Next-to-Next-to-Leading Order in Chiral Effective Field Theory", *Phys. Rev. Lett.*, vol. 110, no. 3, p. 032 504, 2013.

[69] T. Krüger, I. Tews, K. Hebeler, and A. Schwenk, "Neutron matter from chiral effective field theory interactions", *Phys. Rev. C*, vol. 88, p. 025 802, 2013.

[70] S. Weinberg, "Effective chiral Lagrangians for nucleon - pion interactions and nuclear forces", *Nucl. Phys. B*, vol. 363, pp. 3–18, 1991.

[71] A. Nogga, S. K. Bogner, and A. Schwenk, "Low-momentum interaction in few-nucleon systems", *Phys. Rev. C*, vol. 70, p. 061 002, 2004.

[72] E. Braaten and H.-W. Hammer, "Universality in few-body systems with large scattering length", *Phys. Rept.*, vol. 428, pp. 259–390, 2006.

[73] T. Nakamura *et al.*, "Deformation-Driven ρ-Wave Halos at the Drip Line: Ne^{31}", *Phys. Rev. Lett.*, vol. 112, no. 14, p. 142 501, 2014.

[74] M. Shamsuzzoha Basunia, "Nuclear Data Sheets for A = 30", *Nucl. Data Sheets*, vol. 111, pp. 2331–2424, 2010.

[75] V. Zelevinsky and A. Volya, "Nuclear deformation", in *Physics of Atomic Nuclei*. John Wiley & Sons, Ltd, 2017, ch. 12, pp. 223–250.

[76] W. Greiner and J. A. Maruhn, *Nuclear Models*. Springer, 1996.

[77] W. Elkamhawy, Z. Yang, H.-W. Hammer, and L. Platter, "β-delayed proton emission from ^{11}Be in effective field theory", Sep. 2019.

[78] M. J. G. Borge, L. M. Fraile, H. O. U. Fynbo, B. Jonson, O. S. Kirsebom, T. Nilsson, G. Nyman, G. Possnert, K. Riisager, and O. Tengblad, "Rare βp decays in light nuclei", *J. Phys. G*, vol. 40, p. 035 109, 2013.

[79] K. Riisager and IS541 collaboration, "Beta decay to continuum states: the case of ^{11}Be", *EPJ Web of Conferences*, vol. 66, p. 02 090, 2014. [Online]. Available: https://doi.org/10.1051/epjconf/20146602090.

[80] K. Riisager *et al.*, "^{11}Be(βp), a quasi-free neutron decay?", *Phys. Lett. B*, vol. 732, pp. 305–308, 2014.

[81] D. Baye and E. M. Tursunov, "Beta delayed emission of a proton by a one-neutron halo nucleus", *Phys. Lett. B*, vol. 696, pp. 464–467, 2011.

[82] M. Pfützner and K. Riisager, "Examining the possibility to observe neutron dark decay in nuclei", *Phys. Rev. C*, vol. 97, no. 4, p. 042 501, 2018.

[83] B. Fornal and B. Grinstein, "Dark Matter Interpretation of the Neutron Decay Anomaly", *Phys. Rev. Lett.*, vol. 120, no. 19, p. 191 801, 2018, [Erratum: Phys.Rev.Lett. 124, 219901 (2020)].

[84] Y. Ayyad *et al.*, "Direct observation of proton emission in 11Be", *Phys. Rev. Lett.*, vol. 123, no. 8, p. 082 501, 2019, [Erratum: Phys.Rev.Lett. 124, 129902 (2020)].

[85] H. O. U. Fynbo, Z. Janas, C. Mazzocchi, M. Pfützner, J. Refsgaard, K. Riisager, and N. Sokołowska, "Comment on "Direct Observation of Proton Emission in ^{11}Be"", Dec. 2019.

[86] K. Riisager *et al.*, "Search for beta-delayed proton emission from ^{11}Be", *Eur. Phys. J. A*, vol. 56, no. 3, p. 100, 2020.

[87] J. Refsgaard, J. Büscher, A. Arokiaraj, H. O. U. Fynbo, R. Raabe, and K. Riisager, "Clarification of large-strength transitions in the β decay of ^{11}Be", *Phys. Rev. C*, vol. 99, no. 4, p. 044 316, 2019.

[88] X. Kong and F. Ravndal, "Proton proton fusion in leading order of effective field theory", *Nucl. Phys. A*, vol. 656, pp. 421–429, 1999.

[89] J. C. Hardy and I. S. Towner, "Superallowed $0^+ \to 0^+$ nuclear β decays: A critical survey with tests of the conserved vector current hypothesis and the standard model", *Phys. Rev. C*, vol. 71, p. 055 501, 2005.

[90] E. Ryberg, C. Forssén, H.-W. Hammer, and L. Platter, "Effective field theory for proton halo nuclei", *Phys. Rev. C*, vol. 89, no. 1, p. 014 325, 2014.

[91] J. Okołowicz, M. Płoszajczak, and W. Nazarewicz, "Convenient Location of a Near-Threshold Proton-Emitting Resonance in ^{11}B", *Phys. Rev. Lett.*, vol. 124, no. 4, p. 042 502, 2020.

[92] M. Schmidt, L. Platter, and H.-W. Hammer, "Neutron transfer reactions in halo effective field theory", *Phys. Rev. C*, vol. 99, no. 5, p. 054 611, 2019.

[93] R. Higa, G. Rupak, and A. Vaghani, "Radiative^{3}He(α, γ)^{7}Be reaction in halo effective field theory", *Eur. Phys. J. A*, vol. 54, no. 5, p. 89, 2018.

[94] J. H. Eberly, "Quantum scattering theory in one dimension", *American Journal of Physics*, vol. 33, no. 10, pp. 771–773, 1965.

[95] H.-W. Hammer and D. Lee, "Causality and the effective range expansion", *Annals Phys.*, vol. 325, pp. 2212–2233, 2010.

[96] S. König, "Effective quantum theories with short- and long-range forces", PhD thesis, Rheinische Friedrich-Wilhelms-Universität Bonn, 2013.

[97] A. G. Volosniev, Private Communication, 2020.

[98] D. R. Phillips and T. D. Cohen, "How short is too short? Constraining contact interactions in nucleon-nucleon scattering", *Phys. Lett. B*, vol. 390, pp. 7–12, 1997.

[99] E. P. Wigner, "Lower Limit for the Energy Derivative of the Scattering Phase Shift", *Phys. Rev.*, vol. 98, pp. 145–147, 1955.

[100] C. H. Schmickler, H.-W. Hammer, and A. G. Volosniev, "Universal physics of bound states of a few charged particles", *Phys. Lett. B*, vol. 798, p. 135 016, 2019.

[101] B. K. Luna and T. Papenbrock, "Low-energy bound states, resonances, and scattering of light ions", *Phys. Rev. C*, vol. 100, no. 5, p. 054 307, 2019.

[102] E. Ryberg, C. Forssén, H.-W. Hammer, and L. Platter, "Range corrections in Proton Halo Nuclei", *Annals Phys.*, vol. 367, pp. 13–32, 2016.

[103] R. Morlock, R. Kunz, A. Mayer, M. Jaeger, A. Müller, J. W. Hammer, P. Mohr, H. Oberhummer, G. Staudt, and V. Kolle, "Halo Properties of the First $1/2^+$ State in ^{17}F from the ^{16}O$(p,\gamma)^{17}$F Reaction", *Phys. Rev. Lett.*, vol. 79, pp. 3837–3840, 1997.

[104] I. Tanihata, H. Savajols, and R. Kanungo, "Recent experimental progress in nuclear halo structure studies", *Prog. Part. Nucl. Phys.*, vol. 68, pp. 215–313, 2013.

[105] M. E. Peskin and D. V. Schroeder, *An Introduction to quantum field theory*. Reading, USA: Addison-Wesley, 1995.

[106] I. S. Gradshteyn and I. M. Ryzhik, *Table of integrals, series, and products*. Elsevier/Academic Press, Amsterdam, 2007.